Supplementary Materials for

Self-assembly of nanocrystals into strongly electronically coupled all-inorganic supercrystals

Igor Coropceanu *et al*.

Corresponding author: Dmitri V. Talapin, dvtalapin@uchicago.edu

Science **375**, 1422 (2022)
DOI: 10.1126/science.abm6753

The PDF file includes:

Materials and Methods
Supplementary Text
Figs. S1 to S39
References

1. Materials and Methods

1.1. Synthetic Methods

Chemicals. Potassium sulfide (95% anhydrous), alladium(II) acetylacetonate, (99%), Nickel(II) acetylacetonate, (anhydrous, min. 95%), and Tri-n-octylphosphine (97%) were purchased from Strem Chemicals.

Gold(III) chloride trihydrate (≥99.9% trace metals basis), Borane tert-butylamine complex (powder, 97%), Oleylamine (70%, tech.), Cadmium oxide (99.99% Cd), Lead(II) Oxide (99.999%), Oleic acid (90%), 1,2,3,4-Tetrahydronaphthalene (ReagentPlus, 99%), hexamethyldisilathiane (synthesis grade), selenium (99.99% pellets), tellurium (99.999%), Arsenic powder (≥99.997% trace metals basis), 1-octadecene (90%), Oleic acid (90%), 1-Dodecanethiol (≥98%), Hydrazine (anhydrous, 98%), N-Methylformamide (99%), Hexane (99%), and Toluene (99.8%) were purchased from Millipore Sigma.

N-Methylformamide (99%), Sulfur (99.999%), Arsenic(III) sulfide (Powder, 99.99%), Copper(I) sulfide, (99.5%), Tin powder, (325 mesh, 99.8%, metals basis) and Indium(III) selenide (99.99% metals basis) were obtained from Alfa Aesar.

Arsenic(V) sulfide was purchased from Santa Cruz Biotechnology.

Tetradecylphosphonic acid was purchased from PCI.

N-methylformamide was purified by standard vacuum distillation techniques and stored in a nitrogen glovebox with molecular sieves. All other chemicals were used without purification.

Nanocrystal Synthesis. All nanocrystals were synthesized according to previously reported methods with details provided in the supplementary information.

Au: Au nanocrystals were synthesized by previously reported methods (*49*, *50*).

Pd: Pd nanoparticles were prepared via decomposition of a Pd-TOP complex in the presence of oleic acid (*51*).

Ni: Ni nanoparticles were prepared by decomposition of nickel acetylacetonate in a mixture of tri-n-octylphosphine and oleylamine according to ref (*52*).

CdSe: Phosphonate capped wurtzite (*53*) and carboxylate capped zincblende CdSe (*54*) particles were prepared by literature methods.

PbS: PbS nanocrystals were synthesized according to previously reported methods (*55*).

PbSe: PbSe nanocrystals were synthesized according to a previously detailed method (*56*).

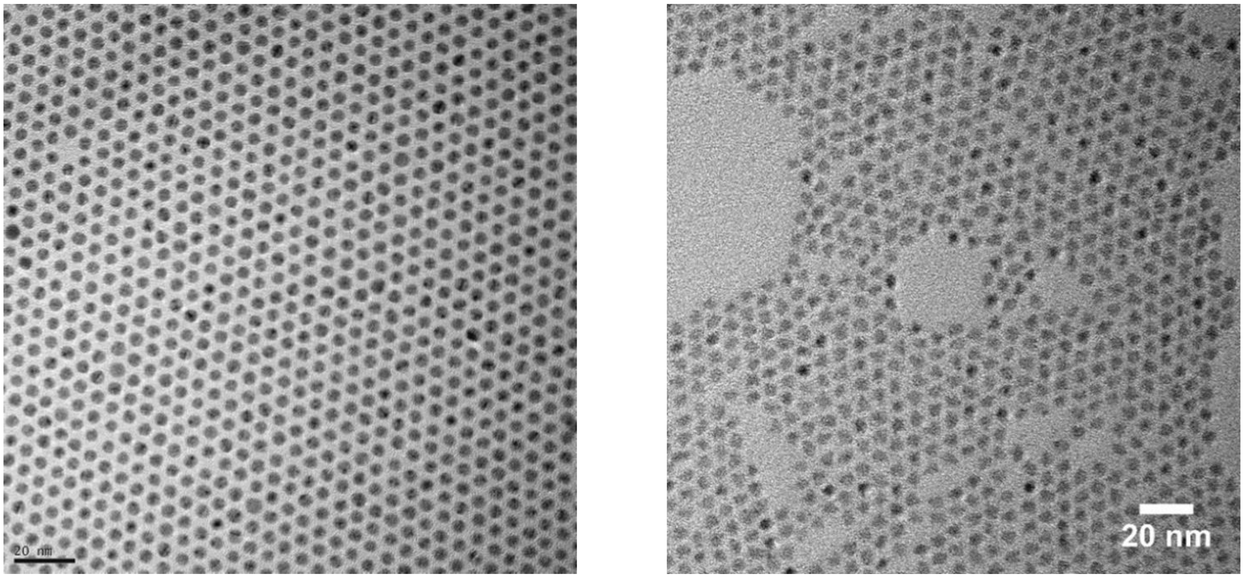

TEM micrograph of (left) 4.5 nm Au nanocrystals and (right) 4.6 nm PbS nanocrystals.

MCC Ligand Synthesis. All methods were performed in a nitrogen glovebox unless otherwise stated. Preparation of the MCC ligands was based on previously reported methods (*21*, *57*). In general, MCCs were prepared as 0.25 M or 0.5 M stock solutions in either hydrazine or N-methylformamide (NMF) by reacting metal chalcogenides with excess chalcogen in the desired stoichiometry. For hydrazinium ($N_2H_5^+$) based species, hydrazine can act as both solvent and redox mediator allowing synthesis directly from elements. For MCCs with other cations in non-hydrazine solvent, metal chalcogenides were reacted with the appropriate alkali metal chalcogenide (e.g. K_2S). *Caution: Special care should be taken when using hydrazine in exothermic reactions which can release hazardous, flammable vapors with a risk of detonation if heated in sealed containers.*

$(N_2H_5)_4Sn_2S_6$, $(N_2H_5)_4Sn_2Se_6$, and $(N_2H_5)_3AsS_4$: Synthesized as 0.25 or 0.5 M solutions in hydrazine with stoichiometric ratios of the appropriate elements and stirring for >24 hours. For example, a 0.25 M solution of $(N_2H_5)_4Sn_2S_6$ was prepared by adding Sn powder (2 mmol, 0.237 g), sulfur (6 mmol, 0.192 g), and 4 mL anhydrous hydrazine a 20 mL glass vial with a Teflon coated stirbar. The solution was stirred at room temperature for 48 hours to form a transparent colorless solution. A small amount of excess sulfur may be required for full dissolution of Sn.

$(N_2H_5)_2In_2Se_4$ and $(N_2H_5)_2Cu_4S_6$: Synthesized as 0.25 M solutions in hydrazine by reacting an appropriate metal chalcogenide with elemental chalcogen. For $(N_2H_5)_2In_2Se_4$, In_2Se_3 (1 mmol, 0.467g), Se powder (1 mmol, 0.079 g), and 4 mL of hydrazine were added to a 20 mL glass vial and stirred for 48 hours.

K_3AsS_3: A 0.25 M solution was prepared by adding As_2S_3 (0.5 mmol, 0.123 g), K_2S (1.5 mmol, 0.165 g), and 4 mL distilled NMF for 96 hours. Small amounts of residual solids were removed by filtration through a 0.2 μm PVDF membrane.

K_3AsS_4: A 0.5 M solution was prepared by adding As_2S_5 (1.0 mmol, 0.310 g) and K_2S (3.0 mmol, 0.331 g) were stirred in 4 mL distilled NMF for 96 hours. Small amounts of residual solids were removed by filtration through a 0.2 μm PVDF membrane.

$K_4Sn_2S_6$: SnS_2 was prepared from previously reported methods (*57*). A 0.25 M solution of $K_4Sn_2S_6$ was prepared by dissolving SnS_2 (2.5 mmol, 0.457 g) and K_2S (2.5 mmol, 0.276 g) in 5 mL of distilled NMF and stirring for 96 hours. Residual solids were first removed by centrifugation then filtration through a 0.44 μm PVDF membrane.

Exchange of Nanocrystal Surface Ligands. NCs were washed three times after synthesis using standard solvent/non-solvent combinations (e.g. toluene/ethanol). All steps for air sensitive particles including HgTe, Ni, and PbS were performed in a nitrogen glovebox. Au and Pd NCs were initially washed in air, then transferred into a nitrogen glovebox for storage. For metal particles, a pre-exchange thiol treatment was applied by adding ~10% v/v dodecanethiol to a solution of NCs to replace the native amine ligands. After 5 minutes of stirring, NCs were flocculated with ethanol and redispersed in hexane or toluene for subsequent two-phase ligand exchange. DDT capped metal particles phase transfer into MCC solutions in hydrazine or NMF slowly and are much more resistant to irreversible aggregation during phase transfer compared to NCs capped with the native ligands. PbS, CdSe, and HgTe were exchanged using native ligands.

For two-phase ligand exchange into polar solvents, NCs in either hexane or toluene were added to a bottom phase consisting of a 25 mM MCC ligand in polar solvent. Note that for exchange into NMF, hexane must be used as the non-polar phase as toluene is miscible with NMF. In a typical procedure, 100 mg of DDT capped Au NCs in 12 mL of toluene along with 4 mL of a 25 mM hydrazine solution of $(N_2H_5)_4Sn_2S_6$ were placed in a 20 mL vial with a Teflon coated stirbar. After ~12 hours of stirring, phase transfer completed and the clear non-polar top phase was discarded and washed with fresh toluene two times. The colloidal NCs in the hydrazine phase were then flocculated by addition of 1.5 mL of acetonitrile (ACN), recovered by centrifugation, and redispersed in 4 mL of hydrazine. The ligand concentration was then increased to 25 mM and stirred for an additional 12 hours with 8 mL of fresh toluene. The clear top phase was replaced with fresh toluene an additional two times. The NCs in hydrazine were then precipitated with a minimal amount of ACN three times (adding ~10 mM of MCC ligand during each washing cycle) and stored as a concentrated (~100 mg/mL) solution in hydrazine. Ligand exchange into NMF was performed similarly but precipitation of NCs required the use of ~1:2:1 NMF:ACN:toluene non-solvent mixtures.

Assembly of Inorganically Capped Nanocrystals. Au and Pd NCs were assembled in hydrazine by flocculation via addition of MCC ligand solution. In a typical procedure, ~1-20 μL of 0.5 M MCC ligand solution was added to a 40 μL aliquot of 100 mg/mL NC stock solution to a set final MCC ligand concentration between 10 and 150 mM. Above a critical concentration, a qualitative change in the appearance of the NC solution was observed within seconds as colloidal stability was lost and particles began to agglomerate into supercrystals. The critical flocculation concentration for a given sample varied with the MCC ligand used due to changes in anion valency (i.e., ionic strength).

Ni NCs with AsS_3^{3-} surface ligands were assembled in NMF by adding an excess of K_3AsS_3

ligands to induce flocculation. Due to the high dielectric constant of NMF, a large excess (>150 mM) of MCC ligand is required to induce assembly which is assisted by the relatively large hard sphere diameter (9 nm) of the NCs with relatively large vdW attractive potentials.

PbS and PbSe NCs with $Sn_2S_6^{4-}$ surface ligands were assembled in NMF by addition of excess K_3AsS_4 ligand solution and ACN. Using additional ligand concentration alone does not lead to SC formation and cannot easily fully flocculate NCs with small (<6 nm) diameters. PbS NC solutions were increased to 200 mM K_3AsS_4 in NMF and within minutes, additional amounts of ACN were added to either partially or fully flocculate the sample. In typical experiments, 20 µL of 0.4 M K_3AsS_4 solution was added to 20 uL of NC stock solution. The addition of >17 µL ACN (>30% v/v) lead to the complete precipitation of NCs into SCs over a period of seconds to minutes. Intermediate volumes of ACN (20-30% v/v) induced a phase separation into dilute fluid, dense fluid, and solid layers visible by eye. Solutions with <20% ACN remained colloidally stable for days in sealed capillaries with no visible aggregation.

CdSe NCs were flocculated in both hydrazine and NMF using an excess of MCC ligand concentration and ACN. In all cases, no SCs were observed over a wide variety of ligand concentrations, capping ligands, or NMF/ACN solvent mixtures.

1.2. Characterization Methods

UV-VIS-NIR Absorption: Steady-state optical absorption measurements were collected on a Varian Cary 500 UV-Vis-NIR spectrophotometer.

DLS: Dynamic light scattering data were collected using a Malvern Instruments Nano-ZS zetasizer.

PXRD: Wide-angle powder x-ray diffraction (PXRD) data was acquired on a Bruker D8 diffractometer using a 1.541 Å Cu K-α source and a Vantec 2000 array detector.

ICP-OES: Elemental analysis of nanocrystal samples was carried out by inductively coupled plasma optical emission spectroscopy on an Agilent 700 Series instrument. Nanocrystal samples were digested using 69.0% TraceSELECT grade nitric acid (Aldrich) and were diluted using ultrapure deionized water. For samples that did not dissolve completely in nitric acid, a small amount (500 ppm) of Br_2 (99.99% Aldrich) was added before dilution.

TEM: Transmission electron micrographs were acquired using a Tecnai F30 microscope at 300 kV accelerating voltage. Samples were imaged on 400 mesh copper grids with amorphous carbon support (Ted Pella). Local chemical characterization by electron energy loss spectroscopy (EELS) was conducted using an FEI Titan 3 microscope equipped with a GatanTridiem 863ER detector.

SEM: Scanning electron micrographs were obtained on a Zeiss Merlin scanning electron microscope with 5 kV accelerating voltage.

Reflectance: Reflectance spectra were obtained using a Cary 5000 with the universal measurement accessory (UMA). Spectra were measured off of the top surface of drop-cast films on sapphire substrates.

Transport: Resistivity measurements were made on a Quantum Design Inc. physical properties measurement system (PPMS). Room temperature resistivity values were determined via a 4-point geometry to minimize effects of lead and contact resistance. For temperature dependent transport studies, samples were cooled using liquid helium cycled through a Cryomech PT-410 He reliquifier and measured via a 2-point geometry (10 µm channel). Samples were cast as films onto insulating substrates with evaporated Ti/Au electrodes.

XRF: Elemental analysis data from x-ray fluorescence was collected using a Rigaku NEX DE instrument. Measurements were taken in a thin-film geometry where samples were prepared by drop-casting on Si substrates.

SAXS: Small-angle x-ray scattering data was measured on a SAXSLAB Ganesha instrument with a Cu K alpha source. Colloidal and supercrystal samples in hydrazine were measured either as powders sandwiched between two layers of adhesive backed polyimide film or in glass capillaries sealed first with paraffin wax, removed from the glovebox, then further sealed with epoxy. Note that hydrazine vapors will slowly degrade epoxy upon extended exposure. Samples in NMF were removed from the glovebox and either measured in flame sealed capillaries or sandwiched between polyimide film layers.

In situ SAXS: In situ SAXS data in Figure 2g were collected at the Stanford Synchrotron Radiation Lightsource (SSRL) at beamline 1-5 with a photon energy of 15 keV and beam size of 600x600 µm. In a nitrogen filled glovebox, a solution of 4.6 nm Au with $(N_2H_5)_4Sn_2S_6$ ligands in hydrazine was loaded into a 2 mm path length quartz cuvette with custom 200 µm thick windows. The cuvette was sealed using a rubber septum and parafilm, and a syringe preloaded with a solution of 0.5 M $(N_2H_5)_4Sn_2S_6$ in hydrazine was attached to the cuvette via Teflon tubing through the septum. The gas-tight apparatus was carefully moved into the beam path, and data was collected continuously while stirring the solution. The ionic strength was increased to 125 mM by slow addition of the ligand solution in 5 µL increments via syringe pump over a period of 2 hours.

Preparation of SAXS Samples. Assemblies of NCs could be measured either in raw solutions or as powders. For solution measurements in hydrazine, NC solutions were transferred to 1.1 mm OD glass capillaries (100 µm thickness) in the glovebox and sealed with melted paraffin wax. The capillaries were then removed from the glovebox and further sealed with epoxy. Note that hydrazine vapors will slowly degrade epoxy if placed in direct contact. Solutions in NMF were transferred outside of the glovebox and flame sealed in glass capillaries. Powdered samples were sandwiched between two layers of polyimide tape. Samples in hydrazine were first washed three times with pure ACN. The resulting clean pellet of SCs can then be ground into a powder by mechanical agitation with a plastic pipette tip and transferred to a polyimide film. Note that hydrazine is incompatible with polyimide-based materials and pure ACN should be used as a transfer agent.

2. Supplementary Text

2.1. Approximating the interparticle potentials using DLVO picture

In order to gain a conceptual understanding into the key parameters that determine the outcome of the assembly process, a useful starting point is the two-particle interaction potential. The simplest theoretical framework that can provide a qualitatively realistic description of the interparticle potentially for electrostatically stabilized colloids is Derjaguin-Landau-Verwey-Overbeek (DLVO) theory. Within DLVO, the interparticle potential is generally described as the combination of an attractive interaction due to dispersion forces (U_{DIS}) and a repulsive term due to electrostatic repulsion (U_{ES}). Here we introduce an additional term to correct for steric repulsion mediated by the ligands (U_{ST}) at very short interparticle separation (<0.4 nm). As a result, the total interparticle potential (Figure SN1-1) can be expressed as:

$$U_{ES} = U_{DIS} + U_{ES} + U_{ST}$$

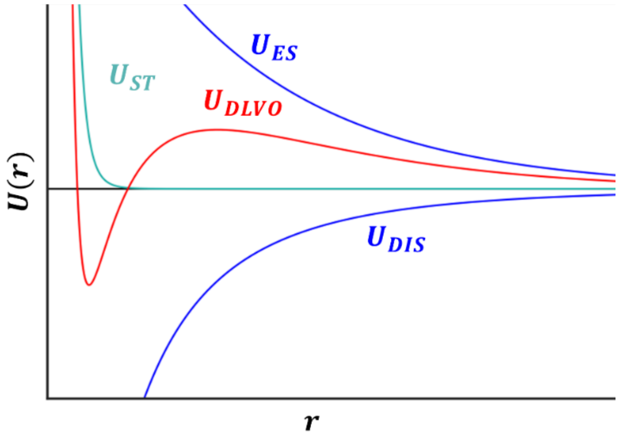

Figure SN1-1. Representative plot of DLVO forces in including electrostatic repulsion (U_{ES}), attractive dispersion forces (U_{DIS}), and steric repulsion (U_{ST}) as a function of interparticle separation, r.

The Dispersion Interaction

In the case of two uniform spheres, the total interaction mediated by dispersion forces has the following analytical result in the absence of retardation:

$$U_{DIS} = -\frac{A}{6}\left(\frac{2R_1R_2}{r^2-(R_1+R_2)^2} + \frac{2R_1R_2}{r^2-(R_1-R_2)^2} + ln\frac{r^2-(R_1+R_2)^2}{r^2-(R_1-R_2)^2}\right)$$

In the expression above R_i corresponds to the radius of the inorganic core of particle I and r is the center-to-center separation. A is the Hamaker constant that depends on the material and the medium through which the particles are interacting. In this case we used value of 1.6 eV for Au (*60*). Figure SN1-2 below shows the dependence of the strength of the dispersion interaction on the radius of the nanoparticle, indicated as expected a strong monotonic increase in the magnitude of the interaction as a function of the nanoparticle size. In the plot below and elsewhere the interparticle separation refers to the edge-edge separation of two nanoparticles.

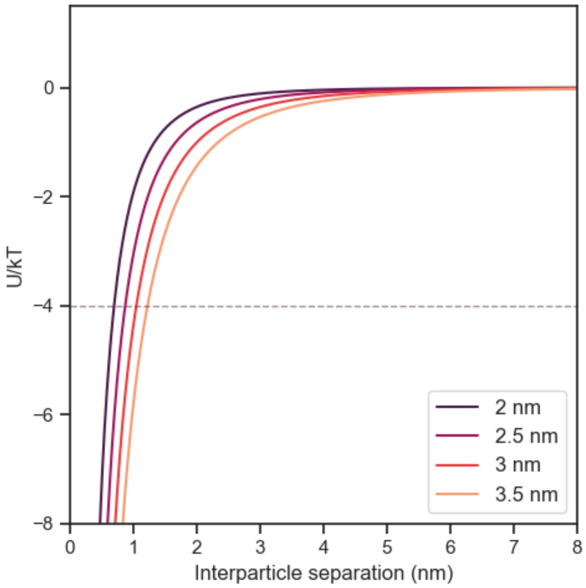

Figure SN1-2. Dispersion forces for Au NCs as a function of the interparticle separation for a range of NC radii.

The Electrostatic Interaction

In order to estimate the electrostatic contribution to the total interparticle potential, we use the analytical result for the electrostatic potential of two spheres in non-linear superposition approximation:

$$U_{ES} = \frac{64\pi k_B T c\gamma^2}{\kappa^2} e^{-\kappa r}$$

Where the term γ has the following form and even for moderate values of the surface potential (φ_0) rapidly approaches a value of 1.

$$\gamma = \tanh\left(\frac{ze\varphi_0}{4k_B T}\right)$$

In the expression above, κ is the Debye screening length and can be estimated as:

$$\kappa^{-1} = \left(\frac{\varepsilon_0 \varepsilon_{sol} k_B T}{e^2 \sum_{j=1}^{N} n_j^0 z_j^2}\right)^{1/2}$$

A related quantity that is important is the Bjerrum length, which can be expressed as

$$\lambda_B = \frac{e^2}{4\pi\varepsilon_0\varepsilon_{sol} k_B T}$$

Finally, the ionic strength defined as:

$$I_{sol} = \frac{1}{2}\sum_{j=1}^{N} c_j z_j^2$$

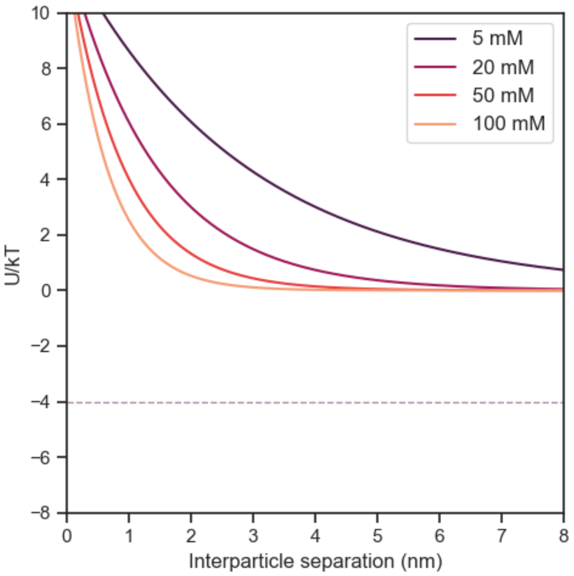

Figure SN1-3. Scaling of the electrostatic contribution to the interparticle potential for 2 Au NCs with a radius of 2.5 nm for different concentrations of a 1:3 electrolyte.

Putting together electrostatic and dispersion terms results in the following interparticle potentials shown in Figure SN1-4.

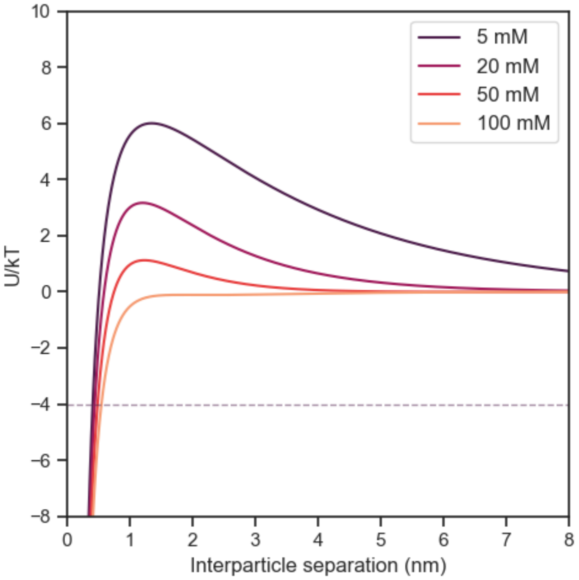

Figure SN1-4. Scaling of the interparticle potential for 2 Au NCs with a radius of 2.5 nm for different concentrations of a 1:3 electrolyte in the absence of a steric repulsion.

The Steric Interaction

In order to obtain more realistic results, a repulsive term needs to be added to account for the incompressibility of the system as one approaches the size of the ligand, which here we simply estimate as 0.3 nm. There are many functionals one can choose, but a sample result is shown in Figure SN1-5:

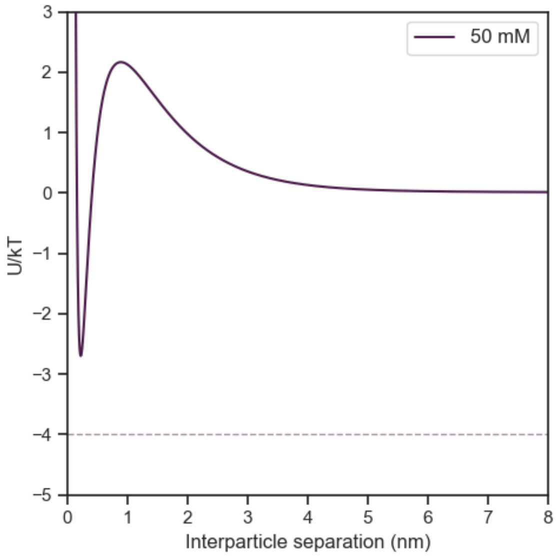

Figure SN1-5. Scaling of the interparticle potential for two Au NCs with a radius of 2.5 nm for at a concentration of 50 mM of a 1:3 electrolyte in the presence of a steric repulsion at a separation of ~0.3 nm.

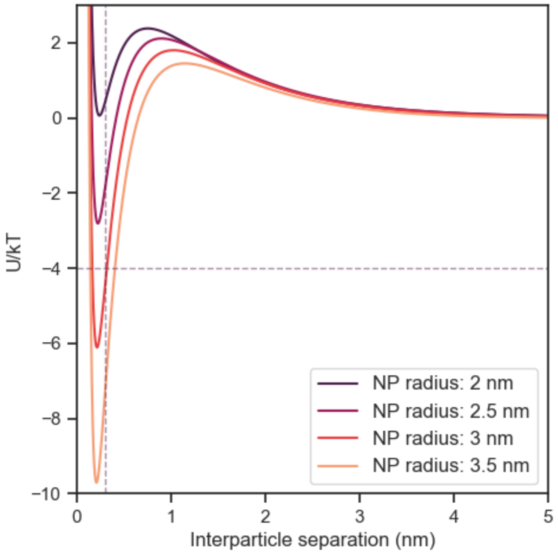

Figure SN1-6. Variation of the depth of the primary minimum for Au NCs of varying size at a constant dielectric constant of 172, 1:3 salt concentration of 150 mM in the presence of a short range repulsive barrier at 0.25 nm.

Interparticle potential range of attraction

In order to make a more direct the connection between the DLVO potential we computed and the square-well potential parameters discussed in the text, it is convenient to map the first potential onto the latter. While there is no unique way of carrying out this mapping, Noro and Frenkel (*26*) proposed one method to extract the equivalent square-well depth (u_0) and range of interaction (λ) for an arbitrary potential. As a natural choice, the well depth is set to the minimum of the potential. The range of interaction is then selected in such a way that the second virial coefficient (B_2) of the two potentials becomes identical. B_2 is defined as:

$$B_2(T) = -2\pi \int_0^\infty r^2\left[e^{-U(r)/k_BT} - 1\right]dr$$

We show the result of this mapping for the potential calculated in figure SN1-7 (specifically for the case of 100 mM $(N_2H_5)_4Sn_2S_6$ ligand in hydrazine for 4.5 nm Au NCs). Note that the square well potential was shifted for the onset of the repulsive regime at small separations to coincide with that of the DLVO potential. This procedure yields a range of interaction of 0.09, supporting the hypothesis that the real potential is in the regime of a very short range of interaction.

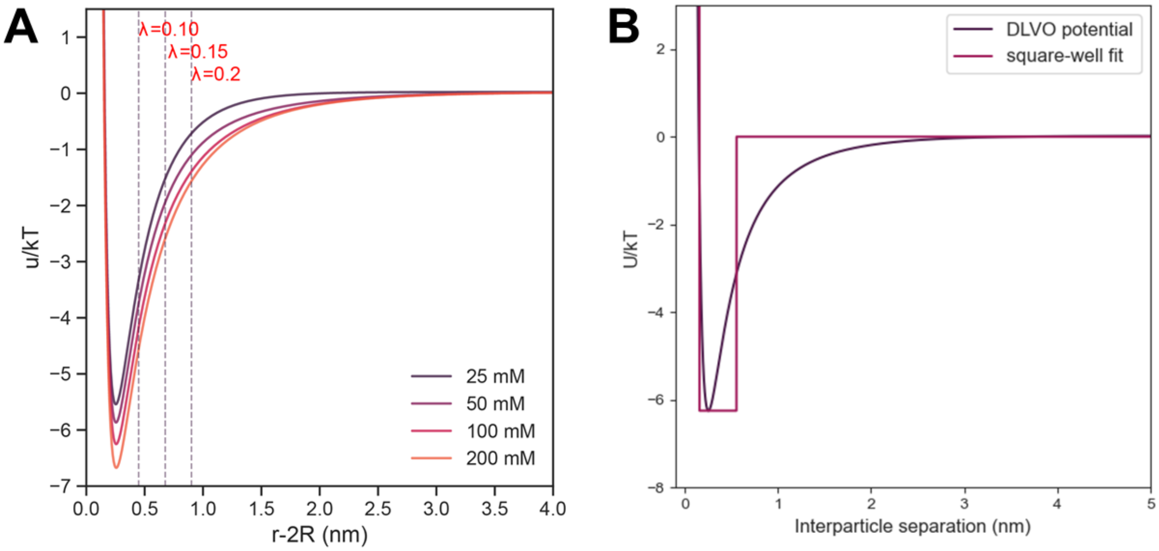

Figure SN1-7. DLVO potential range of attraction. (**A**) Identical data from the main text Figure 2A overlayed with ranges of attraction (λ) for 4.5 nm diameter Au NCs in hydrazine. (**B**) Square-well potential mapped onto the DLVO potential by matching second virial coefficients for 4.5 nm Au NCs at 100 mM with a 1:3 valent salt. The square-well potential has a width of λ=0.09.

2.2. Phase coexistence and nucleation pathways

When a stable colloid of electrostatically stabilized particles is destabilized, e.g. through an increase in the ionic strength, the outcome is generally one of three possibilities on experimentally relevant timescales:

1. Gelation/amorphous aggregation
2. Crystallization
3. Formation of a metastable fluid

These experimental outcomes can be conveniently mapped on a reduced form of the interparticle potential (i.e. the square-well approximation) in terms of the depth (u_0) and range of the attraction (λ) as shown in Fig. 2C of the main text.

Case 1: $u_0 > 5k_BT$

The existing literature on electrostatically stabilized nanoparticles (and especially that on metal sols) indicates that the first regime is by far the most commonly encountered. For example, if a stable colloid of metal nanoparticles is destabilized, the usual outcome is to produce disordered open fractal assemblies. The exact nature of these glassy assemblies depends on the relative timescales of diffusion (τ_D) and coalescence (τ_C) (*61–63*). The fastest regime, called diffusion limited aggregation (DLA) is marked by the condition that $\tau_D \gg \tau_C$ the condition the coalescence of particles occurs effectively instantly when two particles fall within the mutual capture cross-section. Under these conditions, aggregation generally leads to open worm-like structures. In the next regime, called reaction limited aggregation (RLA), the rate of coalescence becomes comparable or smaller than the rate of diffusion. Typically, assembly under these conditions creates fractal-like aggregates that are denser than the structures obtained under DLA as shown in Figure SN2-1. The nature of these open aggregates can be put on a more quantitative footing by extracting the dimensionality factor (D) from small angle X-Ray scattering (SAXS). In the case of DLA, d tends be in the range of ~1.8, while in the case of RLA a typical value is about ~2.
Only when extensive rearrangement can take place does the dimensionality factor increases to 3 or above. As the degree of reversibility increases, the system tends to form increasingly denser aggregates. When the dimensionality factor increases to 4, the system can no longer be considered to be a mass or surface fractal but can be described as a smooth volume at length scales much larger than the NC radius. However, an important point that must be emphasized is that this coarse-grained smoothness does not allow one to distinguish between compact aggregates and crystals. The latter distinction can only be made by analyzing the higher q region corresponding to a length scale smaller than the interparticle separation (see Figures SN2-1 and SN2-2).

Case 2: $u_0 < 5k_BT$, $\lambda < 0.2$

As the depth of the interparticle potential decreases, the system gains enough micro-reversibility that dense aggregation can go hand in hand with the formation of long-range ordered structures. Thermodynamically, the formation of close-packed structures is favorable due to both entropic (*64*) and enthalpic (*65*) contributions. However, there are multiple pathways the system can take to reach that final state. One way to categorize such pathways is as 1) one-step or 2) multi-step processes. The first case is best known as a manifestation of classical nucleation theory (CNT). In this simplest case density fluctuations lead to the formation of small crystallites, which upon reaching a critical size can become the nuclei for the formation of arbitrarily large crystal.

The second category of "non-classical" multi-step nucleation pathways can be much more diverse. One important example, highlighted by both simulations and experimental work is a two step-process where the system first partitions into two metastable fluids, with one phase being significantly denser. The second step then involves the transition of the dense fluid phase into a crystalline solid. Our simulations (see Figure SN2-3) show the appearance of such a trajectory, consistent e.g., with the simulations previously reported by Haxton *et al.* (*25*). As described in the main text, this situation is especially relevant to systems interacting via a short-range attraction potential where the range of interaction is much smaller than the particle radius. The reason for this effect is illustrated in Figure SN2-4. When the interparticle potential is long range, there are three equilibrium phases: a gas, fluid, and a solid. As a result, a solid can nucleate either from the gas or fluid depending on the temperature. On the other hand, as the range of interaction becomes shorter, only two phases remain, namely a fluid and a solid. However, a fluid-fluid coexistence line continues to exist in this regime, albeit as a metastable binodal line below the fluid-solid coexistence line. Our observations suggest that many of our experiments occur exactly in this regime, as best illustrated by the behavior of PbS NCs in NMF.

Case 3: $u_0 < 5k_BT$, $\lambda > 0.2$

As the range of interaction becomes long, a situation can arise where instead of forming aggregates, the nanoparticles become kinetically trapped as a metastable fluid. Such a fluid can persist arbitrarily long depending on the specific experimental parameters. This behavior is represented as Region III in Figure 2C.

Case 4: $u_0 < 1.5k_BT$, $\lambda > 0.25$

At even longer interparticle interaction ranges and small u_0, nanocrystals can condense into a stable liquid phase which is thermodynamically stable compared to the crystalline phase. This is represented as Region V in Figure 2C.

Methods for Figure SN2-1 Simulation

A Diffusion Limited Aggregate (DLA) was constructed with a Brownian Tree algorithm (*66*) from 1000 diffusive particles interacting via a Lennard-Jones potential U_{LJ}

$$U_{LJ}(r) = 4\epsilon_{LJ}\left[\left(\frac{\sigma}{r}\right)^{12} - \left(\frac{\sigma}{r}\right)^{6}\right]$$

with energy and length units ϵ_{LJ} and σ and with a friction coefficient γ with a thermal bath with Boltzmann constant times temperature such that $\epsilon_{LJ}/k_BT = 1$. The Lennard-Jones potential was cut off and shifted to zero at 2.5σ. The simulation started with a seed particle at the origin and successive particles each starting their Brownian diffusion from one of the eight vertices of a cubic box of length 215σ placed symmetrically around origin and aggregating on encountering the growing DLA through the Lennard-Jones interaction. After full construction of the DLA, an energy minimization was performed for $11\gamma\sigma^2/\epsilon_{LJ}$ in the natural time units with each time step being $10^{-3}\gamma\sigma^2/\epsilon_{LJ}$.

For simulating a disordered compact aggregate, first a periodic box of 27000 Lennard-Jones interacting particles was equilibrated with Brownian dynamics at $\epsilon_{LJ}/k_BT = 2.5$ and density $\rho = 0.85/\sigma^3$ for $100\gamma\sigma^2/\epsilon_{LJ}$ time units. Then a droplet of 19619 particles was carved out around the origin and its energy was minimized for $2\gamma\sigma^2/\epsilon_{LJ}$. This resulted in the jammed and approximately spherical disordered aggregate.

The pristine superlattice of 19619 particles was built layer-by-layer using FCC lattice vectors. All SAXS patterns were simulated after mapping the Lennard-Jones repulsion range $2^{1/6}\sigma$ to the experimental nanocrystal diameter.

Methods for Figure SN2-3 Simulation

The self-assembly simulation was performed with underdamped Langevin dynamics at xed volume using the LAMMPS software (*67*). The nanocrystals were represented as 10976 spherical particles in a cubic periodic box. The particles repel each other with a Weeks-Chandler-Andersen potential (*68*), U_{WCA},

$$U_{WCA}(r) = \begin{Bmatrix} 4\epsilon_{LJ}\left[\left(\frac{\sigma}{r}\right)^{12} - \left(\frac{\sigma}{r}\right)^{6}\right] + \epsilon_{LJ}; r \le 2^{1/6}\sigma \\ 0;\ r > 2^{1/6}\sigma \end{Bmatrix}$$

with energy and length units ϵ_{LJ} and σ, and attract each other with a Morse potential, U_M

$$U_M(r) = \epsilon\left(e^{-2\alpha(r-r_0)} - 2e^{-\alpha(r-r_0)}\right)$$

with a well-depth ϵ, inverse range $\alpha = 5/\sigma$, location of well $r_0 = 1.23\sigma$ and the potential being truncated and shifted to zero at 3σ. The Langevin dynamics algorithm uses a friction unit γ with the natural time units of the system being $\tau = \gamma\sigma^2/\epsilon_{LJ}$. Temperature, density, mass of particles, and timestep were chosen to be ϵ_{LJ}/k_B, $0.01/\sigma^3$, $\gamma^2\sigma^2/\epsilon_{LJ}$, and $5 \times 10^{-5}\tau$ respectively. The system was equilibrated in gas phase at $\epsilon = 1$ in units of k_BT, adiabatically quenched to $\epsilon = 2.5$ and then evolved to undergo self-assembly, mimicking the instantaneous ligand addition.

The growth of order was tracked with order parameters reporting on density and crystalline order. The largest cluster was detected by analyzing nearest neighbors with a cutoff on interparticle distances $r_c = 1.5\sigma$. Crystalline order was detected with the bond-orientational $\psi_6^{(i)}$ order parameter, for particle i being defined as

$$\psi_6^{(i)} = \frac{1}{n_i}\sum_{j\epsilon n_i}\left[\frac{\sum_{m=-6}^{6} q_{6m}^{(i)}\, q_{6m}^{(j)*}}{\left(\sum_{m=-6}^{6} q_{6m}^{(i)}\, q_{6m}^{(i)*}\right)^{1/2}\left(\sum_{m=-6}^{6} q_{6m}^{(j)}\, q_{6m}^{(j)*}\right)^{1/2}}\right]$$

with

$$q_{6m}^{(i)} = \frac{1}{n_i}\sum_{j\epsilon n_i} Y_{6m}\left(\phi_{ij}, \theta_{ij}\right)$$

where the sum over $j \in n_i$ includes neighbors within $\left|\boldsymbol{r}_i - \boldsymbol{r}_j\right| < 1.5\sigma$, and $Y_{lm}(\phi_{ij}, \theta_{ij})$ is the l-m spherical harmonic function associated with the angular coordinates of the vector $\boldsymbol{r}_i - \boldsymbol{r}_j$. A locally crystal-like particle was defined as having a value of $\psi_6^{(i)}$ higher than a cutoff value 0.7 (*69*). Neighboring ordered particles were grouped together into an ordered cluster. Growth of the largest cluster size N_α with and without considering crystalline order was tracked as a function of simulation time to reveal the separation in timescale between aggregation and crystallization.

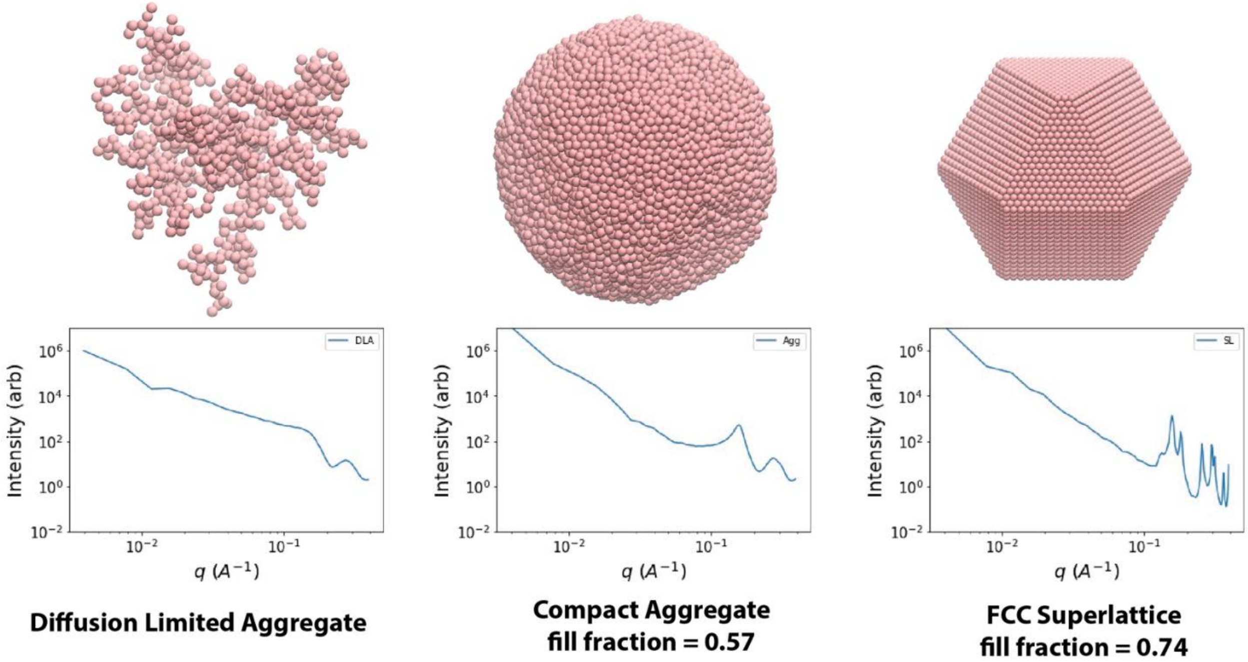

Figure SN2-1. Simulations of different qualitative outcomes of assembly experiments, including (fractal) diffusion limited aggregates, compact aggregates, and crystalline supercrystals. The top plot shows the real space image and the bottom the computed scattering factor obtained by convolving the structure factor calculated for each simulation with the form factor of the sample.

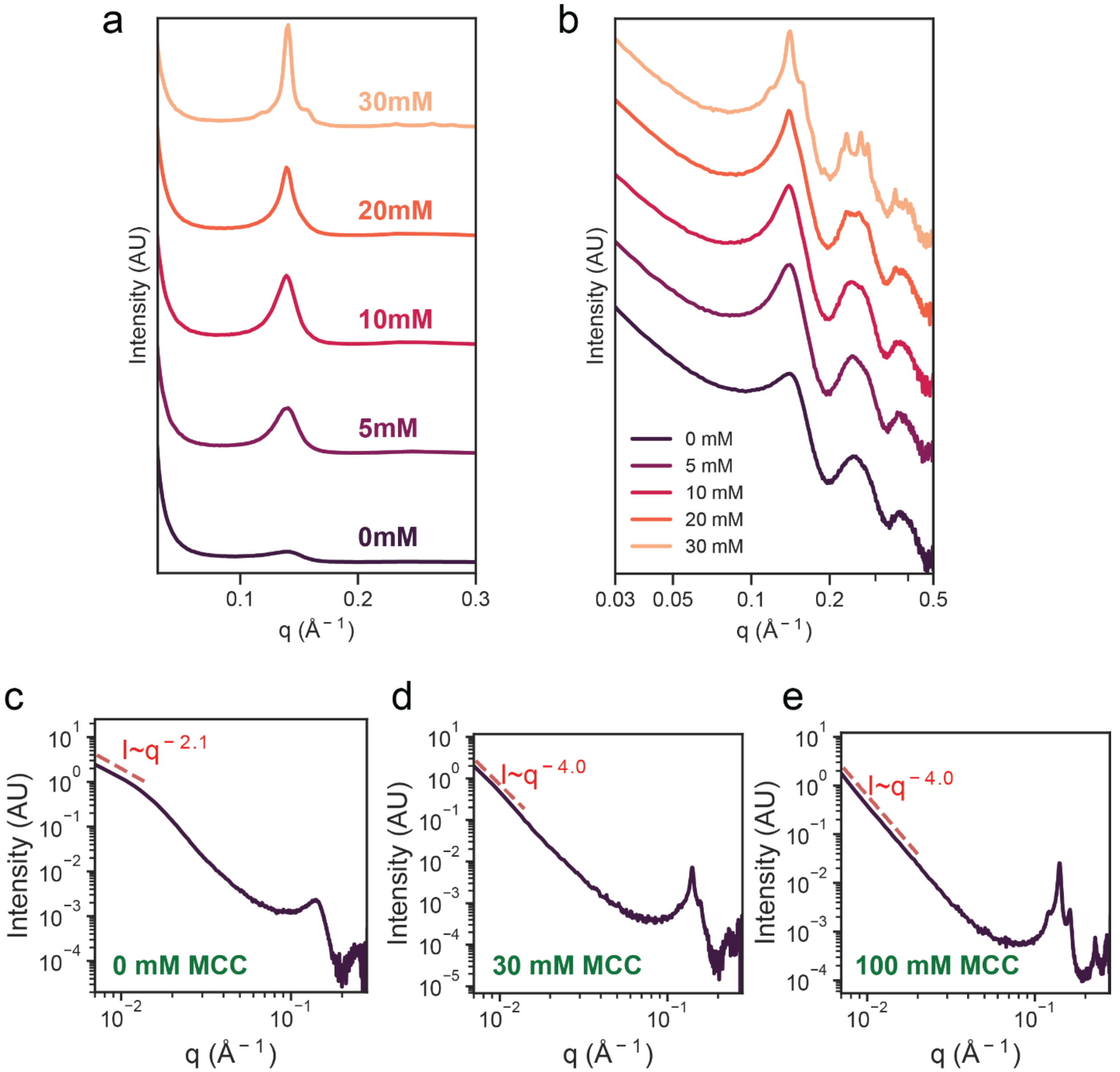

Figure SN2-2. SAXS data for 4.2 nm Au-Sn_2S_6 NCs flocculated by adding $(N_2H_5)_4Sn_2S_6$ to a given concentration and then flocculating the sample to a solid by adding small amount of acetonitrile, plotted on **(a)** linear and **(b)** log scales. Particles flocculated with ACN alone show a power law behavior with an exponent of 2.1 indicating fractal-like aggregates **(c)**, while particles flocculated with **(d)** 30 mM MCC + ACN and **(e)** 100 mM MCC + ACN exhibit an exponent of 4.0, consistent with scattering from smooth solids, with high degrees of crystallinity from the sharp peaks at higher q.

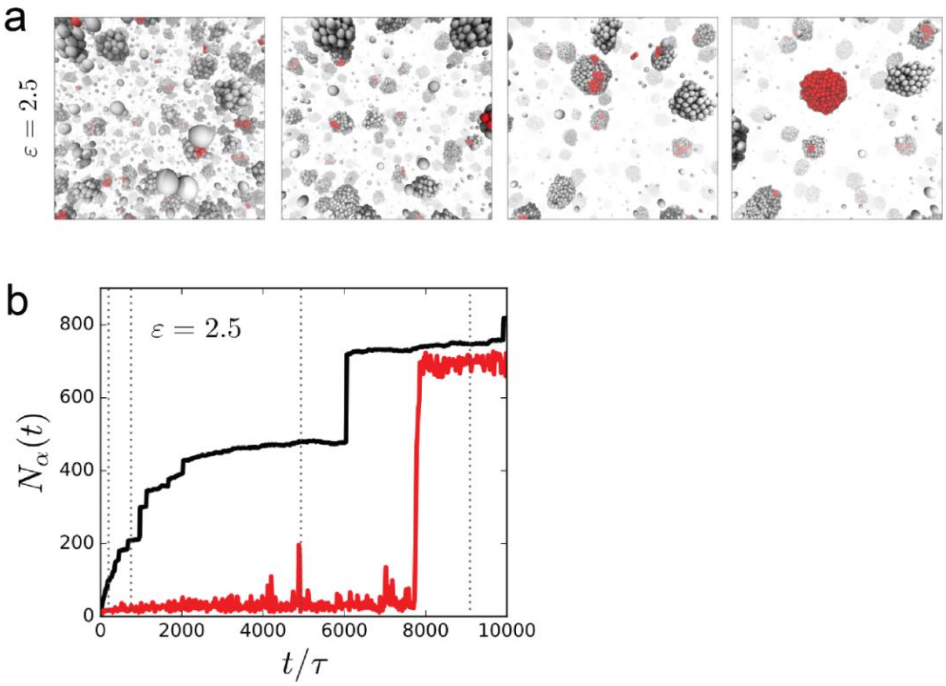

Figure SN2-3. Simulation of NC assembly under conditions leading to two-step nucleation. **(a)** Snapshots show locally ordered colloids as red, while disordered colloids are grey (based on a standard orientational order parameter, Q6). **(b)** The time-series plots the number of particles in the largest cluster, N_α, where the black line is the size of the aggregated cluster and red is the number of ordered particles. A separation of timescales between aggregation and ordering is observed, evident in the initial increase in the number of disordered particles in the largest cluster, followed by an abrupt nucleation event where order grows in.

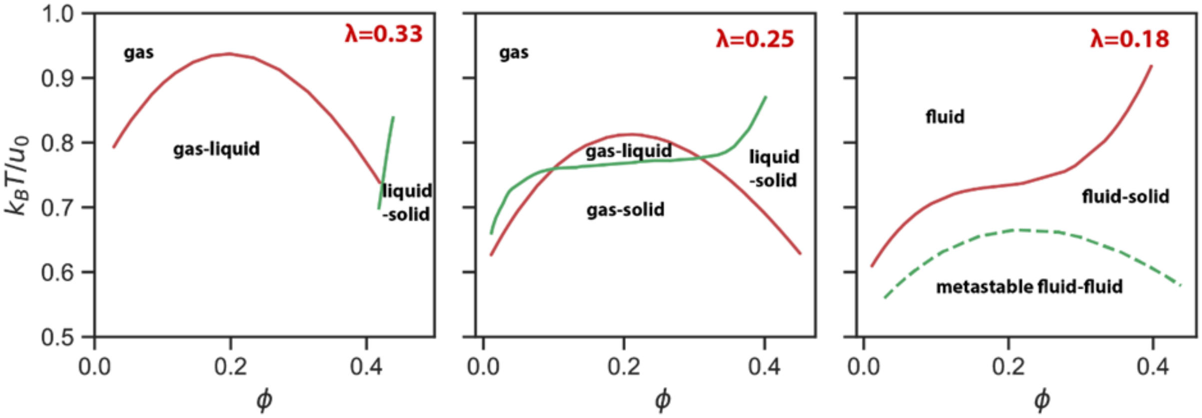

Figure SN2-4. Phase diagrams at various values of the range of interaction (λ) showing the formation of a metastable binodal line outlining a metastable gas-liquid coexistence region (right) for NCs with short, attractive interaction potentials $U(r) = 4\varepsilon_{vdw}\left[\left(\frac{\sigma}{r-\Delta}\right)^{12} - \left(\frac{\sigma}{r-\Delta}\right)^{6}\right] + A\frac{\exp(-\kappa r)}{r}$. Data reproduced from ref (*25*).

2.3. Molecular dynamics simulation model and methods

Surface polarization effects due to dielectric mismatch between the nanocrystals (NCs) and the solvent on the ion-NC binding

To investigate how the dielectric mismatch between the NCs and solvent influences the ion-NC binding and the NC-NC effective interaction at close contact (as shown in Figure 2D in the main text), we employed a minimal model that takes into account the induced charges on the NP surface due to dielectric mismatch and captures the effective interaction between the ion-ion and NC-ion. In our previous studies, we have shown that the ion-ion effective interactions (i.e., their potential of mean forces) depend on the salt concentration and ion valency in a nontrivial manner (*70*). Because in the present study the NC-NC interaction appears to be persistent for different multivalent anions ($Sn_2S_6^{4-}$, $Sn_2Se_6^{4-}$, $In_2Se_4^{2-}$ and AsS_4^{3-} and $Cu_6S_4^{2-}$), we chose to use a generic model for the ion-ion potential of mean force that incorporates the excluded volume interaction and electrostatic interaction:

$$U(r) = 4\varepsilon[(\sigma/r)^{12} - (\sigma/r)^{6} + 1/4] + Z_i Z_j \exp(-\kappa_D r)/r,$$

where the first term corresponds to the purely repulsive Weeks-Chandler-Anderson potential with characteristic length σ (approximately 0.5 nm) and energy ϵ (approximately 20 kJ/mol). The second term corresponds to the screened Coulombic interaction between two charged particles, Z_i and Z_j are the anion valency. The screening length $1/\kappa_D$ for the 1:1, 1:2, 1:3 and 1:4 salt concentrations from 50 mM to 150 mM in bulk hydrazine ($\varepsilon_r = 53$) and NMF ($\varepsilon_r = 177$) under investigation varies from 1.0 nm to 0.5 nm. Nevertheless, we note that the dielectric constant of the medium near the NC is typically much smaller than in bulk due to confinement effects (*71*). Therefore, we chose the Debye length $1/\kappa_D = 4\sigma$ (approximately 2.0 nm) to characterize the weekly screened electrostatic interaction between the ions near the NC surfaces.

The NCs do not carry inherent charge but have varying dielectric constants from 10 (dielectric) to 200 (to approach a metal-like behavior). Due to the dielectric mismatch between the NCs and the medium, the surrounding ions polarize the NC surface leading to nonzero induced charges. In our model, we solve for the induced charges at the NC surfaces using the image change method as implemented in our recent work (*72*).

Using the model, we attempt to evaluate the NC-NC effective interaction as the free energy profile along the center-center distance between the two nanocrystals in the presence of surrounding multivalent ions. To facilitate the sampling of the free energy profile of the NC-NC distance, we employ the constrained simulation method, where the NCs are fixed in space at varying center-center distances, only the anions (modeled as smaller spheres) are mobile (Figure 2D). Due to the symmetry of the reaction coordinate (i.e. the NC-NC distance), the average work needed to keep the two NC at any given distance is equal to the average force experienced by the NCs in the center-to-center direction (*73–75*).

Alternately, the free energy difference can also be given by the change in the potential energy of the whole system under constraint:

$$\Delta G(r) = k_B T \log \frac{P_{eq}(r)}{P_{eq}(r_0)} = k_B T \log \frac{P_c(r)}{P_c(r_0)} + k_B T[\log\ w_c(r) - \log w_c(r_0)] \approx E_c(r) - E_c(r_0)$$

where $P_{eq}(r)$ is the equilibrium probability of observing the NC-NC distance r in the canonical ensemble, the $P_c(r)$ is the probability of observing the NC-NC distance given the hard constraint, and $k_B T$ log$[w(r)]$ is the work needed to impose the constraint. The last approximation is possible because of two reasons:

First, the constrained probability $P_c(r)$ is proportional to the Boltzmann weight of the potential energy of the configurations under the constraint:

$$P_c(r) \sim \int \mathrm{d}r\,' \exp(-E\,(r')/k_B\,T)\delta(r' - r) = \exp(-E_c\,(r)/k_B\,T).$$

Second, the change in the imposed work $W(r) = k_B T \log\,[w_c(r)]$ over the distance of interest is negligible to the first term. Indeed, to make the whole system in equilibrium with a bulk salt solution, we need to impose a work W to pull the anions from the bulk solution to pack them into the given simulation box volume. The simulated system (the NCs and the anions) and the implicit salt bulk solution are in equilibrium and charge neutral. The constraint work certainly depends on the chemical potential of the cations (or anions) in the bulk salt (which is a function of temperature and salt concentration), and the constrained ion concentration in the box. If the box dimensions, L, are sufficiently larger than the NC-NC distance range of interest, it is reasonable to expect that $W(r)$ is independent of r such that the difference $W(r)$–$W(r_0)$ is small compared to the first term. As a result, we set $L_x = 100r_{max}$; $L_y = L_z = 10r_{max}$, where the maximum NC-NC distance of interest $r_{max} = 1.4D_{NC}$.

The anions are equilibrated in the constant temperature and volume using the Langevin thermostat. The anion density profiles are measured and averaged over our production runs. The forces on the NC are measured along the center-center vector between the two NCs every 100 timesteps and averaged the course of 10^6 timesteps in our production runs. In our simulation, the reduced time unit is defined as $\tau = \sigma(m/\epsilon)^{1/2}$, where m is the ion mass being the mass unit. The long-range contribution of the Coulombic interaction is computed via the particle-particle particle-mesh algorithm. Our simulations were performed using LAMMPS, an open-source MD software package (*67*).

Figure SN3-1 shows the potential energy change as a function of the center-center distance between two NCs, r, normalized by the NC diameter, D_{NP}. The change in the potential energy is indeed consistent with the free energy profile computed from the average force shown in Figure 2E, confirming that both approaches yield similar effects of surface polarization on the NC-NC effective interaction (potential of mean force) at short range.

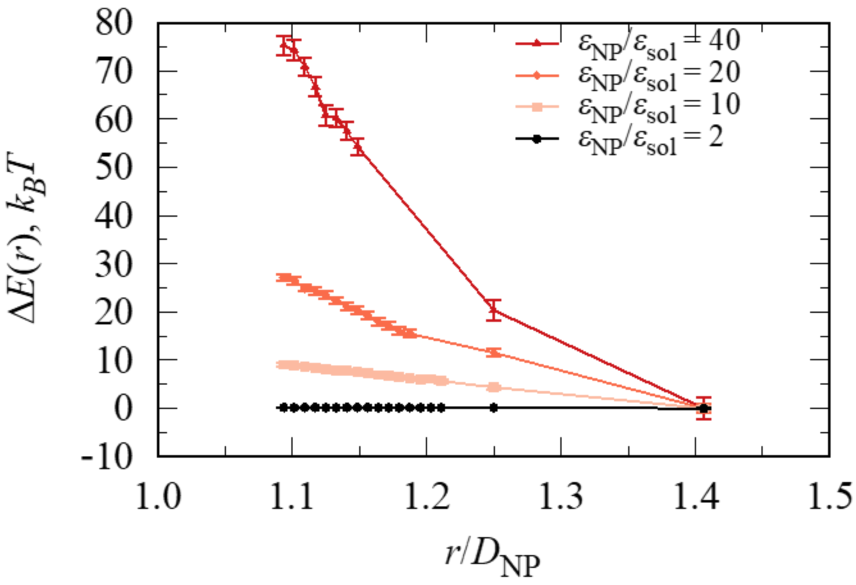

Figure SN3-1. Potential energy change as a function of the center-center distance between the NPs.

Radial density profiles of the anions from the above-mentioned simulation protocol

We compute the radial density profiles in Figures S24 and S25 by binning the anions based on their distance to the NC center. The radial density profiles are time averaged over 50 snapshots with time interval of 10τ. For high dielectric constants (ϵ_{NC} = 100 and 200), where the surface polarization effects are the strongest, we performed parallel tempering simulations with 16 replicas each with a temperature $k_B T/\varepsilon$ in the range of 0.8 – 2.3 to ascertain that the simulation results are not biased by initial configurations. The temperature swaps between adjacent replicas were attempted every 1000 time steps, or 1 time unit. The system configurations obtained at individual temperature were subsequently used to compute the ensemble averages of the anion density profiles.

Our simulation results show that for the metallic NCs (Figure 2D, left) the condensed counterions form a dense layer on the NC surface, whereas for the dielectric NCs (Figure 2D, right) the counterions are loosely attracted to the NC surface. This is because the dielectric mismatch between the NCs and their ionic environment is larger for the metallic NCs than for the dielectric NCs, leading to stronger polarization effects at the metallic NC surface. The polarization effects are manifested by greater values of the surface induced charges, attracting more anions toward the NC surface. This is in line with our previous work on the polarization effects of dielectric nanoparticles in asymmetric charged solutions (*37*). The radial density profiles of the anions for varying dielectric constants of the NCs (Figure S24) indeed reveal that as the NC dielectric constant increases (i.e., as the NCs become more metallic), the anions form more dense layers next to the NC surface. Regardless of the NC distances, the condensed anion layers remain relatively intact, which indicates that the driving force for the counterion condensation results from the attraction between the anions and the induced charges at the NC surface arising due to polarization effects. As the anion valency is decreased, the surface induced charges are reduced, leading to a loosely packed condensed anions (Figure S25), which again is consistent with experimental observations when monovalent anions are used in place of multivalent anions.

The key finding from our minimal model and surface polarization-included simulation is that the NCs with higher dielectric constants would attract more anions, and hence have higher surface charge densities. The enhanced accumulation of the multivalent anions in turn leads to stronger repulsive forces exerted on individual NCs as the NC dielectric constant increases. For dielectric NCs, the repulsive force does not change with the NC-NC distance, whereas the short-range repulsion between the metallic NCs increases substantially as they approach each other. We argue that it is the repulsive force component at short range that reduces the attraction well depth between the NCs, and thus prevents the formation of the kinetically arrested, branched aggregates.

Metastable fluid-fluid coexistence simulations

Based on the results from the surface polarization effects on the ion-NC binding and NC-NC effective interaction, we employ a minimal coarse-grained model that allows us to investigate the effects of the interaction range and attraction well depth on the metastable fluid-fluid coexistence. Specifically, we use the hard-core attractive Yukawa potential (*76*) that was shown to exhibit similar phase behaviors with our system in that the coexistence of low-density and high-density fluids is present at a lower temperature than the fluid-solid coexistence point. For NCs with a low dielectric constant and those in monovalent salts, the short-range repulsive force between the NCs is weak and the electrostatic attraction between ion-adsorbed NCs are strongly screened, the attraction well is expected to be deep. For NCs with higher dielectric constants and those in multivalent salts, the attraction well is shallower.

We have performed Gibbs ensemble Monte Carlo (GEMC) simulations for different attraction ranges and starting from different initial densities (Figure SN3-2). The total particles in two simulated boxes in a single simulation, N, is fixed. In the GEMC simulations, there are three types of trial moves: 1) particle displacement within the two boxes; 2) box volume exchange under the constraint that the total box volume $V = V_1 + V_2$ is fixed; and 3) particle exchange between two boxes. We strictly followed the algorithm described in ref. (*77*). Our GEMC code can be accessed at https://bitbucket.org/ndtrung/basicmc/src/master/. For different initial densities from $\rho_0 = 0.35\sigma^{-3}$ to $\rho_0 = 0.48\sigma^{-3}$, we varied the total number of particles from $N = 350$ to $N = 480$. Our simulation results are consistent with previous studies, showing that as the attraction range decreases, the metastable fluid-fluid coexistence shifts to lower temperatures. Additionally, the high-density fluid branch shifts to higher values (closer to the solid phase), indicating that the fluid-fluid coexistence is metastable, and dependent upon the initial state point.

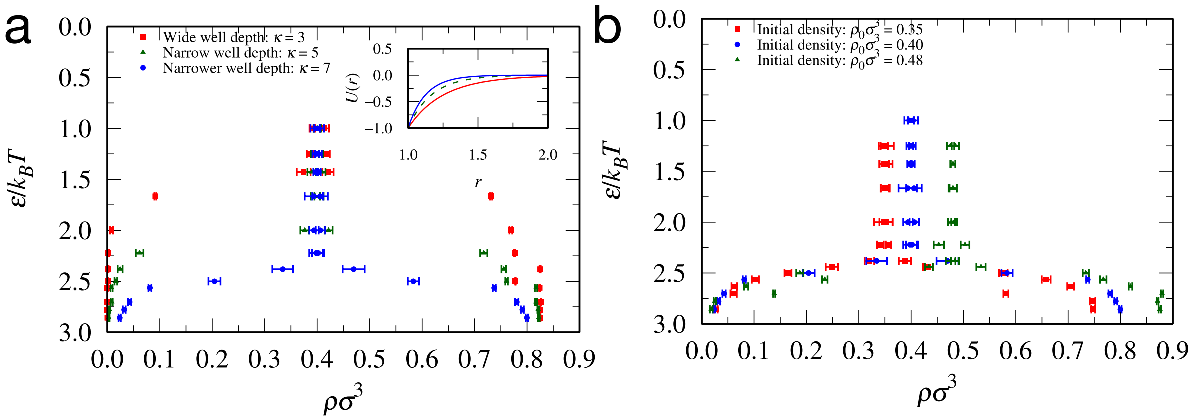

Figure SN3-2. Gibbs ensemble Monte Carlo simulation results for hard-core attractive Yukawa systems for (a) for different well depths and (b) for different initial densities.

Coarse-grained model and simulation of self-assembly

To ascertain that the self-assembled structures by the NCs are rather insensitive to the specific form of the NC-NC effective interaction, but to the attractive well depth and range, we consider a generic interaction potential, analogous to the DLVO potential:

$$U(r) = 4\varepsilon_{vdw}\left[\left(\frac{\sigma}{r-\Delta}\right)^{12} - \left(\frac{\sigma}{r-\Delta}\right)^{6}\right] + A\,\frac{\exp\left(-\kappa r\right)}{r},$$

where the first term represents the excluded volume interaction and short-range repulsion due to polarization effects, the second term to the attractive part that decays similarly to the regular dispersion forces. The parameter Δ is used to control the range of the short-range repulsion relative to the NC effective diameter σ. The last term, which is in the Yukawa potential, represents the electrostatic repulsion between the ligand-coated NCs in the given Debye screening length $1/\kappa$. The attractive well depth is dictated by the ratio between the electrostatic repulsion strength A and the attractive strength ε_{vdw}, as can be seen in Figure S26a. In this coarse-grained model, the ligand-coated NCs are modeled as spherical particles, whereas all the solvent molecules and salt ions are treated implicitly. From experimental estimates of the ligand coating layer and anion sizes, we chose $\Delta = 0.2\sigma$ and $1/\kappa = 0.25\sigma$. In these simulations, the NC effective diameter is set to be $\sigma = 1.0$. The reduced temperature $k_BT/\varepsilon_{\text{vdw}} = 1.0$ is fixed during the simulation.

Using Molecular Dynamics simulations in the canonical ensemble (constant temperature and particle density), we found that for $A/\varepsilon_{\text{vdw}} = 1$ the NCs spontaneously form gel-like structures at low and moderate number densities (Figure S26b). This is because the NC-NC net attraction is much stronger than thermal fluctuations; consequently, the NCs are kinetically trapped in the gel-like morphologies and cannot re-arrange into nanostructures with lower potential energies. For high values of $A/\varepsilon_{\text{vdw}}$, we perform a computer experiment where a thick slab of a face-centered cubic (*fcc*) solid slab is slowly melted by raising the temperature step by step. We observe that when a crystalline (*fcc*) phase is close to the melting temperature, the solid phase remains stable in contact with a high-density liquid (Figure S26c), for instance, within 10^4–10^5 time units for

$A/\varepsilon_{\mathrm{vdw}} = 10$. As the solid phase gradually melts away into a liquid phase with a remarkably lower density beyond this time scale, it is possible that the high-density liquid wetting the solid surface during the early melting stage is a metastable state, which is consistent with the coexistence reported in Figure 3A in the main text, and with the metastable fluid-fluid coexistence suggested by previous studies (*25*, *76*).

2.4. Calculations of interparticle resistance and supercrystal size for Figure 4A

Estimating the crystalline domain size

The crystalline domain size ($\overline{N}$) was determined in different way for different types of samples. In all cases, N was taken as the volume of the crystalline domain divided by the volume of the constituent nanoparticle. For samples with a small degree of ordering, the autocorrelation function (ACF) of real space images (TEM or SEM) was used to determine $\overline{N}$ by defining the bound of the crystalline domain as the point at which the ACF decreased to 10% of the initial value (Figure SN4-1). For highly crystalline super-crystals showing clear faceting, the crystalline domain size was taken to be the total volume of the super-crystals as quantified using electron or optical imaging.

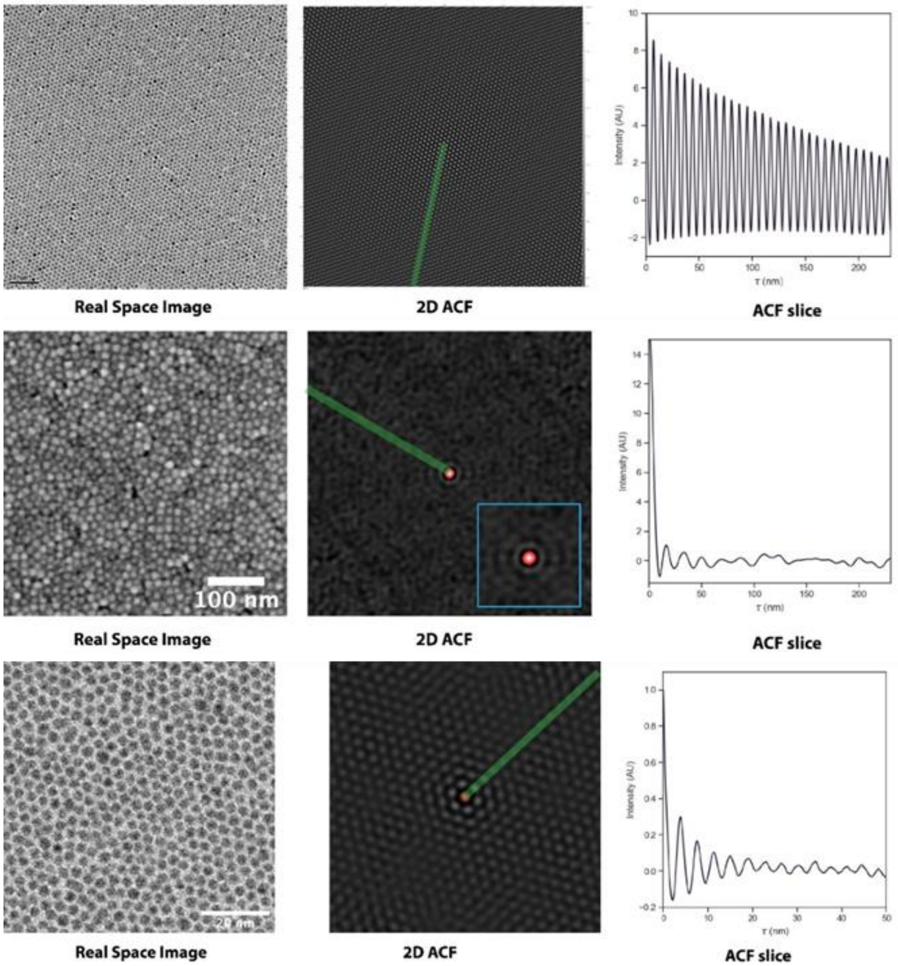

Figure SN4-1. Quantifying the crystalline domain size for NC films using the autocorrelation function (ACF) measured for a TEM micrograph of 9 nm Au NCs, an SEM image of 10 nm HgTe NCs with inorganic ligands (from ref (*48*)) and a TEM micrograph of 6 nm PbS NCs capped with formic acid (from ref (*78*)).

As mentioned above, using the ACF taken from electron microscopy or the physical size of facetted crystallites from optical imaging is a convenient, but imperfect measure of the true degree of crystallinity and phase purity. A more rigorous definition would be to calculate the crystalline component of a solid by determining the fraction of NCs locally coordinated in a close-packed geometry, e.g. as determined by the Steinhard-Nelson order parameters (*69*). While such precise reconstruction is difficult to achieve experimentally (e.g. via real space reconstruction based on 3D tomography), such analysis can routinely be done through simulations where the location of all the NCs is explicitly known (*25*).

Estimating the interparticle conductance

As a general figure of merit for the strength of coupling an artificial solid composed of individual nanocrystals, we use the normalized conductance between two neighboring NCs. Using the Landauer formula, the conductance between two NCs can be expressed as:

$$\sigma = \frac{2e^2}{h}\sum_{i,j} T_{i,j}$$

where $T_{i,j}$ is the transmission of the conductance channel between state i on one particle j on the other and $\frac{2e^2}{h}$ is the conductance quantum, which we denote as σ_0. To simplify the discussion, we use a normalized form of the conductance (σ^*) defined as $\sigma^* = \sigma/\sigma_0$:

The transmission for each channel can in turn be approximated as (*79*):

$$T = e^{-\beta l}$$

where β is the attenuation length of the wavefunction and *l* is the edge to edge separation between two neighboring NCs. In systems where there is only one conductance channel (e.g. as would be expected to be the case for CdSe NCs), the normalized conductance can then be expressed using the simplified formula:

$$\sigma^* = e^{-\beta l}$$

Taking a value of β of 1.1Å^{-1} (see ref (*80*)) one obtains a value of σ^* of 1.80×10^{-10} at an interparticle separation of 2.04 nm, e.g. corresponding to the interparticle separation expected in an FCC film of NPs with a diameter of 5 nm capped with dodecanethiol.

As a last note, in the case of one conduction channel one can relate the previous discussion to the more standard measure of the mobility using the following approximate form (*79*):

$$\mu = \frac{ed^2E_a}{3hk_BT}e^{-\beta l - E_a/k_BT},$$

where E_a is the activation energy assuming that the hopping is an exponentially activated process. The relationship above provides a convenient way of relating the pairwise conductance to the effective mobility in a film.

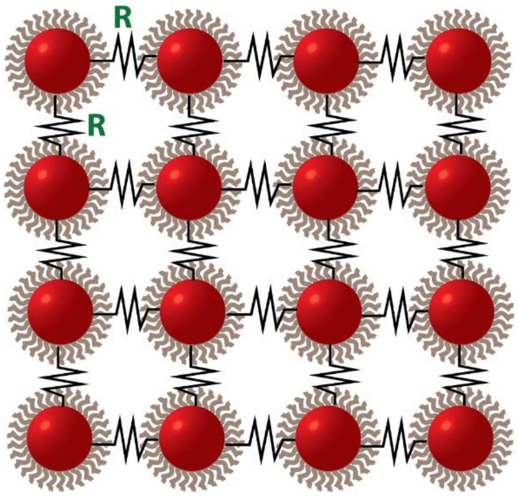

Figure SN4-2. Representation of a NC array as a resistive network with a constant pairwise resistances *R* for nearest neighbor NCs. Distances are not drawn to scale.

Relationship to a resistive network

The conductivity of a film of nanoparticles can also be analyzed by treating the film as a resistive network with a defined resistance between nearest neighbors. Applying such a model to a perfect 3D cubic lattice, one obtains the following resistance for the conductivity (*81*, *82*):

$$\sigma = \frac{1}{Rd},$$

where *R* is the interparticle resistance and *d* is the center-to-center distance between two touching nanoparticles.

3. Supplementary Figures

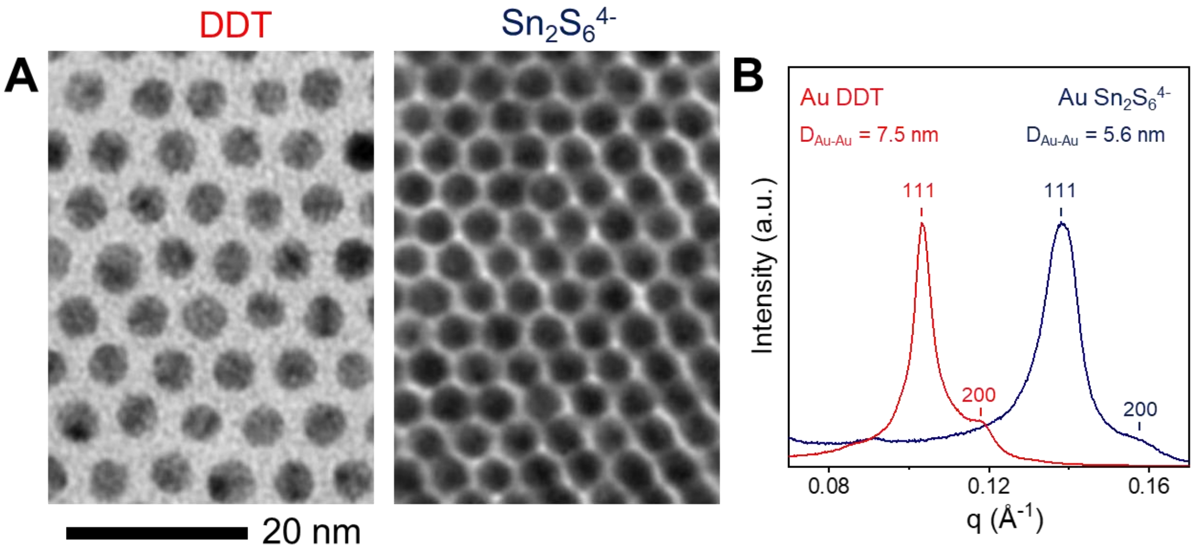

Figure S1. (**a**) Zoomed in TEM images comparing interparticle spacing for self-assembled 5 nm Au NCs capped with n-dodecanethiol (DDT) and $Sn_2S_6^{4-}$ ligands. (**b**) SAXS data on a linear scale comparing the lattice spacing of Au NCs from the same batch assembled using *n*-dodecanethiol organic ligands and $Sn_2S_6^{4-}$ inorganic ligands.

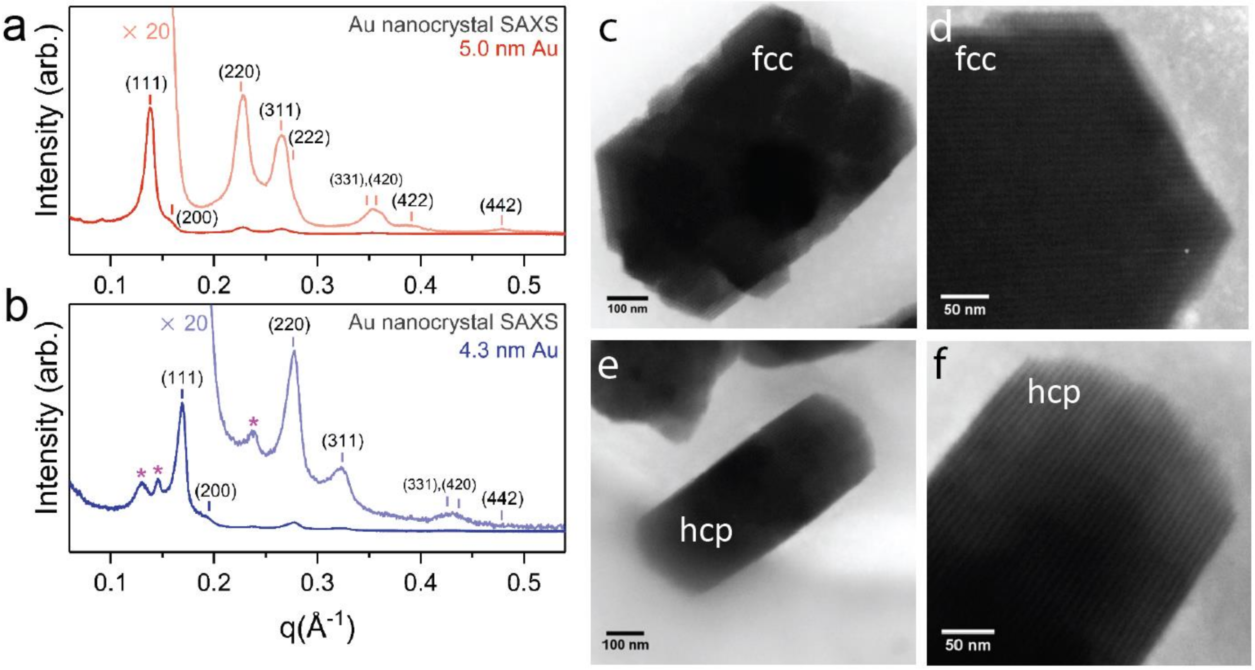

Figure S2. *fcc/hcp* phase coexistence. **(a)** SAXS pattern of a typical Au assembly showing nearly phase-pure *fcc* solid. **(b)** SAXS pattern of a Au assembly with a mixture of *fcc* and *hcp* phases. Additional *hcp* peaks are indicated by an asterisk. **(c-f)** Representative TEM images of *fcc* and *hcp* superlattices.

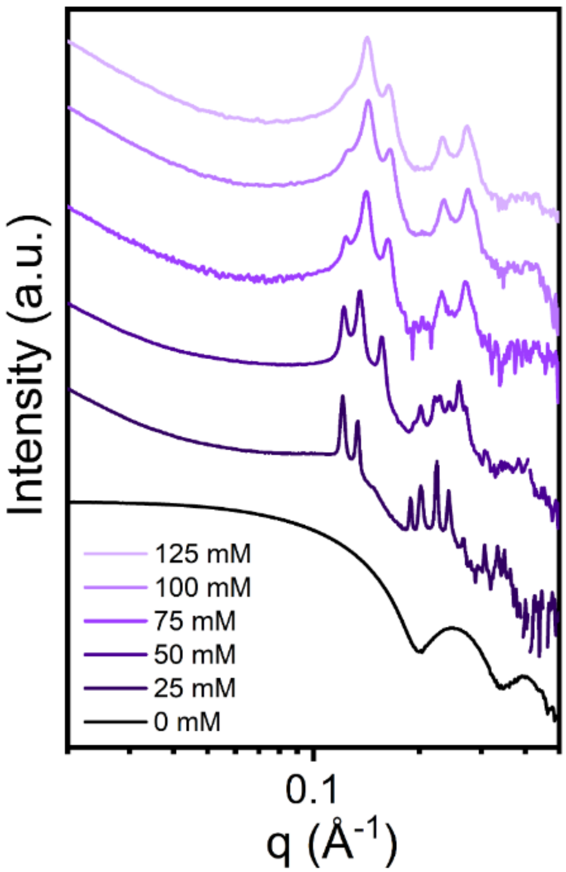

Figure S3. Self-assembly of 4.2 nm Au NCs with $(N_2H_5)_4Sn_2S_6$ ligands in hydrazine. SAXS data are shown at a series of excess ligand concentrations and collected by measuring the solids at the bottom of a glass capillary containing a combination of free colloidal NCs in solution and solid supercrystals. Clear *fcc* structure factors are observed upon complete flocculation of the NC solution (75, 100, 125 mM). At low ligand concentrations (25 mM), partial flocculation often results in complex structure factors resembling topologically close-packed Frank-Kasper phases (*58*). Non-*fcc* phases are likely metastable structures enabled by the additional microreversibility at low quench depths (MCC concentrations).

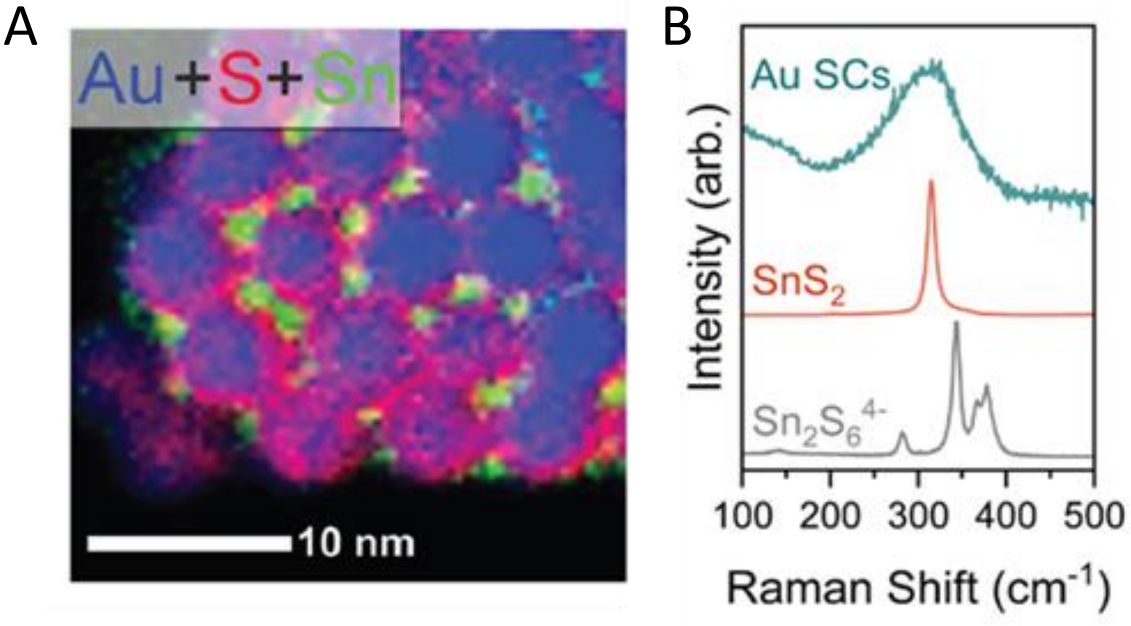

Figure S4. (**A**) Elemental map from the electron energy loss spectroscopy (EELS) data showing the concentration of Sn and S at the interstitial sites of the *fcc* lattice of Au NCs. (**B**) Raman scattering data for Au SCs, crystalline SnS_2, and crystalline $(N_2H_5)_4Sn_2S_6$. The Raman feature centered at 315 cm^{-1} corresponds to the longitudinal optical (LO) phonon frequency of crystalline SnS_2. The significant broadening of the peak is indicative of an amorphous, glassy SnS_2 and $Sn_2S_6^{4-}$ matrix resulting from partial ligand decomposition according to the formula $(N_2H_5)_4Sn_2S_6 \rightarrow 2\ SnS_2 + 2\ (N_2H_5)_2S$. The rise in scattering intensity at lower Raman shift energies is consistent with disorder activated scattering from acoustic modes, also commonly seen in amorphous semiconductors.

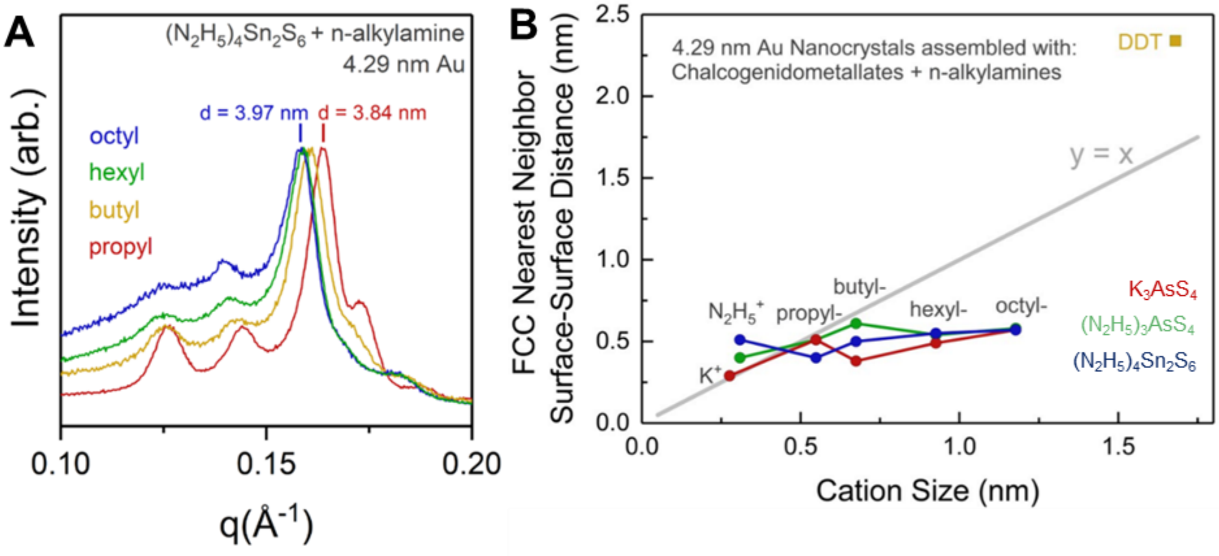

Figure S5. (**A**) Normalized SAXS data taken from assemblies of $(N_2H_5)_4Sn_2S_6$ capped Au NCs flocculated by addition of co-solutions of $(N_2H_5)_4Sn_2S_6$ with 4 equivalents of n-alkylamines of varying chain lengths. All amines used in this experiment were soluble in hydrazine at the necessary 1 M concentration and reacted with hydrazinium cations to form n-alkylammonium thiostannates. Assembly by flocculation with these species resulted in superstructures with lattice constants that only slightly increased with increasing alkyl chain length. The increase in the nearest neighbor surface to surface spacing is less than would be expected if cations were significantly intercalated into the final structures. (**B**) Plot of nearest neighbor spacings for SCs grown by addition of 15 different MCC ligand solutions against the size of the cationic species. K_3AsS_4 serves as a control where no protonation of the additional amine equivalents is possible. As cation size is increased, spacings increase less steeply than the y = x line which denotes the nearest neighbor distance that would be expected if the particles were spaced out by one monolayer of cations. These data suggest that MCC decomposition and rearrangement may be important during SC lattice formation. The rearrangement pathway: $(\text{cation})_4Sn_2S_6 \rightarrow 2\ SnS_2 + 2\ (\text{cation})_2S$ to form glassy SnS_2 in the SC interstices results in expulsion of $(\text{cation})_2S$ from the growing lattice and a weak dependence of lattice dimensions on cation size. As a comparison, the relevant lattice parameter of DDT capped Au superlattices is also included and is plotted against the length of a dodecanethiol molecule as an effective “cation size”. In DDT capped Au superlattices, the DDT ligands are present in significant amounts between neighboring particles and the result is a surface-to-surface distance that is, as expected, larger than the size of a dodecanethiol molecule.

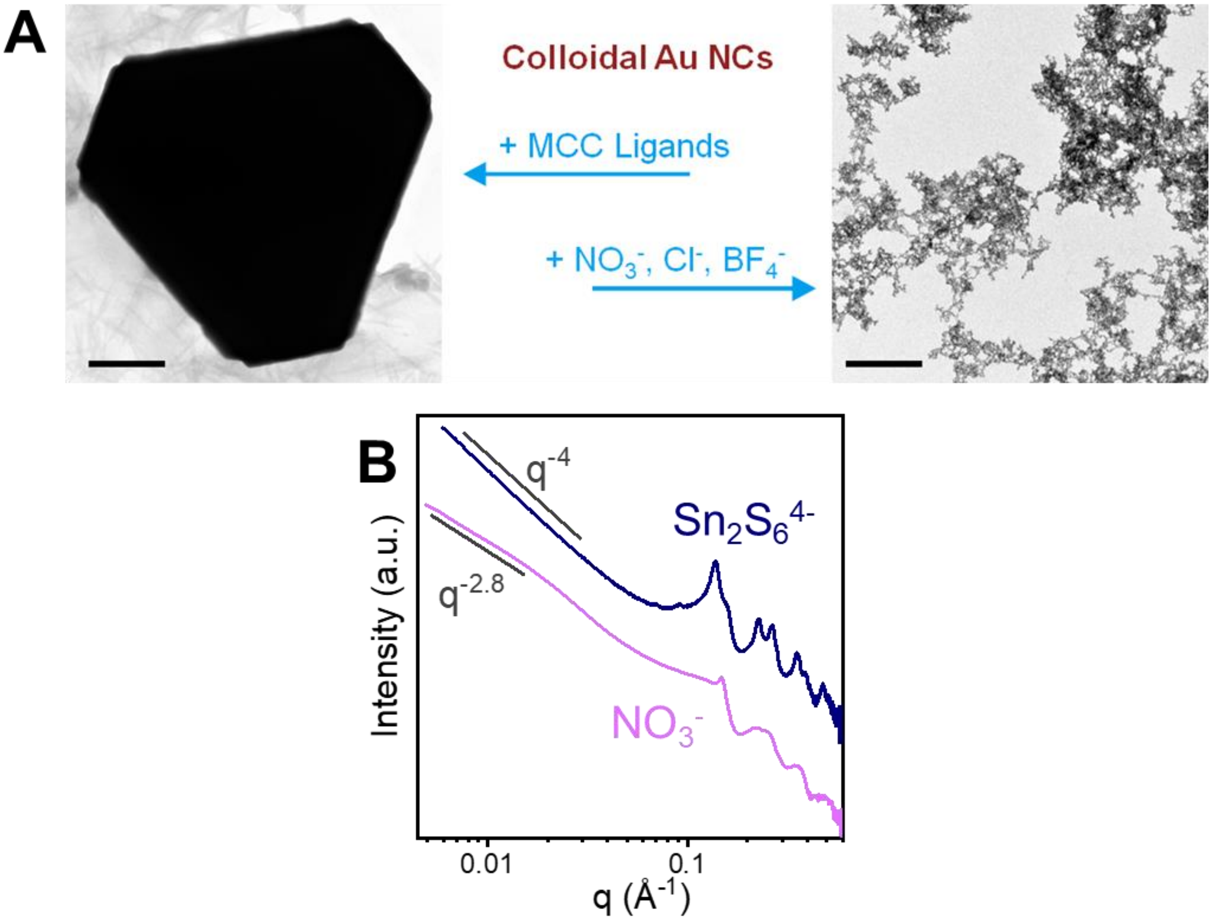

Figure S6. (**A**) TEM images summarizing the result of aggregating colloidal Au with MCC ligands (left) and non-binding 1:1 electrolytes (right). Scale bars are 500 nm. (**B**) Log-log scale SAXS comparing the Porod's Law scaling at low q for Au flocculated with $NaNO_3$ and with $(N_2H_5)_4Sn_2S_6$.

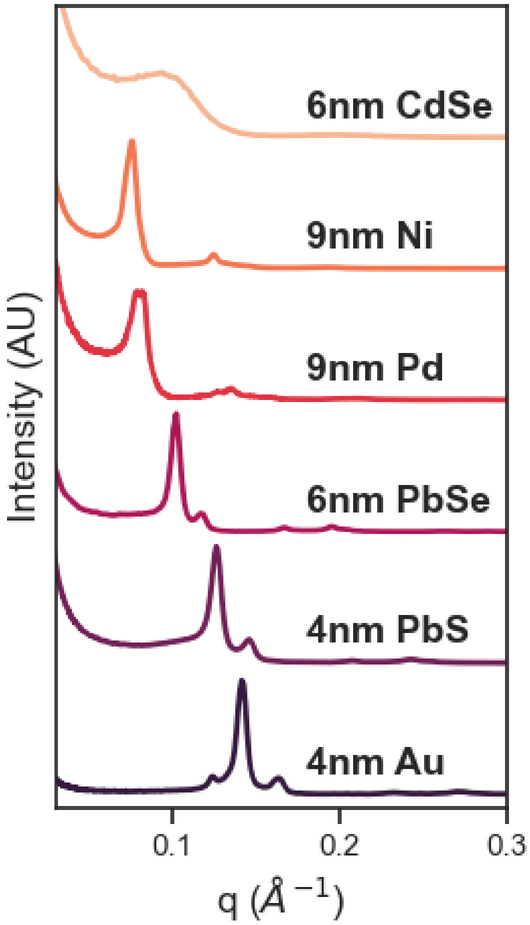

Figure S7. SAXS patterns of NCs of different compositions and sizes flocculated by MCC ligands showing crystalline assembly in all cases except for CdSe, where fractal aggregates were observed.

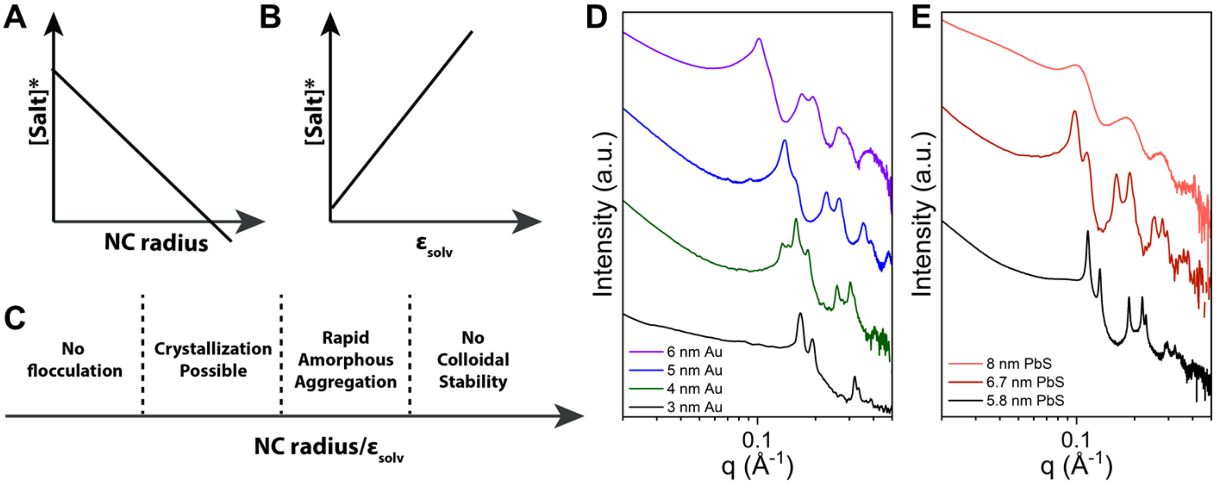

Figure S8. Flocculation regimes of electrostatically stabilized NCs. (**A**,**B**) Schematic dependence of nanocrystal radius and the solvent dielectric constant on the critical salt concentration, [Salt]*, defined as the point at which the sample fully loses colloidal stability and aggregates. (**C**) Regimes of stability and assembly for electrostatically stabilized nanocrystals for a given radius to solvent dielectric constant ratio. (**D**) Size dependent self-assembly of Au-$Sn_2S_6^{4-}$ in hydrazine. Smaller 4 nm NCs required greater amounts of $(N_2H_5)_4Sn_2S_6$ flocculant (~100 mM) than larger 6 nm NCs (~50 mM). Au NCs with a 3 nm diameter could not be fully flocculated with 300 mM $(N_2H_5)_4Sn_2S_6$ but showed partial crystallization with a residual colloidal scattering component. (**E**) Size dependent self-assembly of PbS-$Sn_2S_6^{4-}$ NCs in NMF. All size-dependent data are not presented as ultimate limits for the total ordering of a given size as further optimization is likely possible, but these representative data show a general trend for the influence of NC size on the interparticle interaction potential.

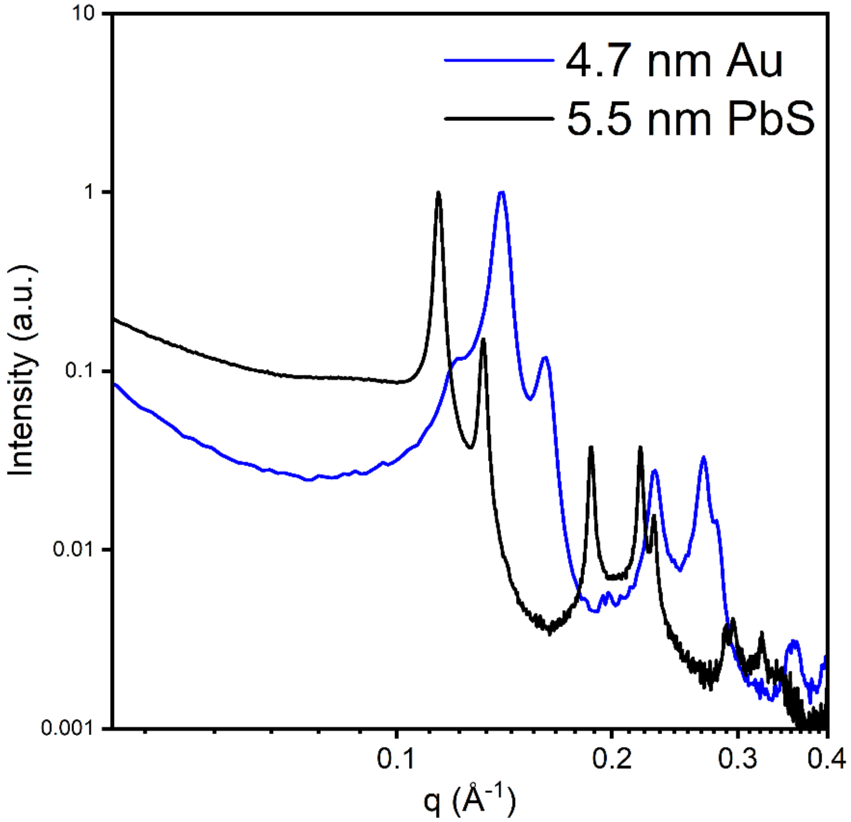

Figure S9. Direct SAXS comparison of Au and PbS NC supercrystals with high degrees of crystallinity. The Au NCs shown here were fully flocculated from hydrazine into a solid powder and measured while suspended in an MCC-hydrazine matrix in a glass capillary. The PbS NCs were partially flocculated with MCC ligand and acetonitrile in N-methylformamide and measured at the bottom of a capillary with an additional fluid component still present in the system due to the nature of the two-step nucleation process.

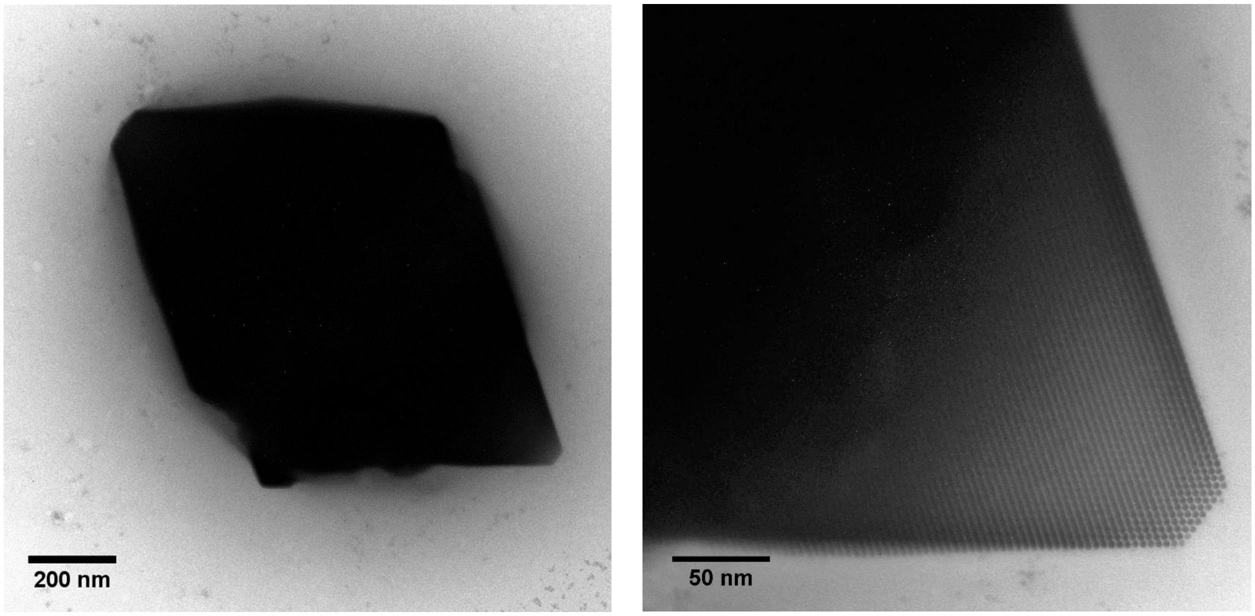

Figure S10. 3.8 nm Au capped with $(N_2H_5)_4Sn_2S_6$ in N_2H_4.

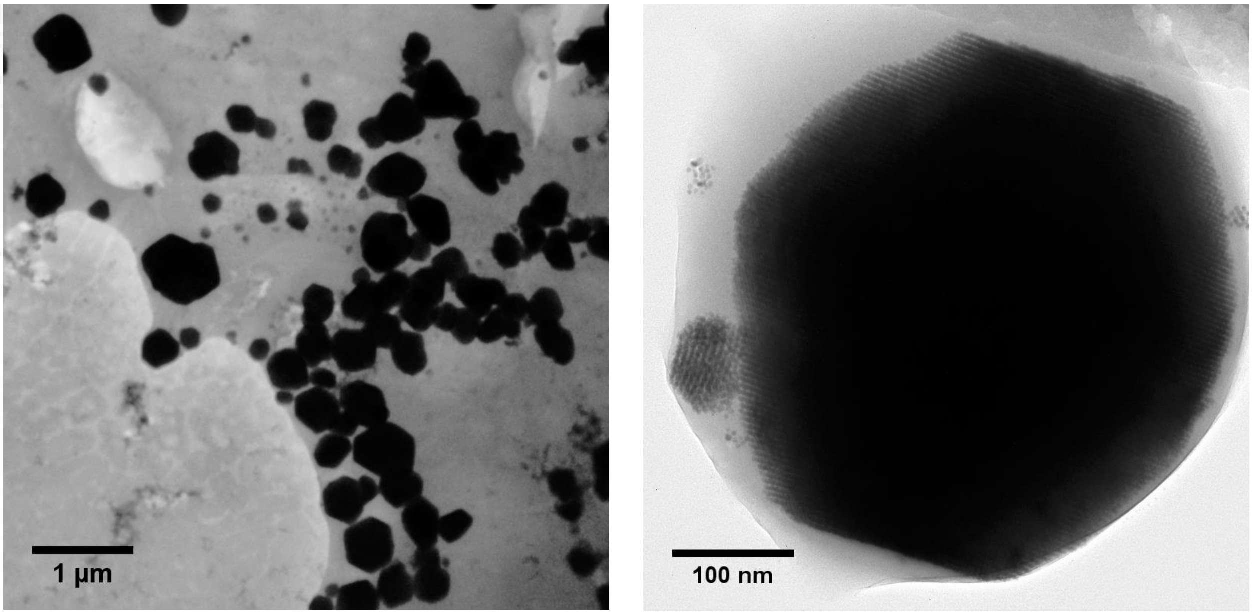

Figure S11. 5 nm Au capped with $(N_2H_5)_4Sn_2S_6$ in N_2H_4.

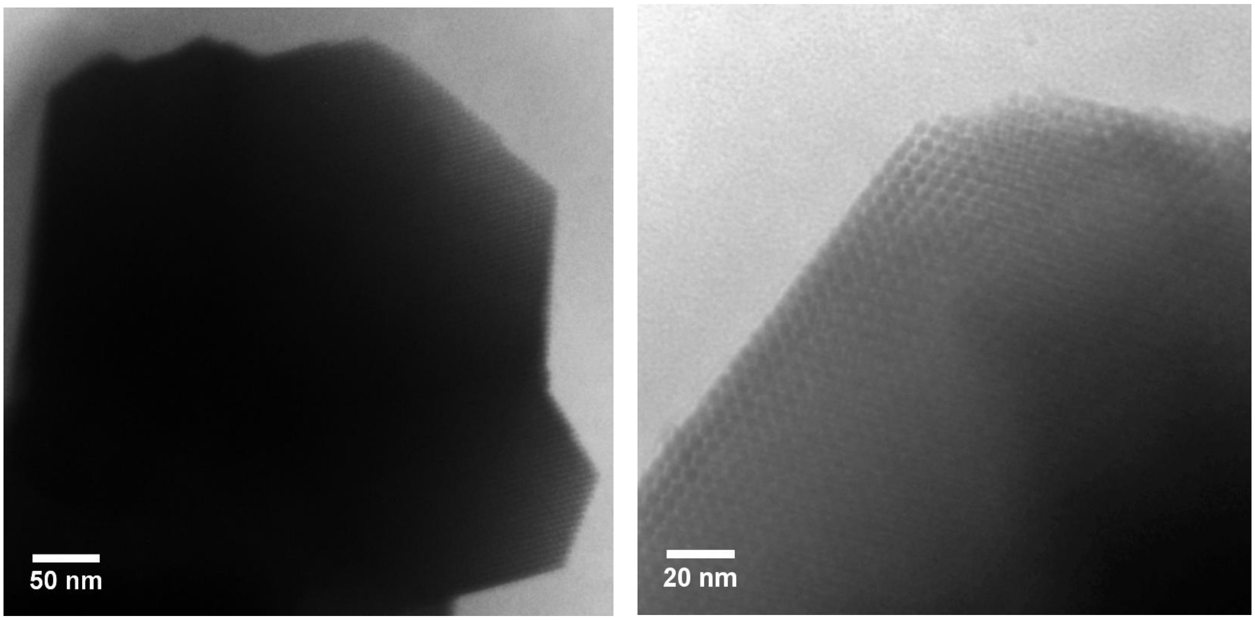

Figure S12. 4 nm Pd capped with $(N_2H_5)_3AsS_4$ in N_2H_4.

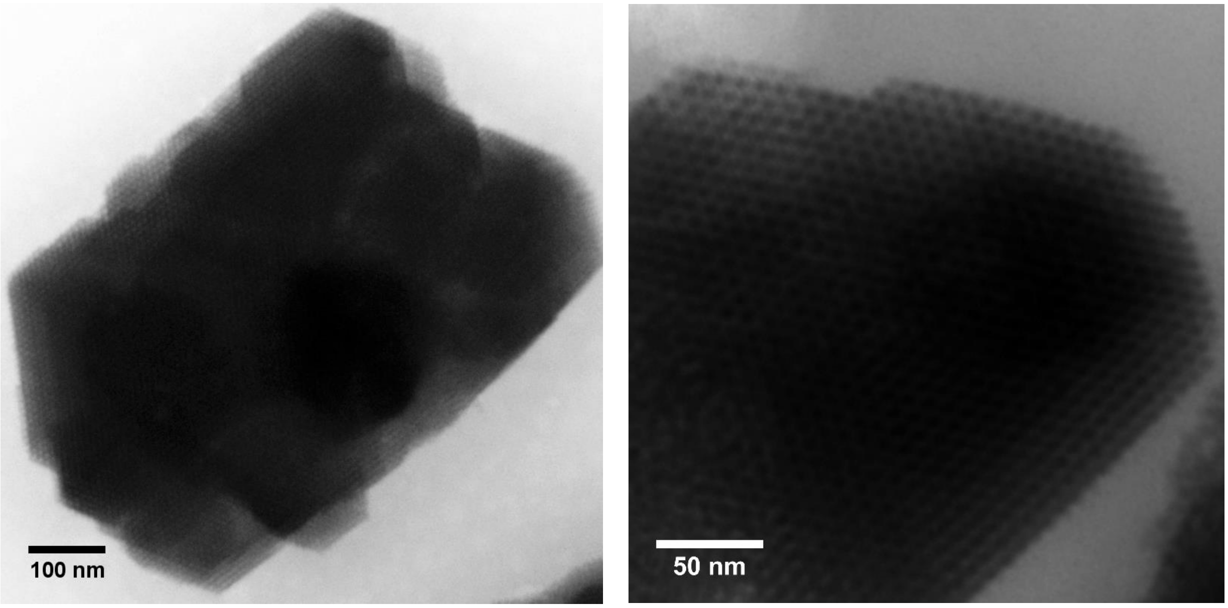

Figure S13. 7.5 nm Pd capped with $(N_2H_5)_4Sn_2S_6$ in N_2H_4.

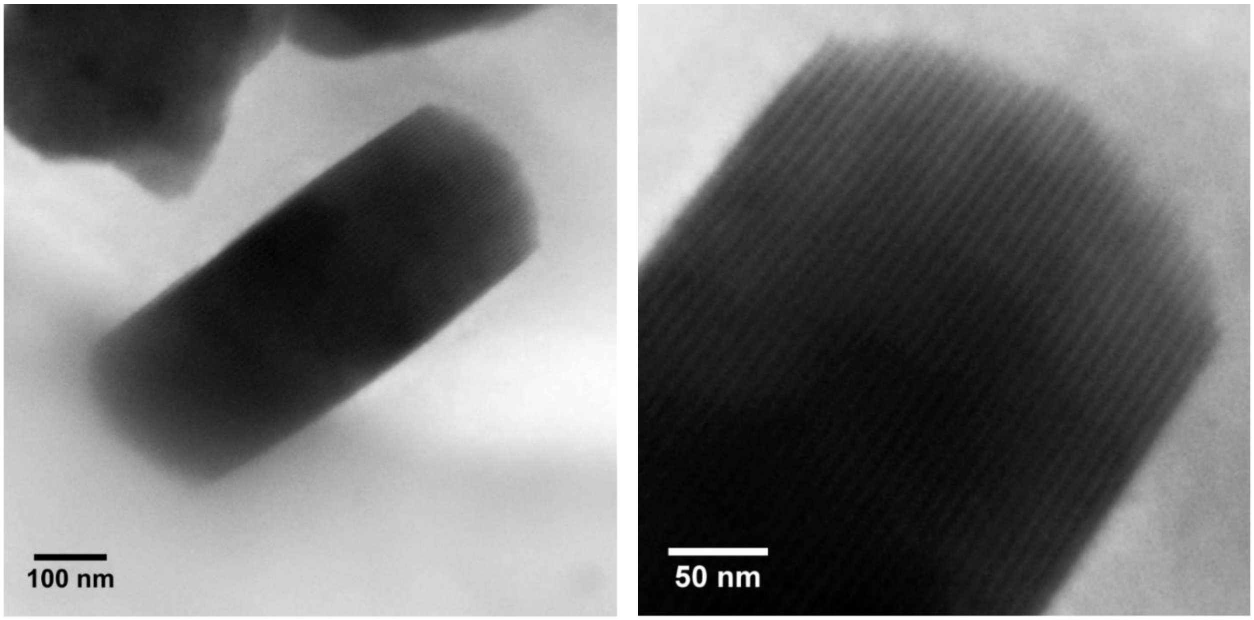

Figure S14. 7.5 nm Pd capped with $(N_2H_5)_4Sn_2S_6$ in N_2H_4.

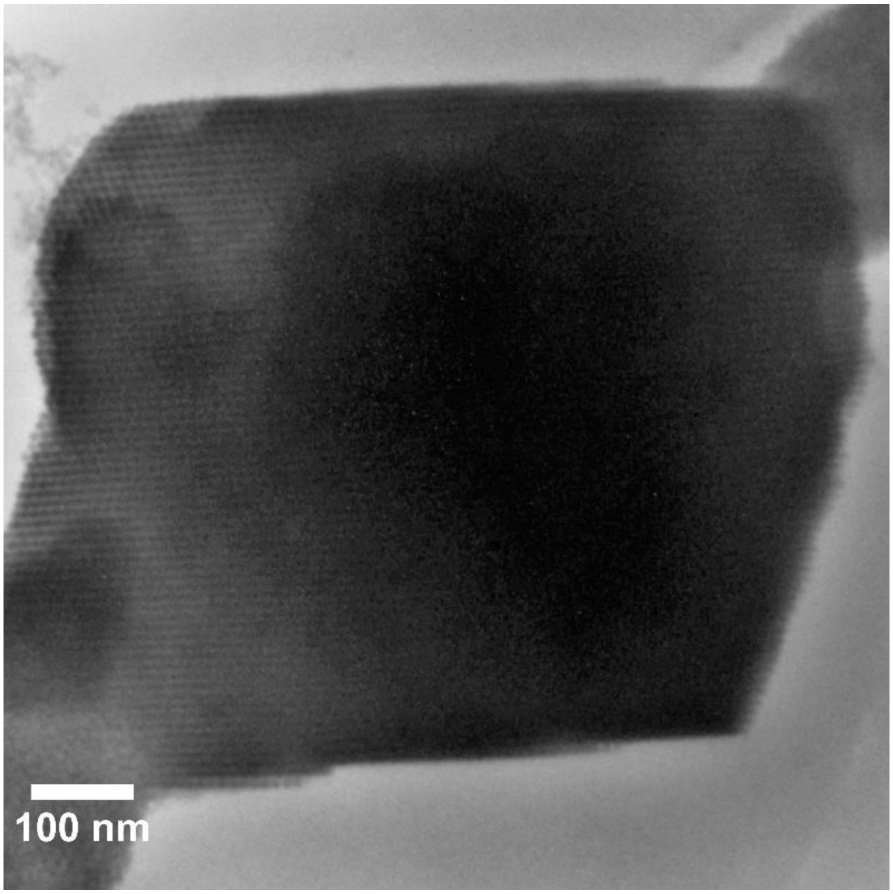

Figure S15. 11 nm Pd capped with $(N_2H_5)_4Sn_2S_6$ in N_2H_4.

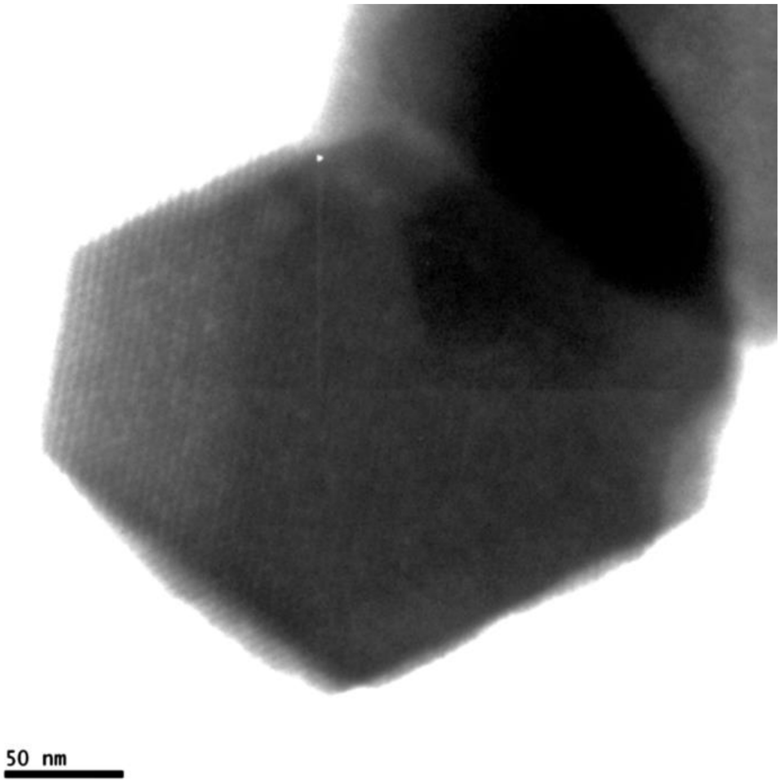

Figure S16. 5 nm Au capped with $(N_2H_5)_3AsS_4$ in N_2H_4.

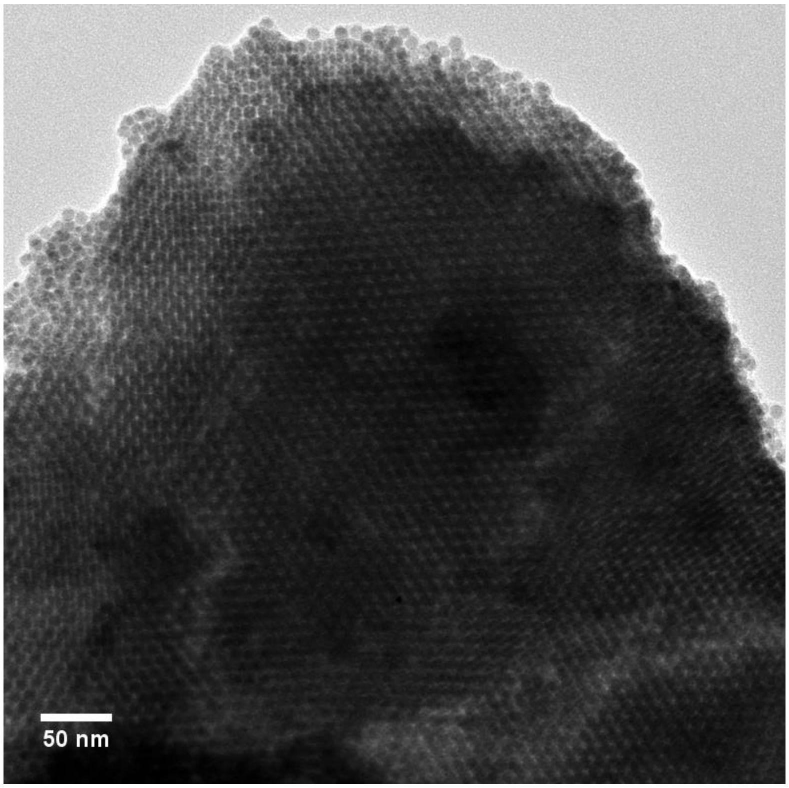

Figure S17. 10 nm Ni capped with K_3AsS_3 in NMF.

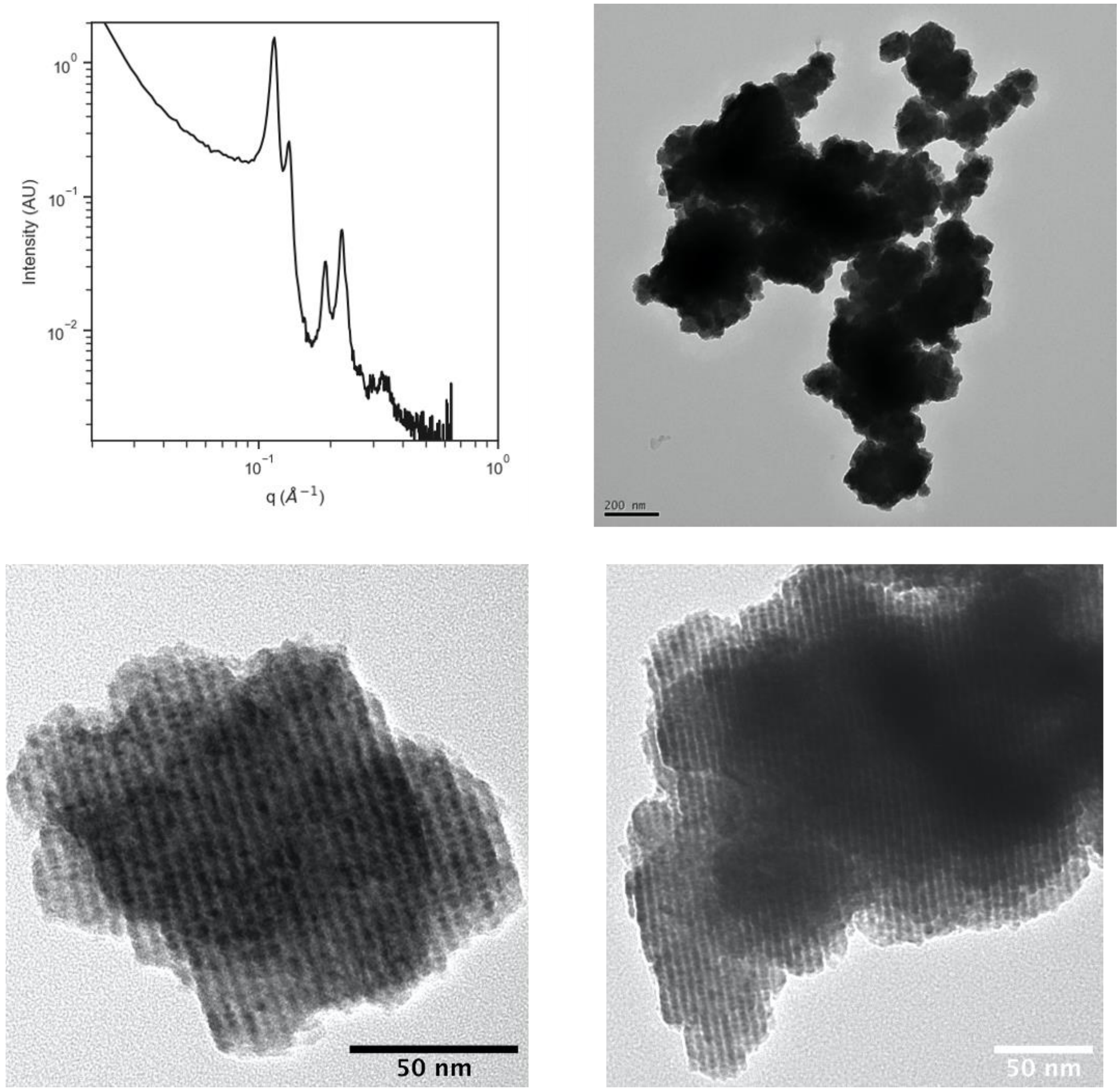

Figure S18. Assembly results for 5 nm PbS NCs flocculated with K_3AsS_4 followed by fast addition of ACN.

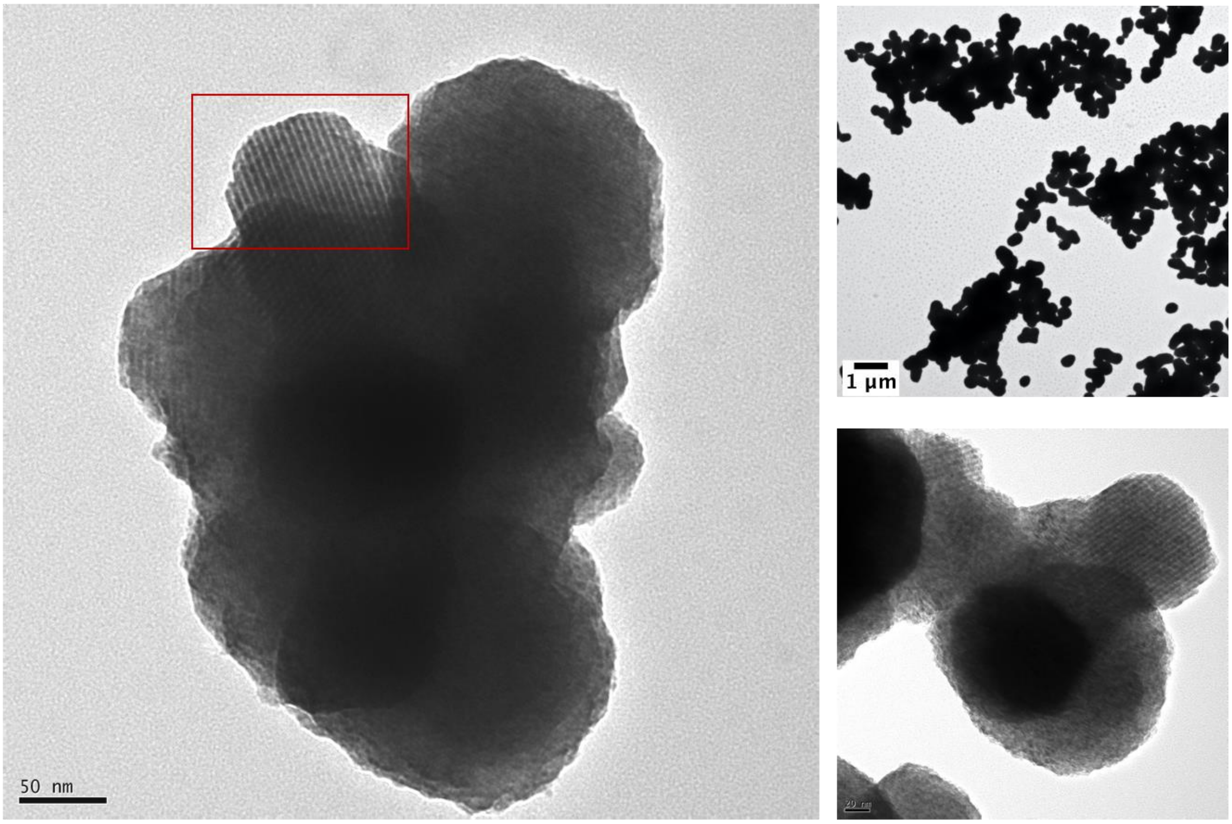

Figure S19. TEM images at various magnifications of assembly results for 4.5 nm PbS NCs flocculated with K_3AsS_4 in NMF followed by slow addition of ACN.

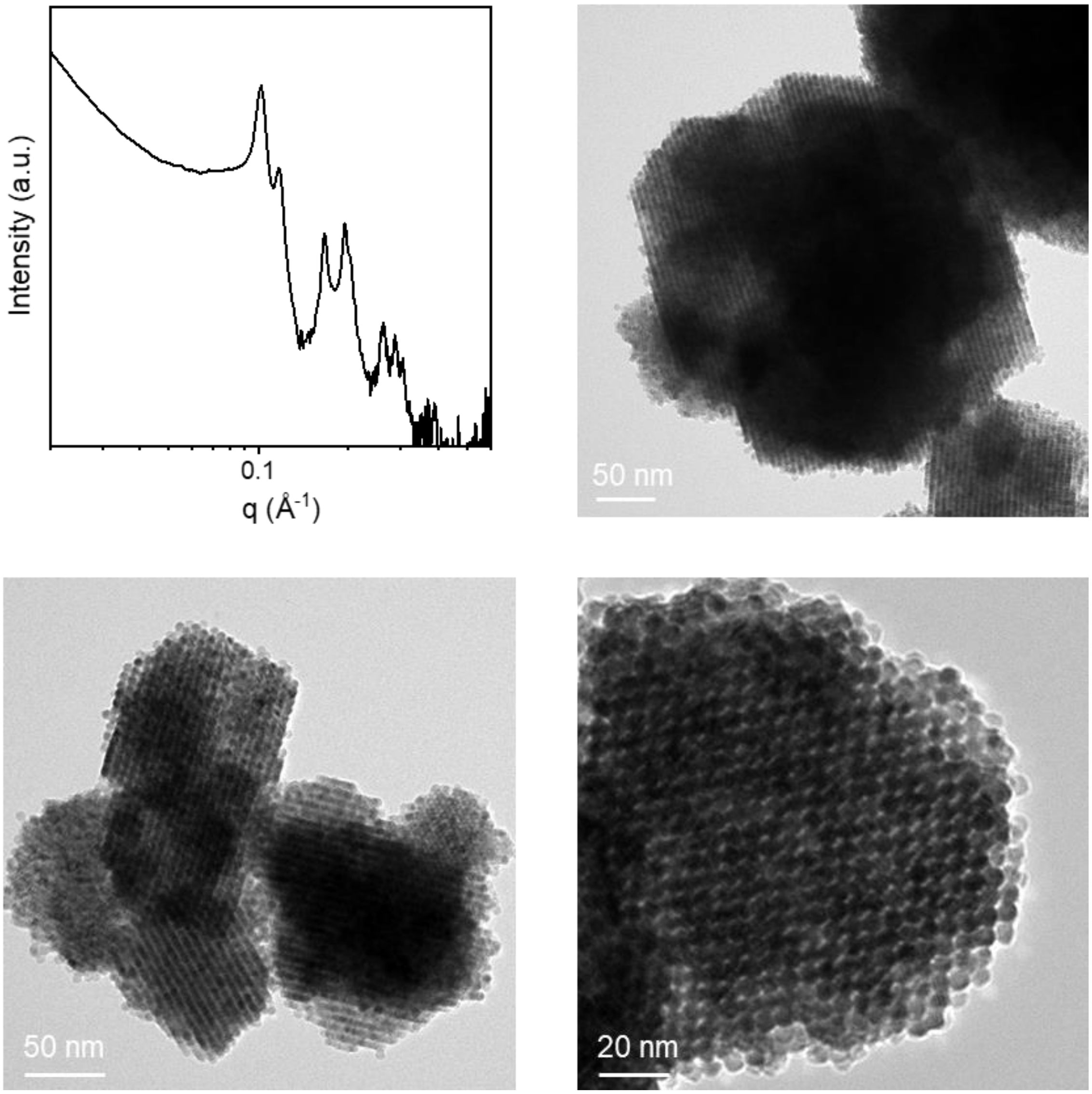

Figure S20. Assembly results for 6 nm PbSe NCs stabilized by $K_4Sn_2S_6$ ligands in N-methylformamide. The colloid was first brought to a ligand concentration of 200 mM K_3AsS_4 followed by addition of acetonitrile to fully flocculate the sample.

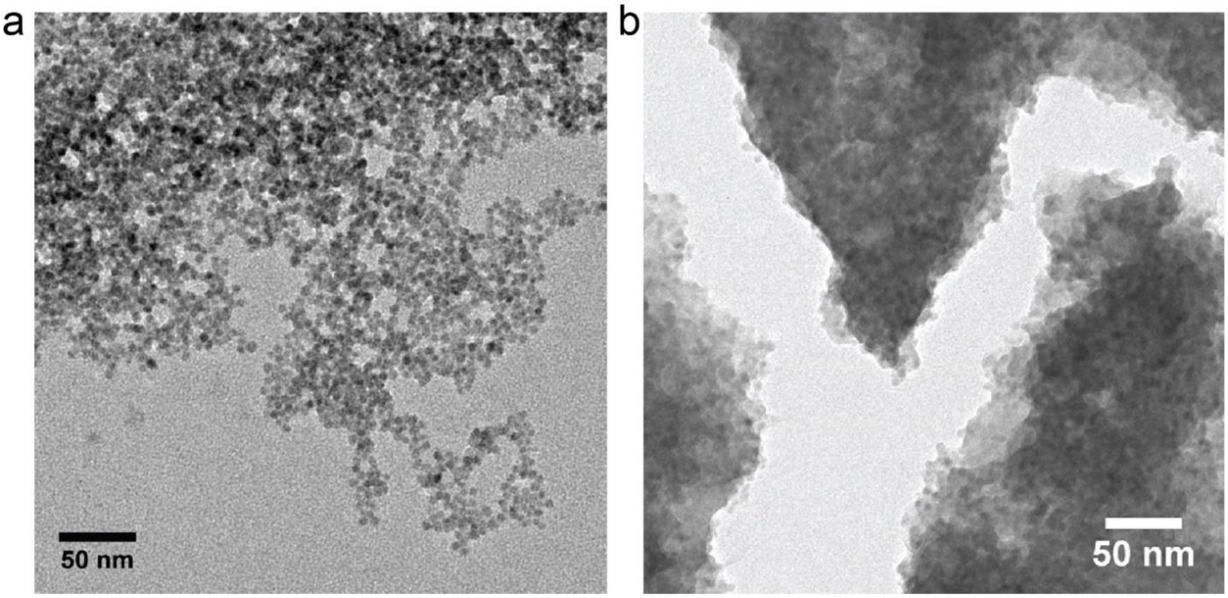

Figure S21. Assembly results for 5 nm CdSe NCs in hydrazine flocculated with **(a)** ACN resulting in a low-density fractal aggregate and **(b)** additional $(N_2H_5)_4Sn_2S_6$ and ACN resulting in compact aggregates with no long-range order.

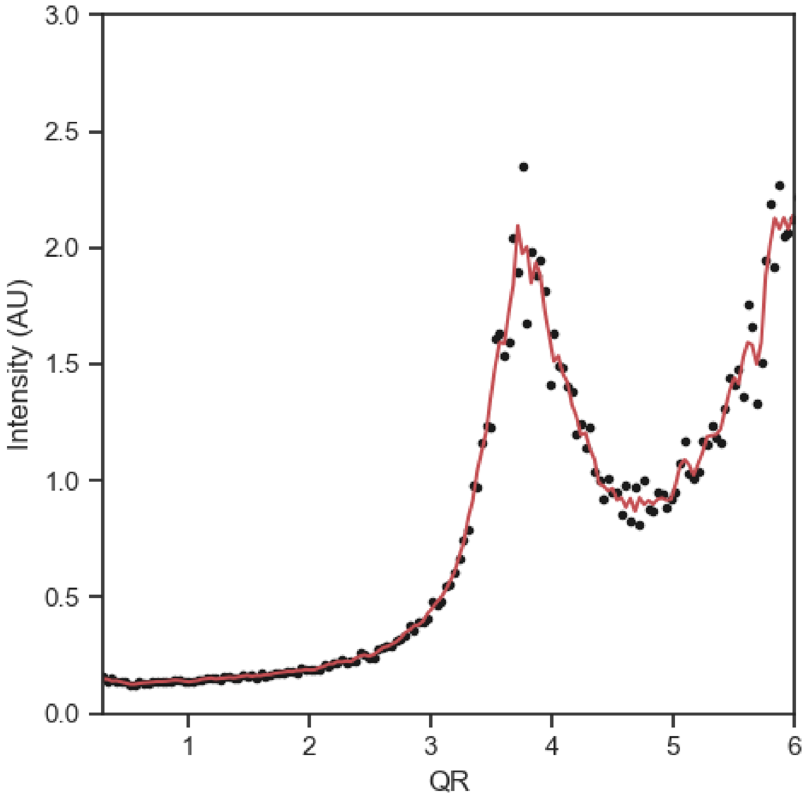

Figure S22. Extracted structure factor for a typical "dense fluid" shown in Fig. 3A for PbS NCs with an average diameter of 5.5 nm. Black points represent the raw data, and the red trace is a 3-point running boxcar average.

A XRF Analysis

Sample in Hydrazine	MCC grafting density (nm^{-2})
5 nm zb-CdSe-$Sn_2S_6^{4-}$	0.23
5 nm Au-$Sn_2S_6^{4-}$	2.0
4.3 nm Au-$Sn_2S_6^{4-}$	2.0

B ICP-OES Analysis

Sample in Hydrazine	MCC grafting density (nm^{-2})
5 nm zb-CdSe-$Sn_2S_6^{4-}$	0.18
5 nm Au-$Sn_2S_6^{4-}$	1.6

C ICP-OES Analysis

Sample in NMF	MCC grafting density (nm^{-2})
4.4 nm PbS-$Sn_2S_6^{4-}$	1.3
4.5 nm zb-CdSe-$Sn_2S_6^{4-}$	0.84

Sample in NMF	MCC grafting density (nm^{-2})
5.7 nm PbS-$Sn_2S_6^{4-}$	1.2
5.5 nm zb-CdSe-$Sn_2S_6^{4-}$	0.94
5.8 nm zb-CdSe-$Sn_2S_6^{4-}$	0.83

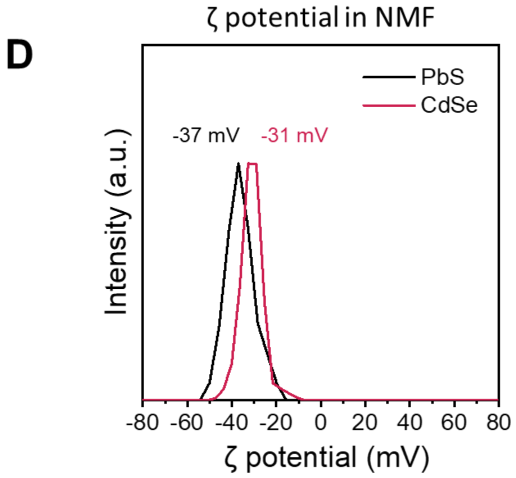

Figure S23. (**A**) Elemental analysis by X-ray fluorescence (XRF) for selected inorganic NCs stabilized in hydrazine by $(N_2H_5)_4Sn_2S_6$ ligands. All grafting densities were calculated based on the metal (NC) to metal (ligand) ratios (e.g., Au:Sn) assuming spherical NCs with a given diameter and a density equal to that of the bulk material. Metallic particles consistently have much more associated MCC for a given amount of NC core material. The samples are prepared from NC colloids that have been washed with acetonitrile to remove excess MCC that is not associated with the particle surfaces. These values are presented as an effective "grafting density," but they do not distinguish between MCC species that are directly chemically bonded to an NC surface or can be held near a NC surface by electrostatics. (**B**) Elemental analysis by ICP-OES of CdSe and Au NC samples stabilized $(N_2H_5)_4Sn_2S_6$ in hydrazine. The effective grafting densities agree well with those obtained via XRF. (**C**) Elemental analysis by ICP-OES of PbS and CdSe NC samples stabilized by $K_4Sn_2S_6$ in N-methylformamide. PbS NCs have an ~40% higher grafting density than similar CdSe NCs. The large difference in CdSe MCC grafting density between hydrazine and NMF may be related to a difference in solvent-NC or solvent-MCC interactions which could affect the equilibrium ligand grafting density. (**D**) ζ-potential measurements of 5.7 nm PbS and 5.5 nm CdSe with identical $K_4Sn_2S_6$ in N-methylformamide. PbS NCs exhibit a slightly higher negative zeta potential (and therefore surface charge) in agreement with elemental analysis showing increased anion condensation. This result is consistent with our model of high ε_{NC} enabling self-assembly due to increased ligand coverage.

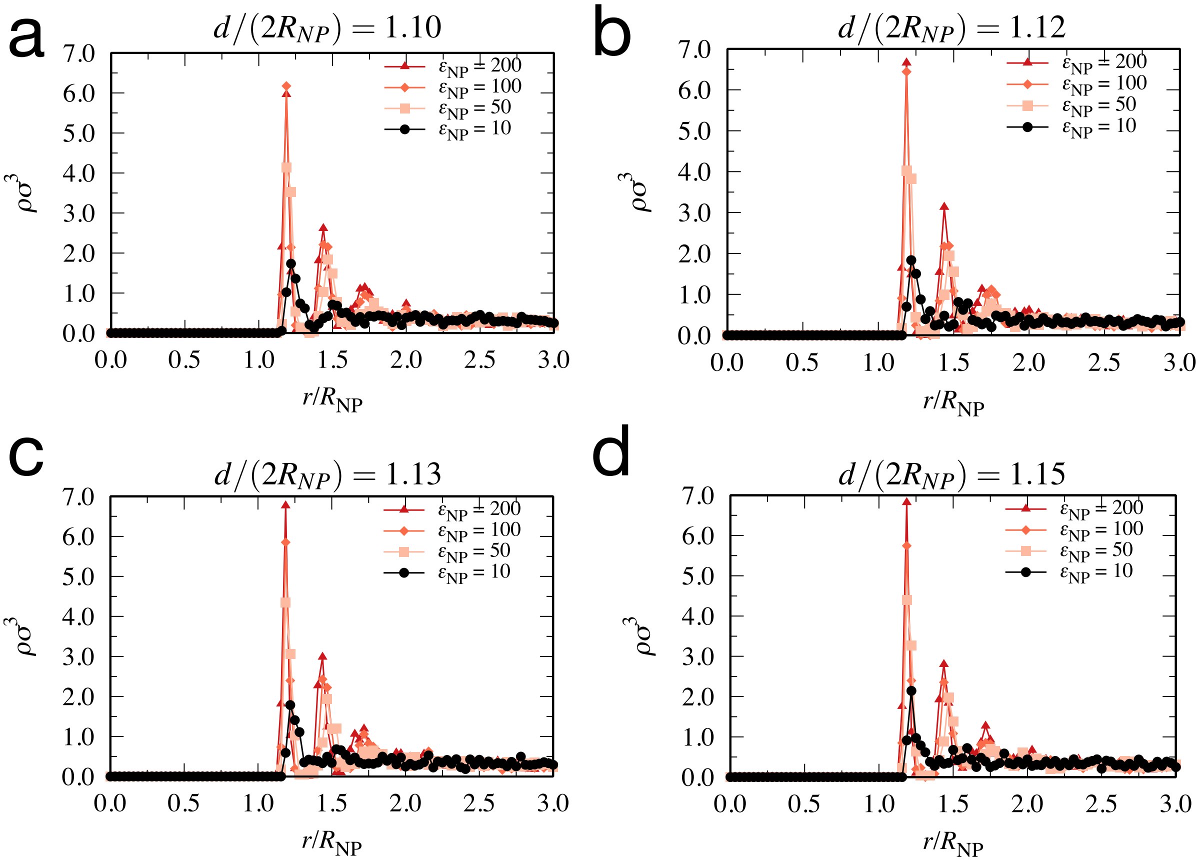

Figure S24. Radial density profiles of the anions surrounding a nanoparticle (NP) for different NP dielectric constants at varying NP center-center distances ($d/2R_{NP}$).

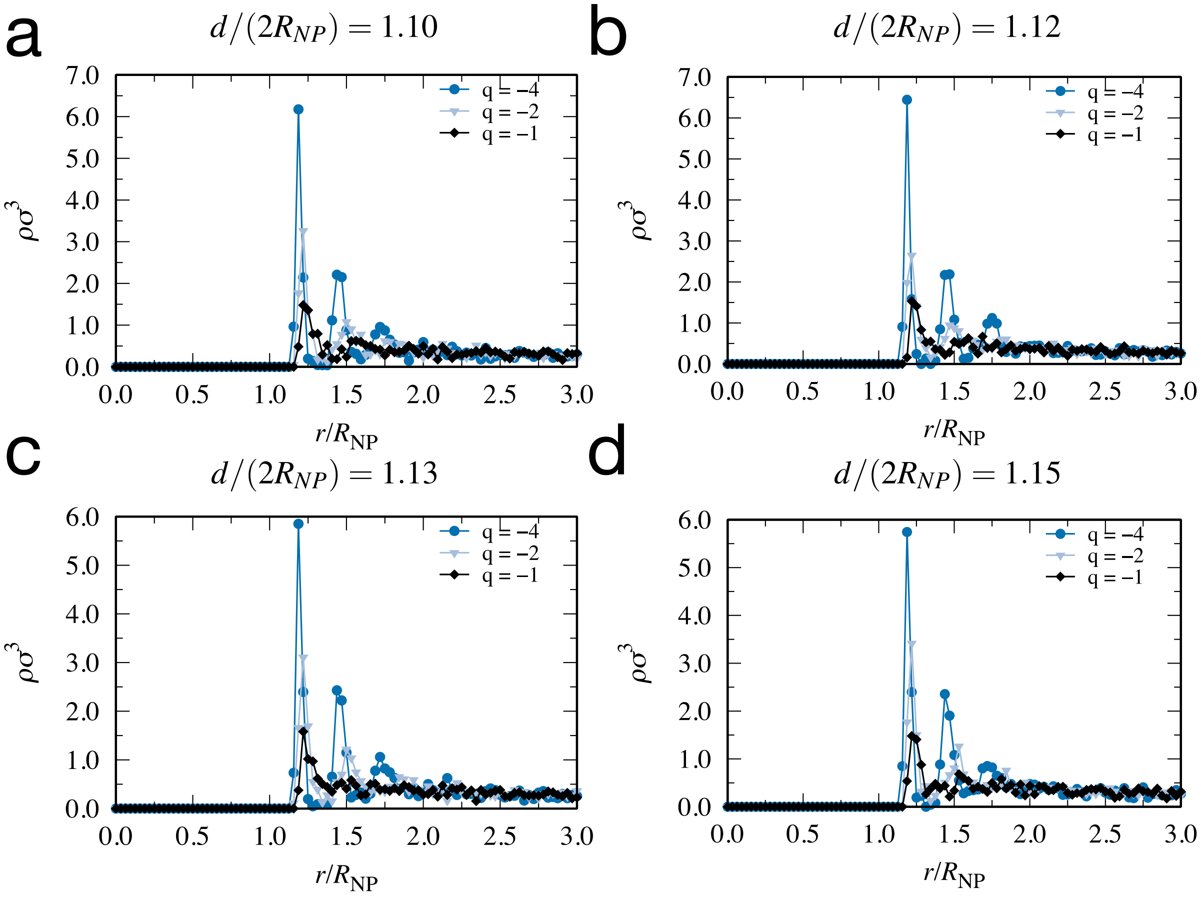

Figure S25. Radial density profiles of the anions surrounding nanoparticles for different anion valences, q, at varying NC center-center distances, d/2R_{NP}.

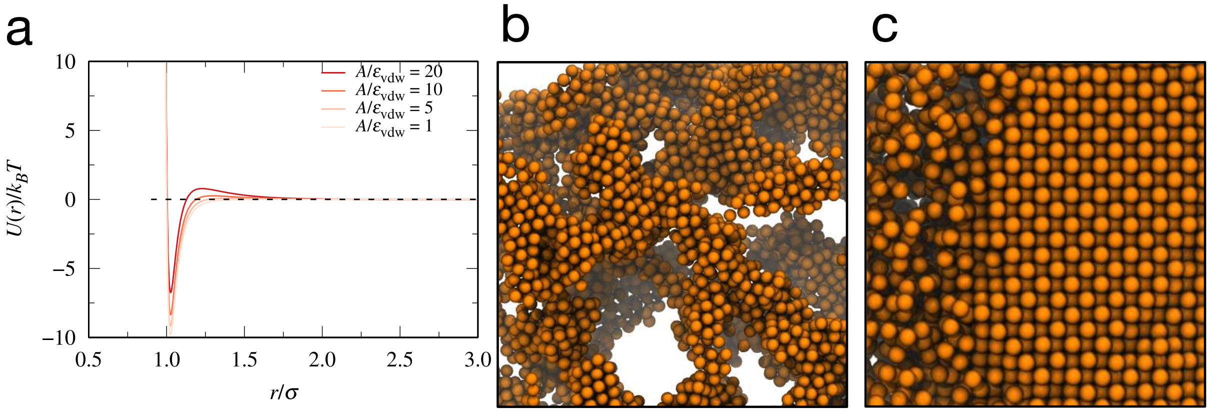

Figure S26. (a) Coarse-grained (CG) interaction energy between two ligand coated NCs with implicit condensed multivalent ions. **(b)** Representative snapshot of a gel structure formed with $A/\varepsilon_{\mathrm{vdw}} = 1$. **(c)** Representative simulation snapshots of the coexistence between a metastable high-density liquid phase and a face-centered cubic (*fcc*) crystalline phase close to the melting temperature. See Supplementary Note 2 for additional details.

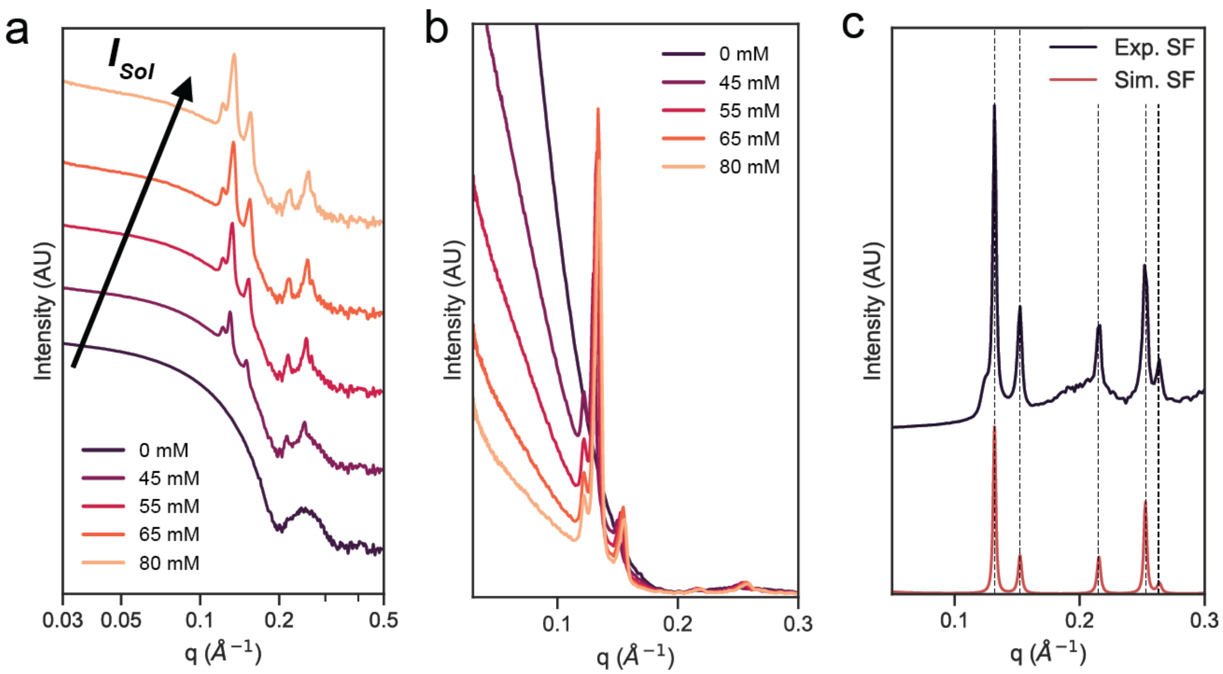

Figure S27. (a) Offset log-log SAXS patterns of 4.2 nm Au NCs at increasing concentrations of $(N_2H_5)_4Sn_2S_6$. **(b)** The data from panel **a** shown on a linear scale (not offset), showing the decrease of colloidal background as the crystalline peaks grow, indicating incorporation of free colloidal particles into a crystalline solid. **(c)** Comparison of experimental and simulated *fcc* structure factor for the same particles at a ligand concentration of 50 mM.

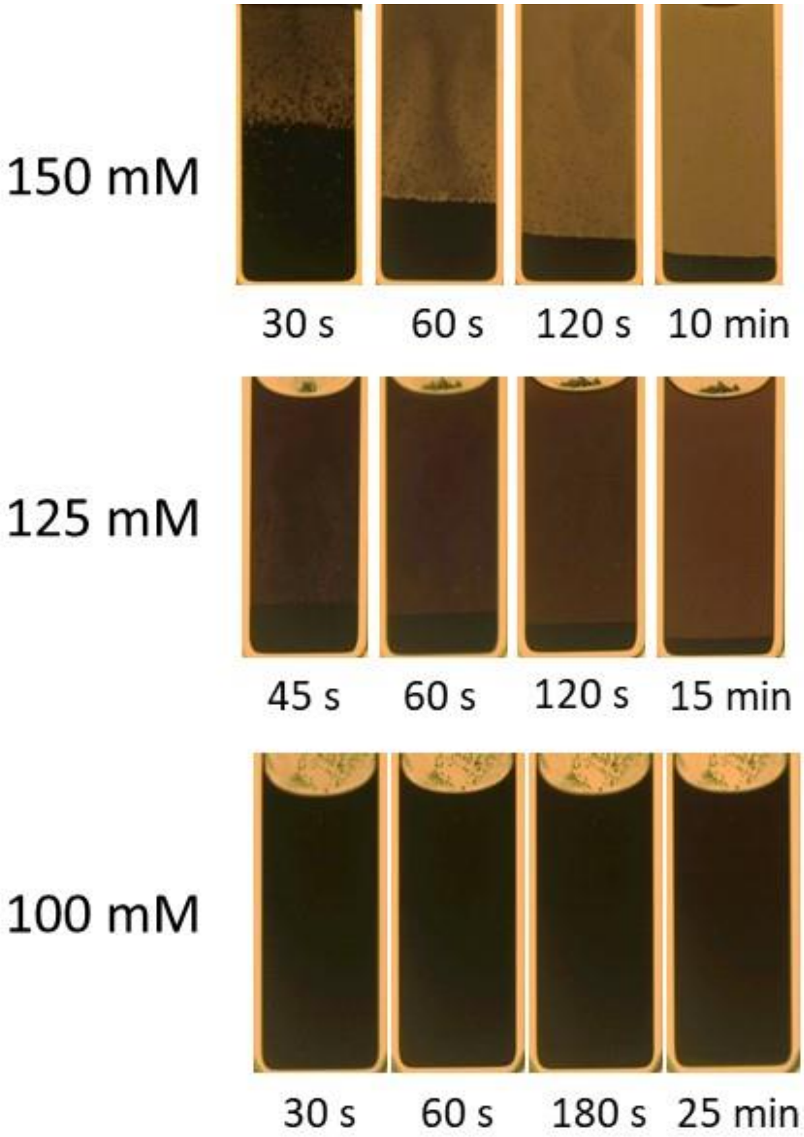

Figure S28. Photographs of 4.4 nm Au NCs with $Sn_2S_6^{4-}$ surface ligands in hydrazine taken immediately after the addition of $Sn_2S_6^{4-}$ ligands to final concentrations of 150, 125, and 100 mM. Samples are suspended in 1 mm path length glass cuvettes and photos taken inside of a nitrogen-filled glovebox.

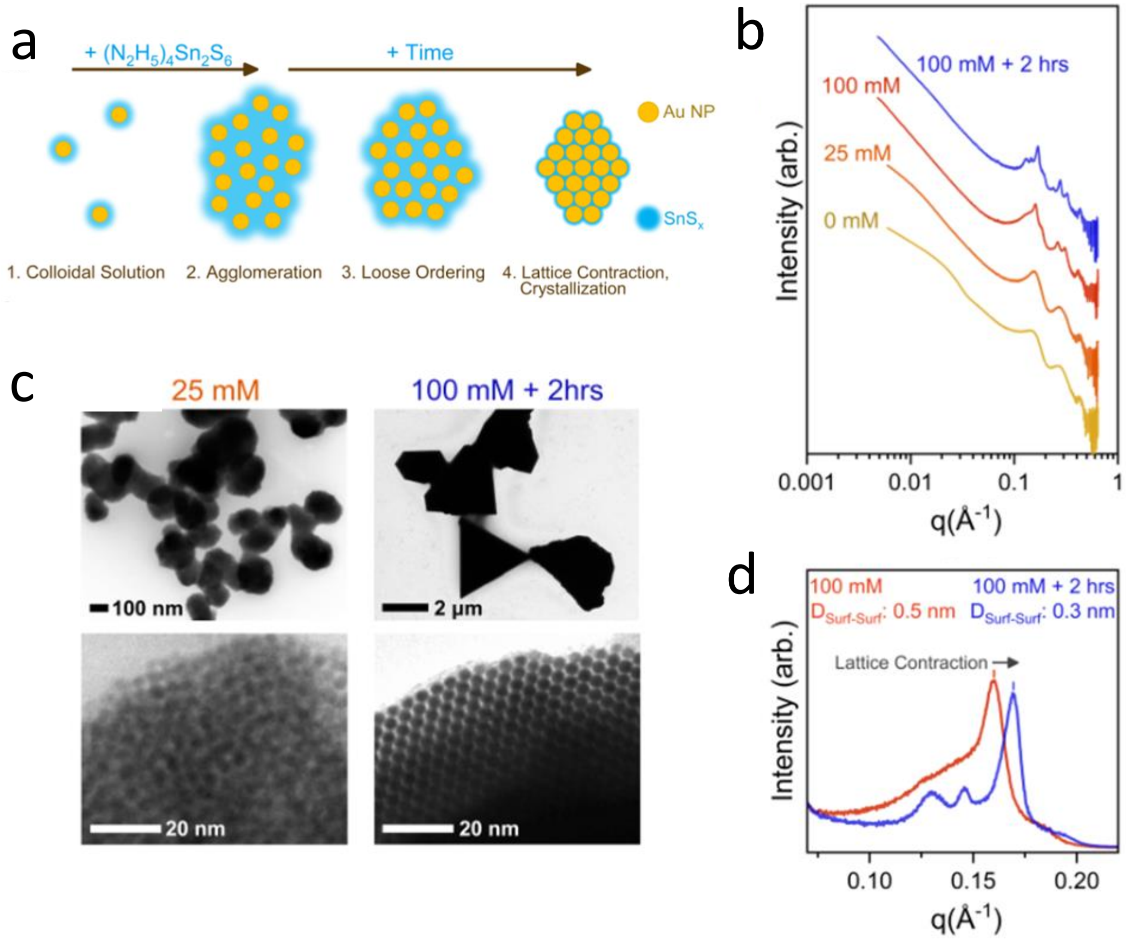

Figure S29. Assembly mechanism of 4.6 nm Au-$Sn_2S_6^{4-}$ nanocrystals. **(a)** Schematic diagram depicting the two-step assembly process. **(b)** SAXS data on a log-log scale showing the progression of structuring with increasing $Sn_2S_6^{4-}$ concentration. **(c)** TEM images showing the material recovered from drying Au colloids with 25 mM $Sn_2S_6^{4-}$ and 100 mM $Sn_2S_6^{4-}$ ligand concentrations. **(d)** Linear scale SAXS plots emphasizing the lattice contraction and ordering that occurs after the separation of colloidal solution into two phases.

An addition of 100 mM $(N_2H_5)_4Sn_2S_6$ ligand solution induces colloidal 4.6 nm Au NCs to agglomerate. These agglomerations gradually densify into the final SC structure (figure S29a). Structural changes occurring during the assembly process can be monitored by SAXS. A series of assembly experiments were set up such that four identical starting colloids of Au in N_2H_4 in four separate vials each had the concentration of $(N_2H_5)_4Sn_2S_6$ incrementally increased taking the samples through four stages: **1.** 0 mM, **2.** 25 mM, **3.** 100 mM, and **4.** 100 mM + 2 hours wait time. In the course of this procedure, the assembly process was arrested by addition of MeCN to precipitate the colloid at the end of a different stage for each of the four samples. The samples were collected and deposited on polyimide film for SAXS measurements (figure S29b). The yellow and orange traces show results for the two samples where MeCN was added at stage 1, and 2 respectively. These samples were still colloidal at the time of MeCN precipitation as the $(N_2H_5)_4Sn_2S_6$ concentration was insufficient to destabilize the colloid. The result in both cases was formation of amorphous NC aggregates, as confirmed by both SAXS (figure S29b) and TEM (figure S29c). These first two traces serve as a control experiment to verify that precipitation by a small amount of acetonitrile immobilizes the particles and prevents further reorganization. In contrast, the samples precipitated after stage 3 and stage 4, shown in red and blue in Figure S29b, do show formation of ordered phases. For these samples, agglomeration occurs due to the 100 mM $(N_2H_5)_4Sn_2S_6$ concentration, and the colloids are already destabilized by the time MeCN is added at the end of stages 3 and 4. The effective difference between these two samples is in the length of the wait time between raising the $(N_2H_5)_4Sn_2S_6$ concentration to 100 mM and the addition of MeCN to freeze the particles in place. Both samples show evidence of NC ordering by the SAXS measurements in Figure S29b, with sharper and more defined peaks indicating a higher degree of order in the sample precipitated after waiting 2 hours. TEM images from a sample of Au colloid flocculated in 100 mM thiostannate solution and aged for 2 hours reveal faceted supercrystals with 1 – 5 µm edge lengths (figure S29c). Images taken at higher magnification clearly show the internal lattice symmetry of these large structures.

A more surprising and counterintuitive difference between the internal structure of these two samples is highlighted in Figure S29d. During the 2 hour wait time, the agglomerated structures induced by $(N_2H_5)_4Sn_2S_6$ addition not only rearrange to a higher degree of order, they also contract. The *fcc* lattice constant shrinks such that the calculated surface to surface distance between neighboring particles in the lattice decreases from 0.5 nm to 0.3 nm. Apparently, supercrystals form by particles first loosely ordering at a larger spacing followed by a contraction and densification that produces the final faceted energy minimized structures. These observations suggest that despite apparent agglomeration, Au NCs can efficiently rearrange and that long-range ordered structures form from the dense phase formed immediately after addition of 100 mM $(N_2H_5)_4Sn_2S_6$. The dense phase undergoes time evolution characteristic of fluid-like behavior rather than arrested properties of a colloidal glass.

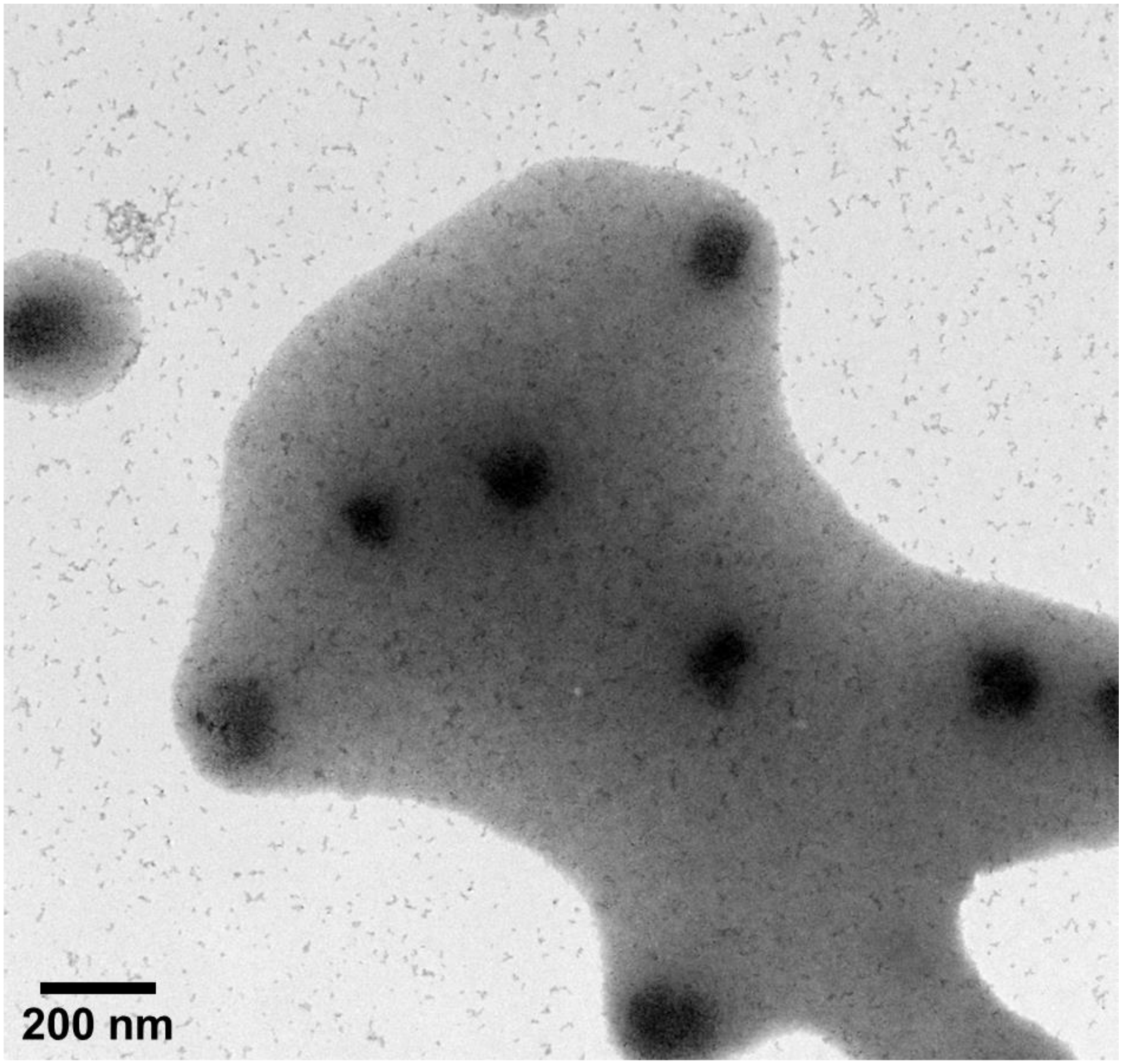

Figure S30. TEM image of 5 nm Au assembled from N_2H_4 by addition of $(N_2H_5)_4Sn_2S_6$. The dark gray structure is composed of dense, randomly packed Au nanocrystals. Within this amorphous structure, small regions of supercrystalline phases have nucleated and are visible as dark spots roughly 100 nm across.

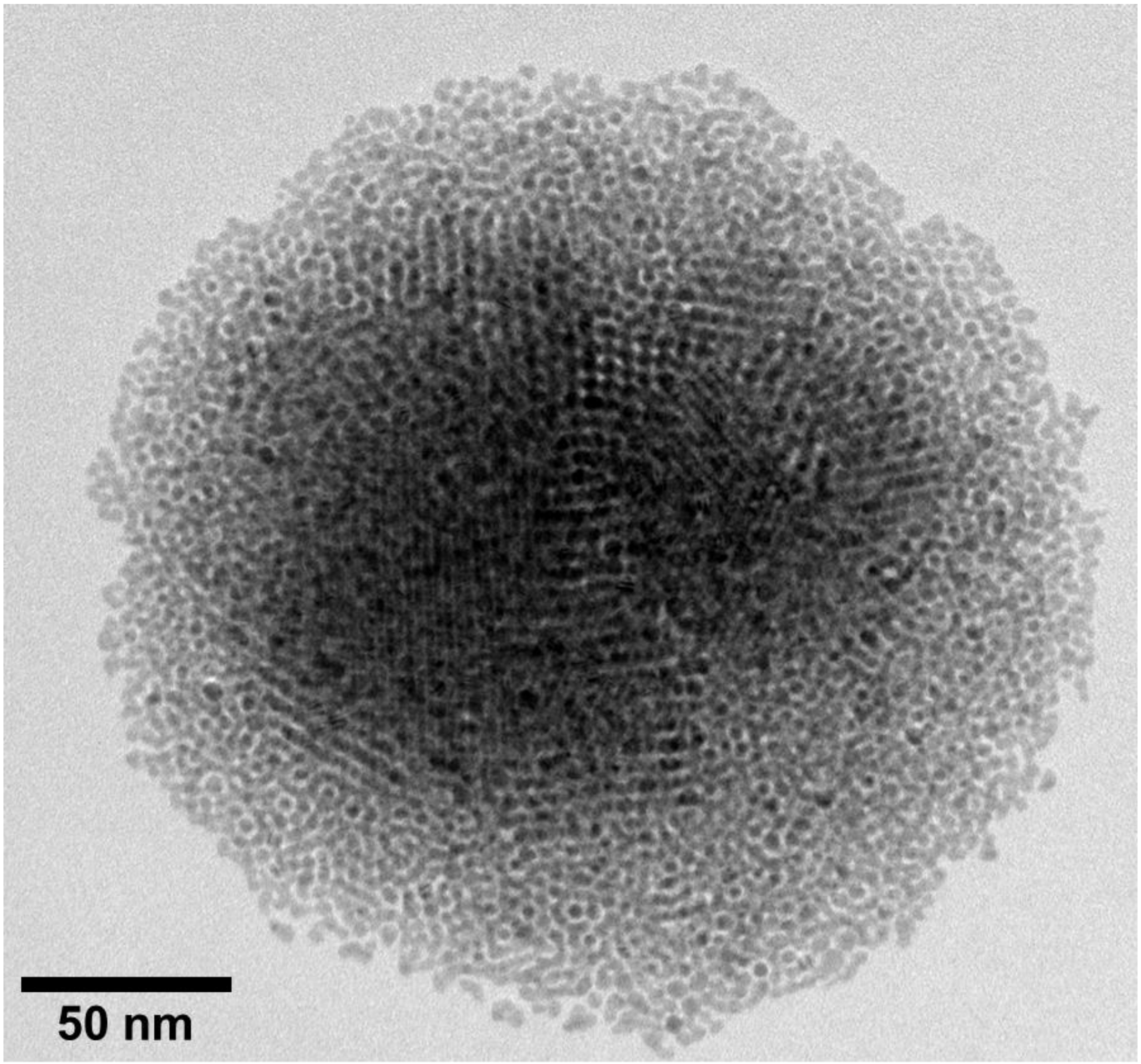

Figure S31. A TEM image showing a magnified view of the same area seen in figure S30. Here, the darker area is clearly visible as a nucleated ordered phase within an envelope of disordered particles.

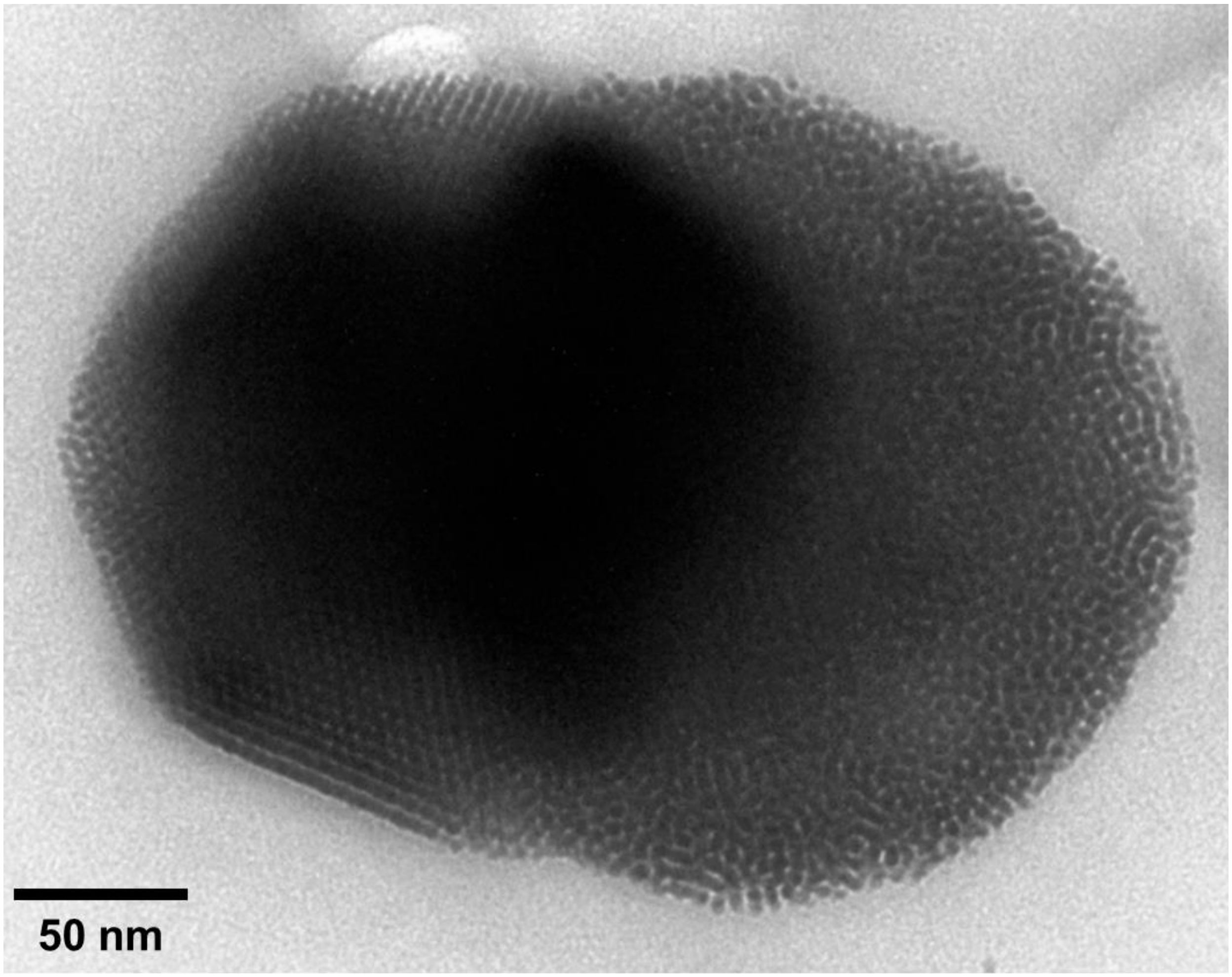

Figure S32. A TEM image showing a crystallization front resulting from an ordered phase nucleating at the left side of the image. Particles on the right side of the structure are seen in a dense but disordered state. This image was obtained by placing a colloid of $(N_2H_5)_2In_2Se_4$ capped Au in a 25 mM solution of $(N_2H_5)_2In_2Se_4$ in hydrazine. A drop of the solution was left to evaporate on a TEM grid causing the MCC ligand concentration to slowly increase over the course of evaporation. In this version of the assembly experiment, the kinetics of ordering compete with solvent evaporation leaving structures as seen above where the ordering process was interrupted by solvent evaporation.

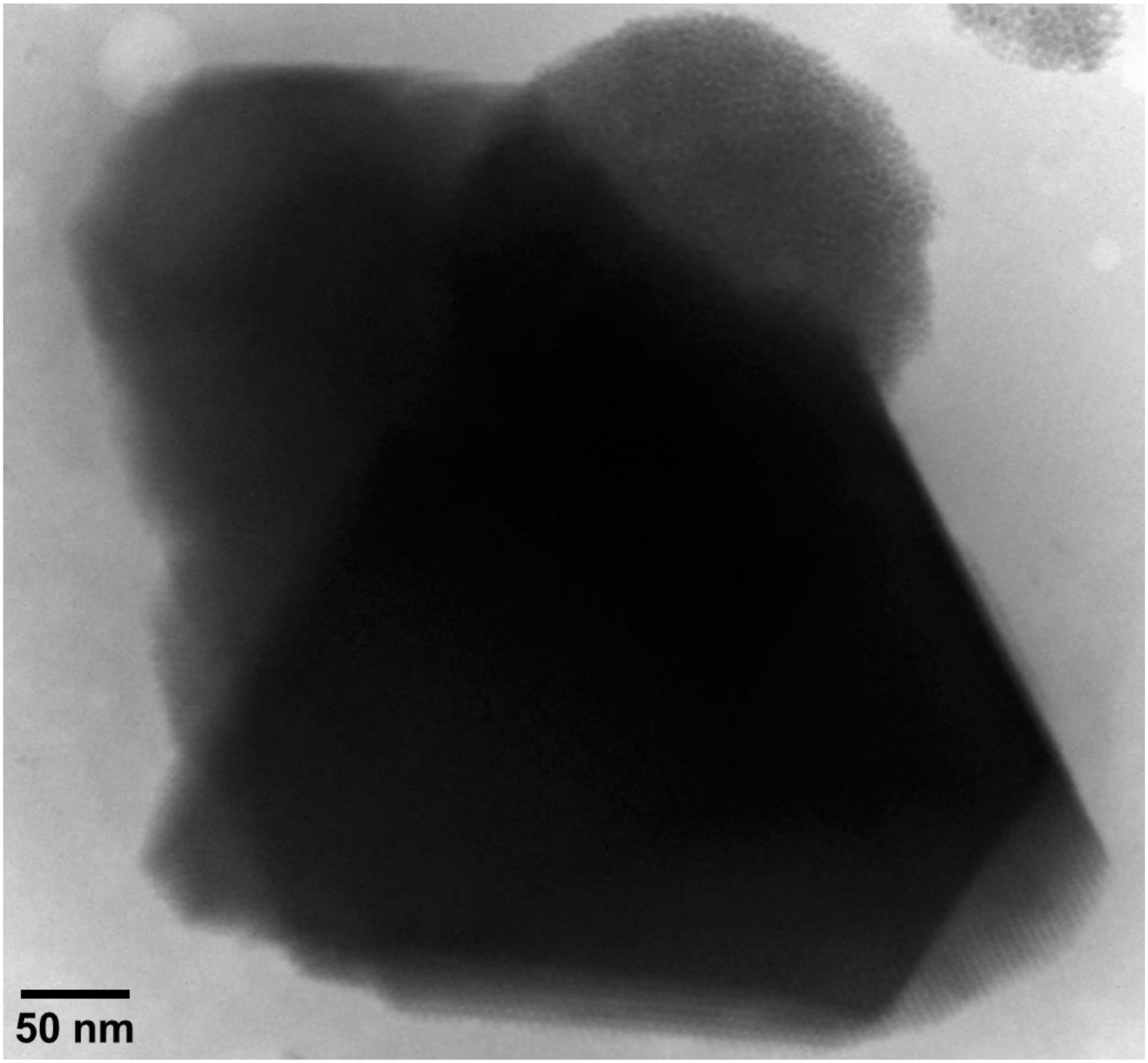

Figure S33. A TEM image showing results of a similar experiment as described for Figure S32 but with $(N_2H_5)_3AsS_4$ capped 4 nm Pd nanoparticles in a 50 mM hydrazine solution of $(N_2H_5)_3AsS_4$. Here, a faceted and supercrystalline structure is seen with a small remaining amount of disordered material near the top of the image.

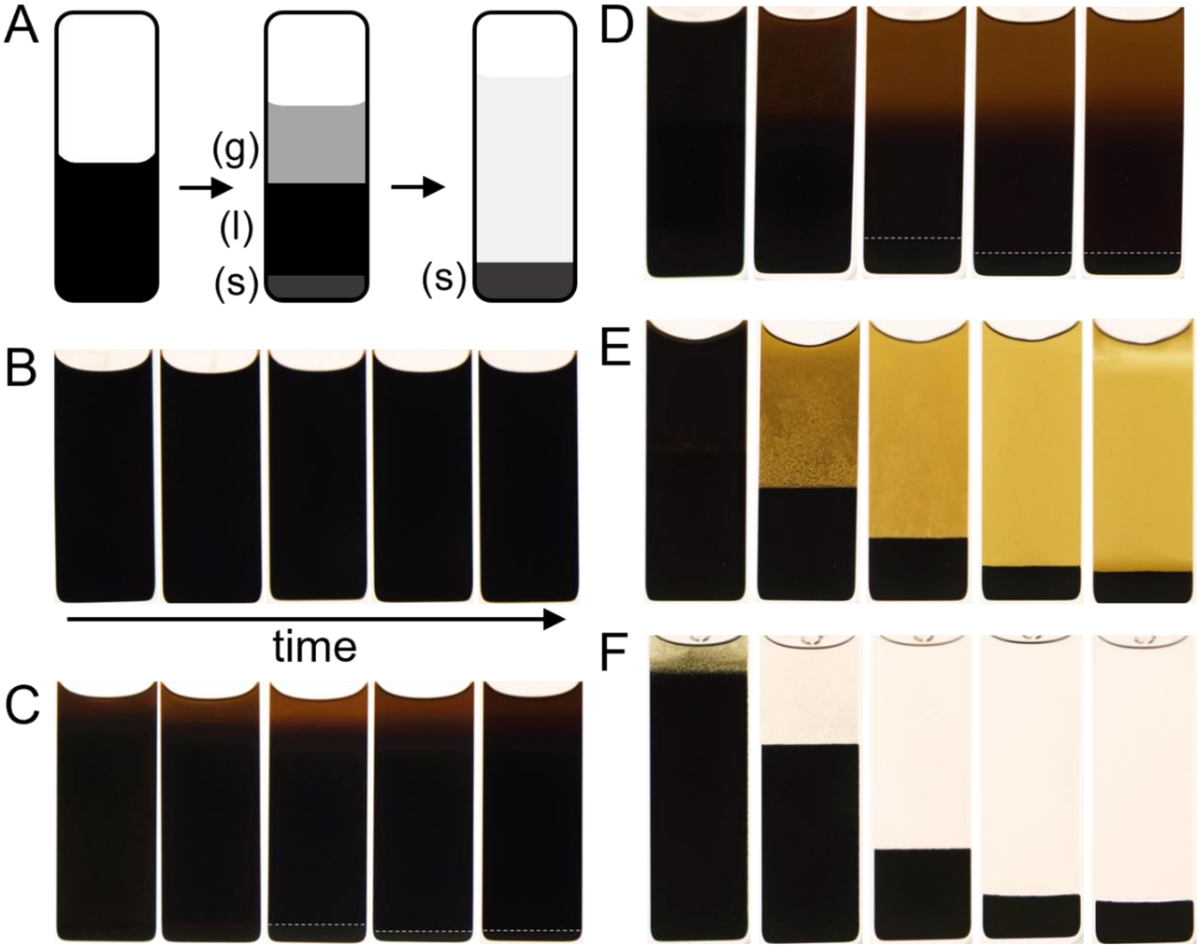

Figure S34. Triple phase coexistence in nanocrystal destabilization. **(A)** Schematic representation of a colloidal solution partially destabilized to a triple phase coexistence and further destabilized to a solid precipitate. **(B-F)** Photographs (1 mm path length) of PbS NCs at 200 mM K_3AsS_4 in NMF with an additional 17, 21, 25, 29, and 32% ACN v/v, respectively, at 10 min, 20 min, 50 min, 11 hr, and 23 hr time points (left to right). Dotted white lines indicate visible solid-liquid phase separation.

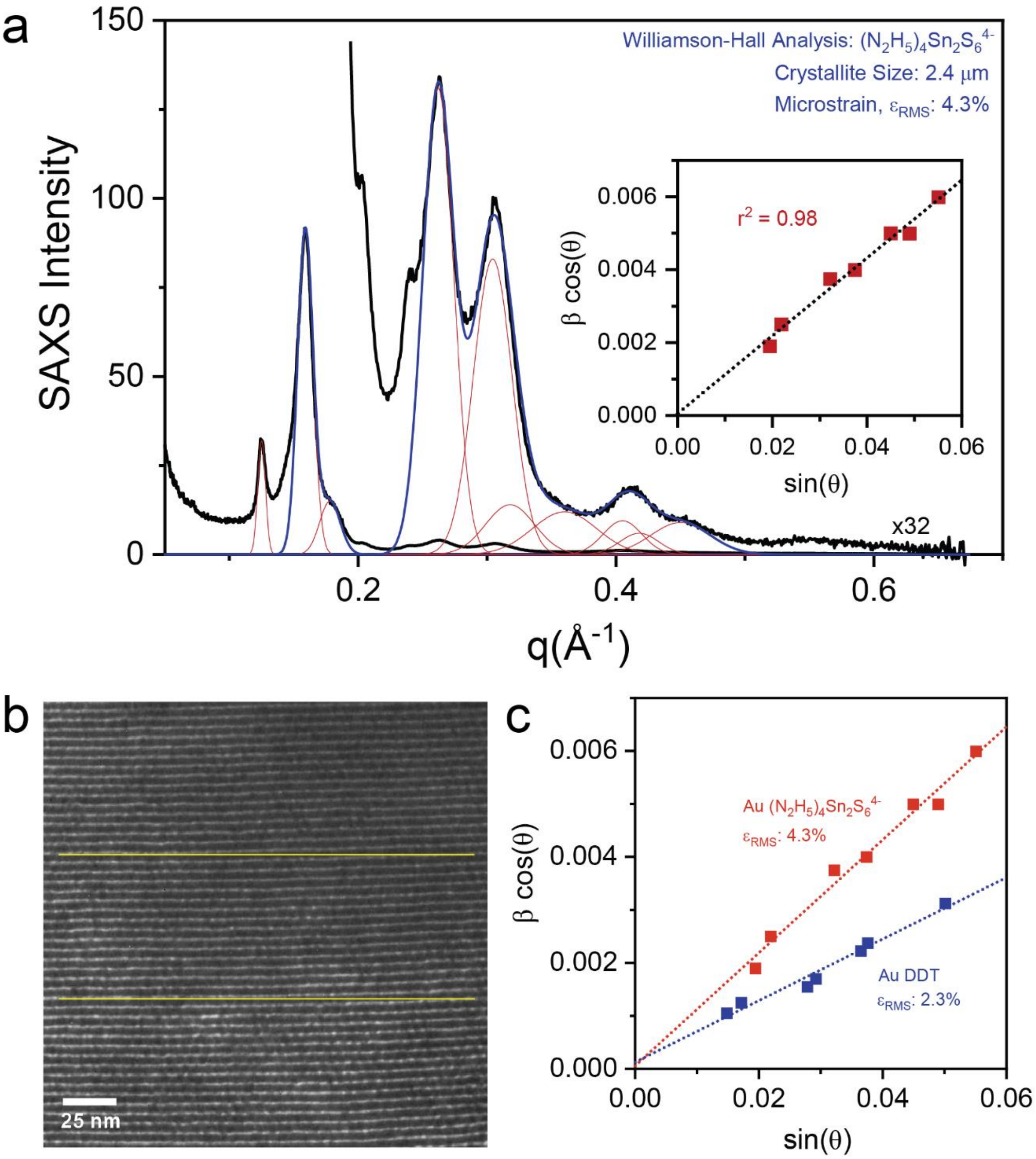

Figure S35. Williamson-Hall analysis of Au NC supercrystals. **(a)** SAXS fitting of 5 nm Au NCs with $Sn_2S_6^{4-}$ ligands. Data are replotted with scaled intensity (x32) to show high q peak fitting. Inset: Linear fit to determine crystallite size (D_{WH}) and apparent strain (η) using the equation $\beta \cos\theta = \frac{k\lambda}{D_{WH}} + \eta \sin\theta$ where β is the integral breadth, λ is the wavelength, and k is a shape factor (0.9 for spherical symmetry used here) (*59*). **(b)** TEM image of the same Au NCs with $Sn_2S_6^{4-}$ ligands showing strain profiles along the crystallographic direction. **(c)** Fitted data from Williamson-Hall analysis with extracted root-mean squared average strain (ε_{RMS}) values for 5 nm Au NCs capped with $Sn_2S_6^{4-}$ and dodecanethiol (DDT) ligands.

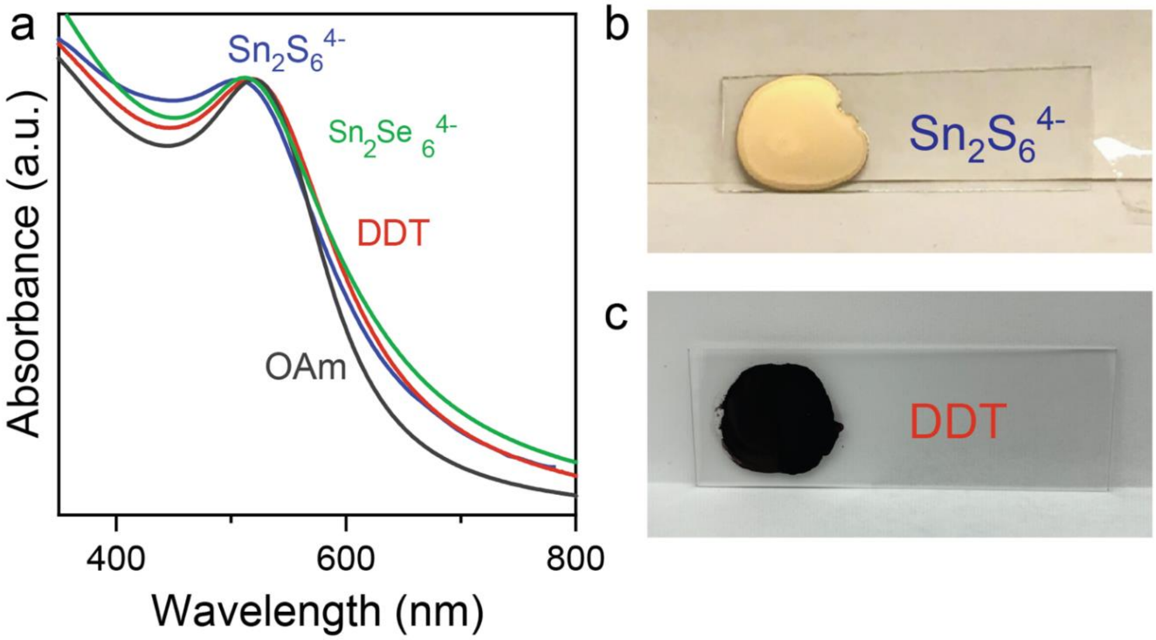

Figure S36. **(a)** Absorbance spectra of solutions of 5 nm diameter Au NCs from the same synthetic batch with native oleylamine ligands (OAm), post-exchange to dodecanethiol (DDT) ligands, and after phase transfer into hydrazine and capping with $(N_2H_5)_4Sn_2S_6$ and $(N_2H_5)_4Sn_2Se_6$. The localized surface plasmon resonance (LSPR) is evident as an absorbance peak in all cases. **(b)** Image of a Au NC film with $(N_2H_5)_4Sn_2S_6$ ligands showing a reflective, metallic surface and **(c)** DDT ligands with low reflectance.

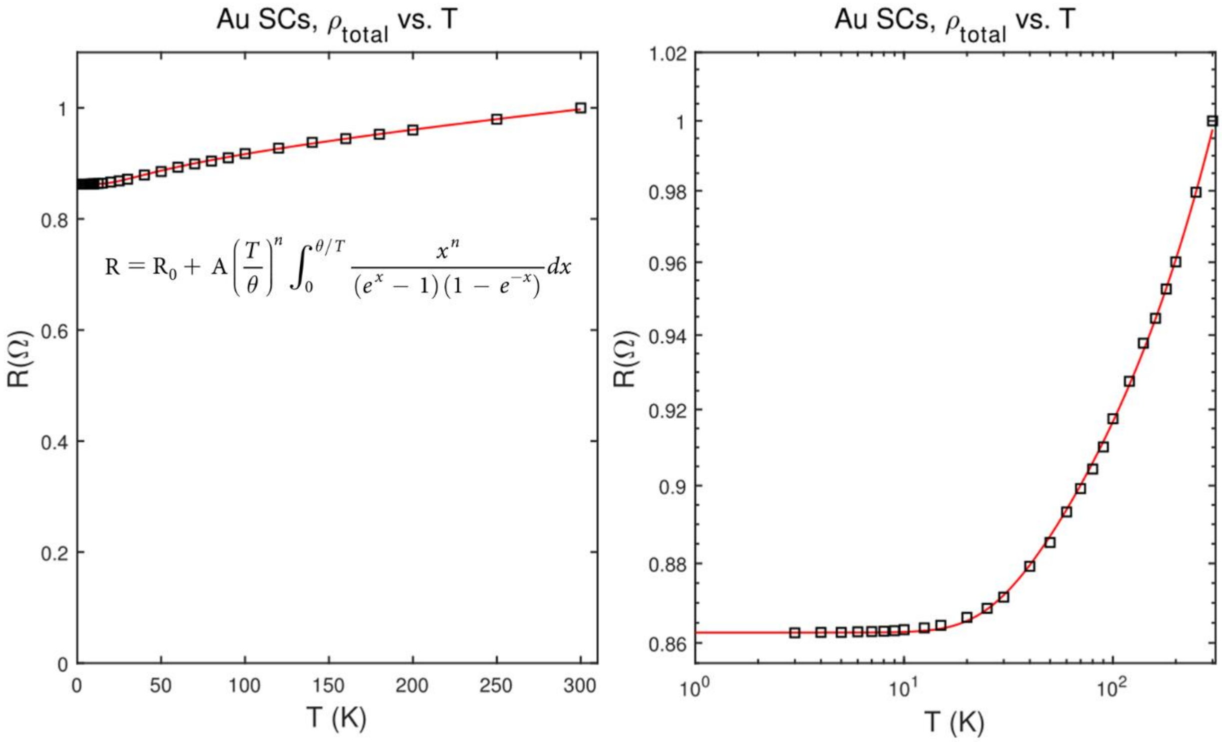

Figure S37. Temperature dependent resistivity data for $Sn_2Se_6^{4-}$ capped Au SCs. Data points are plotted as open black squares, linear scale on the left, log–log scale on the right. The solid red line is a Bloch–Grüneisen model fit plotted according to the expression inset in the left panel. The exponential factor is set at n = 4.75 and Debye temperature θ = 135 K. The constants A and R_0 are a normalization factor and an offset for residual resistance, respectively.

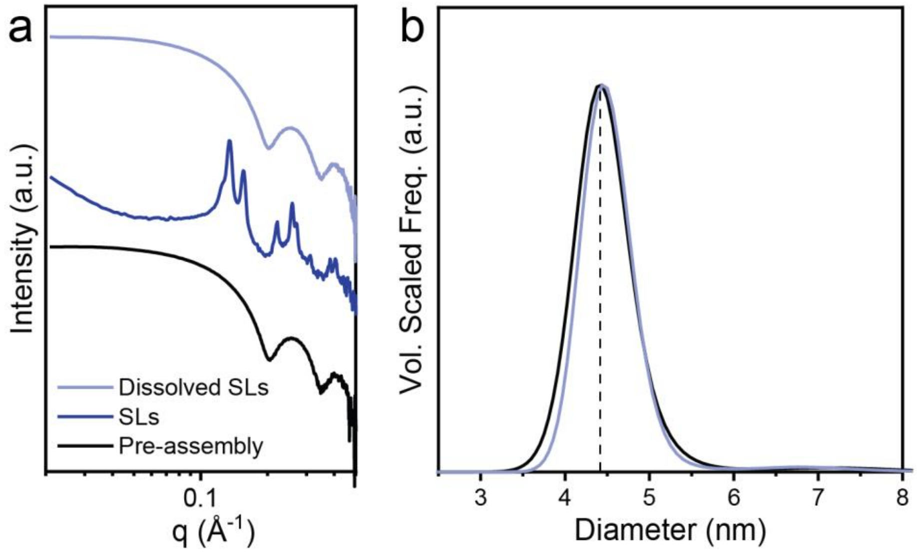

Figure S38. (a) SAXS patterns of 4.5 nm Au NCs before assembly (bottom), after assembly into superlattices (middle), and after redissolution of the superlattices in hydrazine (top). **(b)** Extracted size distribution for Au particles before assembly into superlattices and after redissolution into hydrazine.

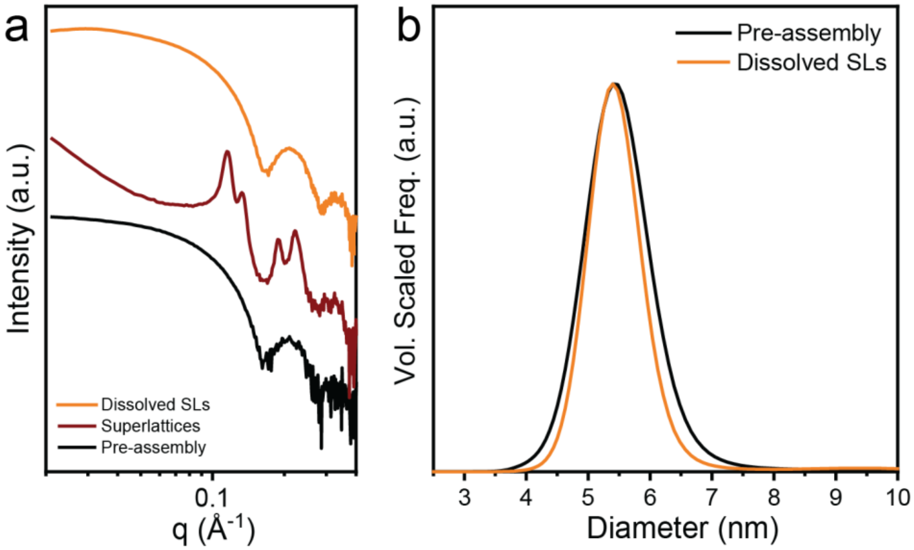

Figure S39. (a) SAXS patterns of 5.5 nm PbS before assembly (bottom), after assembly into superlattices (middle), and after redissolution of the superlattices in NMF (top). **(b)** Extracted size distribution for PbS particles before assembly into superlattices and after redissolution into NMF.

References and Notes

1. D. Vanmaekelbergh, Self-assembly of colloidal nanocrystals as route to novel classes of nanostructured materials. *Nano Today* **6**, 419–437 (2011). doi:10.1016/j.nantod.2011.06.005

2. M. A. Boles, M. Engel, D. V. Talapin, Self-assembly of colloidal nanocrystals: From Intricate structures to functional materials. *Chem. Rev.* **116**, 11220–11289 (2016). doi:10.1021/acs.chemrev.6b00196 Medline

3. C. B. Murray, C. R. Kagan, M. G. Bawendi, Synthesis and characterization of monodisperse nanocrystals and close-packed nanocrystal assemblies. *Annu. Rev. Mater. Sci.* **30**, 545–610 (2000). doi:10.1146/annurev.matsci.30.1.545

4. A. Fortini, E. Sanz, M. Dijkstra, Crystallization and gelation in colloidal systems with short-ranged attractive interactions. *Phys. Rev. E Stat. Nonlin. Soft Matter Phys.* **78**, 041402 (2008). doi:10.1103/PhysRevE.78.041402 Medline

5. E. V. Shevchenko, D. V. Talapin, N. A. Kotov, S. O'Brien, C. B. Murray, Structural diversity in binary nanoparticle superlattices. *Nature* **439**, 55–59 (2006). doi:10.1038/nature04414 Medline

6. M. A. Boles, D. V. Talapin, Many-body effects in nanocrystal superlattices: Departure from sphere packing explains stability of binary phases. *J. Am. Chem. Soc.* **137**, 4494–4502 (2015). doi:10.1021/jacs.5b00839 Medline

7. T. Paik, B. T. Diroll, C. R. Kagan, C. B. Murray, Binary and ternary superlattices self-assembled from colloidal nanodisks and nanorods. *J. Am. Chem. Soc.* **137**, 6662–6669 (2015). doi:10.1021/jacs.5b03234 Medline

8. R. J. Macfarlane, B. Lee, M. R. Jones, N. Harris, G. C. Schatz, C. A. Mirkin, Nanoparticle superlattice engineering with DNA. *Science* **334**, 204–208 (2011). doi:10.1126/science.1210493 Medline

9. D. V. Talapin, E. V. Shevchenko, M. I. Bodnarchuk, X. Ye, J. Chen, C. B. Murray, Quasicrystalline order in self-assembled binary nanoparticle superlattices. *Nature* **461**, 964–967 (2009). doi:10.1038/nature08439 Medline

10. X. Ye, J. Chen, M. Eric Irrgang, M. Engel, A. Dong, S. C. Glotzer, C. B. Murray, Quasicrystalline nanocrystal superlattice with partial matching rules. *Nat. Mater.* **16**, 214–219 (2017). doi:10.1038/nmat4759 Medline

11. N. S. Mueller, Y. Okamura, B. G. M. Vieira, S. Juergensen, H. Lange, E. B. Barros, F. Schulz, S. Reich, Deep strong light-matter coupling in plasmonic nanoparticle crystals. *Nature* **583**, 780–784 (2020). doi:10.1038/s41586-020-2508-1 Medline

12. J. Chen, A. Dong, J. Cai, X. Ye, Y. Kang, J. M. Kikkawa, C. B. Murray, Collective dipolar interactions in self-assembled magnetic binary nanocrystal superlattice membranes. *Nano Lett.* **10**, 5103–5108 (2010). doi:10.1021/nl103568q Medline

13. J.-S. Lee, M. V. Kovalenko, J. Huang, D. S. Chung, D. V. Talapin, Band-like transport, high electron mobility and high photoconductivity in all-inorganic nanocrystal arrays. *Nat. Nanotechnol.* **6**, 348–352 (2011). doi:10.1038/nnano.2011.46 Medline

14. M. Y. Lin, H. M. Lindsay, D. A. Weitz, R. C. Ball, R. Klein, P. Meakin, Universality in colloid aggregation. *Nature* **339**, 360–362 (1989). doi:10.1038/339360a0

15. G. H. Carey, K. W. Chou, B. Yan, A. R. Kirmani, A. Amassian, E. H. Sargent, Materials processing strategies for colloidal quantum dot solar cells: Advances, present-day limitations, and pathways to improvement. *MRS Commun.* **3**, 83–90 (2013). doi:10.1557/mrc.2013.17

16. M. P. Boneschanscher, W. H. Evers, J. J. Geuchies, T. Altantzis, B. Goris, F. T. Rabouw, S. A. P. van Rossum, H. S. J. van der Zant, L. D. A. Siebbeles, G. Van Tendeloo, I. Swart, J. Hilhorst, A. V. Petukhov, S. Bals, D. Vanmaekelbergh, Long-range orientation and atomic attachment of nanocrystals in 2D honeycomb superlattices. *Science* **344**, 1377–1380 (2014). doi:10.1126/science.1252642 Medline

17. A. Abelson, C. Qian, T. Salk, Z. Luan, K. Fu, J. G. Zheng, J. L. Wardini, M. Law, Collective topo-epitaxy in the self-assembly of a 3D quantum dot superlattice. *Nat. Mater.* **19**, 49–55 (2020). doi:10.1038/s41563-019-0485-2 Medline

18. K. Whitham, J. Yang, B. H. Savitzky, L. F. Kourkoutis, F. Wise, T. Hanrath, Charge transport and localization in atomically coherent quantum dot solids. *Nat. Mater.* **15**, 557–563 (2016). doi:10.1038/nmat4576 Medline

19. D. M. Balazs, D. N. Dirin, H.-H. Fang, L. Protesescu, G. H. ten Brink, B. J. Kooi, M. V. Kovalenko, M. A. Loi, Counterion-mediated ligand exchange for PbS colloidal quantum dot superlattices. *ACS Nano* **9**, 11951–11959 (2015). doi:10.1021/acsnano.5b04547 Medline

20. M. C. Weidman, K. G. Yager, W. A. Tisdale, Interparticle spacing and structural ordering in superlattice PbS nanocrystal solids undergoing ligand exchange. *Chem. Mater.* **27**, 474–482 (2015). doi:10.1021/cm503626s

21. M. V. Kovalenko, M. Scheele, D. V. Talapin, Colloidal nanocrystals with molecular metal chalcogenide surface ligands. *Science* **324**, 1417–1420 (2009). doi:10.1126/science.1170524 Medline

22. A. E. Saunders, B. A. Korgel, Second virial coefficient measurements of dilute gold nanocrystal dispersions using small-angle X-ray scattering. *J. Phys. Chem. B* **108**, 16732–16738 (2004). doi:10.1021/jp047153j

23. J. N. Israelachvili, *Intermolecular and Surface Forces* (Elsevier, 1985).

24. P. R. ten Wolde, D. Frenkel, Enhancement of protein crystal nucleation by critical density fluctuations. *Science* **277**, 1975–1978 (1997). doi:10.1126/science.277.5334.1975 Medline

25. T. K. Haxton, L. O. Hedges, S. Whitelam, Crystallization and arrest mechanisms of model colloids. *Soft Matter* **11**, 9307–9320 (2015). doi:10.1039/C5SM01833A Medline

26. M. G. Noro, D. Frenkel, Extended corresponding-states behavior for particles with variable range attractions. *J. Chem. Phys.* **113**, 2941–2944 (2000). doi:10.1063/1.1288684

27. N. Kallay, S. Žalac, Stability of nanodispersions: A model for kinetics of aggregation of nanoparticles. *J. Colloid Interface Sci.* **253**, 70–76 (2002). doi:10.1006/jcis.2002.8476 Medline

28. H. Liu, S. Garde, S. Kumar, Direct determination of phase behavior of square-well fluids. *J. Chem. Phys.* **123**, 174505 (2005). doi:10.1063/1.2085051 Medline

29. W. C. K. Poon, F. Renth, R. M. L. Evans, D. J. Fairhurst, M. E. Cates, P. N. Pusey, Colloid-polymer mixtures at triple coexistence: Kinetic maps from free-energy landscapes. *Phys. Rev. Lett.* **83**, 1239–1242 (1999). doi:10.1103/PhysRevLett.83.1239

30. M. Muschol, F. Rosenberger, Liquid–liquid phase separation in supersaturated lysozyme solutions and associated precipitate formation/crystallization. *J. Chem. Phys.* **107**, 1953–1962 (1997). doi:10.1063/1.474547

31. P. N. Pusey, W. van Megen, Phase behaviour of concentrated suspensions of nearly hard colloidal spheres. *Nature* **320**, 340–342 (1986). doi:10.1038/320340a0

32. D. Klotsa, R. L. Jack, Predicting the self-assembly of a model colloidal crystal. *Soft Matter* **7**, 6294–6303 (2011). doi:10.1039/c1sm05456b

33. T. Bian, A. Gardin, J. Gemen, L. Houben, C. Perego, B. Lee, N. Elad, Z. Chu, G. M. Pavan, R. Klajn, Electrostatic co-assembly of nanoparticles with oppositely charged small molecules into static and dynamic superstructures. *Nat. Chem.* **13**, 940–949 (2021). doi:10.1038/s41557-021-00752-9 Medline

34. J. W. Zwanikken, M. Olvera de la Cruz, Tunable soft structure in charged fluids confined by dielectric interfaces. *Proc. Natl. Acad. Sci. U.S.A.* **110**, 5301–5308 (2013). doi:10.1073/pnas.1302406110 Medline

35. Y. Jing, V. Jadhao, J. W. Zwanikken, M. Olvera de la Cruz, Ionic structure in liquids confined by dielectric interfaces. *J. Chem. Phys.* **143**, 194508 (2015). doi:10.1063/1.4935704 Medline

36. R. M. Malossi, M. Girotto, A. P. Dos Santos, Y. Levin, Simulations of electrolyte between charged metal surfaces. *J. Chem. Phys.* **153**, 044121 (2020). doi:10.1063/5.0012073 Medline

37. G. I. Guerrero García, M. Olvera de la Cruz, Polarization effects of dielectric nanoparticles in aqueous charge-asymmetric electrolytes. *J. Phys. Chem. B* **118**, 8854–8862 (2014). doi:10.1021/jp5045173 Medline

38. O. Gliko, N. Neumaier, W. Pan, I. Haase, M. Fischer, A. Bacher, S. Weinkauf, P. G. Vekilov, A metastable prerequisite for the growth of lumazine synthase crystals. *J. Am. Chem. Soc.* **127**, 3433–3438 (2005). doi:10.1021/ja043218k Medline

39. A. Sauter, F. Roosen-Runge, F. Zhang, G. Lotze, A. Feoktystov, R. M. J. Jacobs, F. Schreiber, On the question of two-step nucleation in protein crystallization. *Faraday Discuss.* **179**, 41–58 (2015). doi:10.1039/C4FD00225C Medline

40. J. Chelikowsky, *Quantum Theory of Real Materials* (Springer, 1996).

41. A. F. Clark, G. E. Childs, G. H. Wallace, Electrical resistivity of some engineering alloys at low temperatures. *Cryogenics* **10**, 295–305 (1970). doi:10.1016/0011-2275(70)90056-1

42. J. Bardeen, Electrical Conductivity of Metals. *J. Appl. Phys.* **11**, 88–111 (1940). doi:10.1063/1.1712751

43. C. Yamanouchi, K. Mizuguchi, W. Sasaki, Electric conduction in phosphorus doped silicon

at low temperatures. *J. Phys. Soc. Jpn.* **22**, 859–864 (1967). doi:10.1143/JPSJ.22.859

44. A. Zabet-Khosousi, A.-A. Dhirani, Charge transport in nanoparticle assemblies. *Chem. Rev.* **108**, 4072–4124 (2008). doi:10.1021/cr0680134 Medline
45. S. Henrichs, C. P. Collier, R. J. Saykally, Y. R. Shen, J. R. Heath, The dielectric function of silver nanoparticle Langmuir monolayers compressed through the metal insulator transition. *J. Am. Chem. Soc.* **122**, 4077–4083 (2000). doi:10.1021/ja991543f
46. J.-H. Choi, H. Wang, S. J. Oh, T. Paik, P. Sung, J. Sung, X. Ye, T. Zhao, B. T. Diroll, C. B. Murray, C. R. Kagan, Exploiting the colloidal nanocrystal library to construct electronic devices. *Science* **352**, 205–208 (2016). doi:10.1126/science.aad0371 Medline
47. Y. Yu, D. Yu, B. Sadigh, C. A. Orme, Space- and time-resolved small angle X-ray scattering to probe assembly of silver nanocrystal superlattices. *Nat. Commun.* **9**, 4211 (2018). doi:10.1038/s41467-018-06734-9 Medline
48. X. Lan, M. Chen, M. H. Hudson, V. Kamysbayev, Y. Wang, P. Guyot-Sionnest, D. V. Talapin, Quantum dot solids showing state-resolved band-like transport. *Nat. Mater.* **19**, 323–329 (2020). doi:10.1038/s41563-019-0582-2 Medline
49. S. Peng, Y. Lee, C. Wang, H. Yin, S. Dai, S. Sun, A facile synthesis of monodisperse Au nanoparticles and their catalysis of CO oxidation. *Nano Res.* **1**, 229–234 (2008). doi:10.1007/s12274-008-8026-3
50. P. P. Wang, Q. Qiao, Y. Zhu, M. Ouyang, Colloidal binary supracrystals with tunable structural lattices. *J. Am. Chem. Soc.* **140**, 9095–9098 (2018). doi:10.1021/jacs.8b05643 Medline
51. L. Wu, J. J. Willis, I. S. McKay, B. T. Diroll, J. Qin, M. Cargnello, C. J. Tassone, High-temperature crystallization of nanocrystals into three-dimensional superlattices. *Nature* **548**, 197–201 (2017). doi:10.1038/nature23308 Medline
52. M. Cargnello, V. V. T. Doan-Nguyen, T. R. Gordon, R. E. Diaz, E. A. Stach, R. J. Gorte, P. Fornasiero, C. B. Murray, Control of metal nanocrystal size reveals metal-support interface role for ceria catalysts. *Science* **341**, 771–773 (2013). doi:10.1126/science.1240148 Medline
53. D. V. Talapin, J. H. Nelson, E. V. Shevchenko, S. Aloni, B. Sadtler, A. P. Alivisatos, Seeded growth of highly luminescent CdSe/CdS nanoheterostructures with rod and tetrapod morphologies. *Nano Lett.* **7**, 2951–2959 (2007). doi:10.1021/nl072003g Medline
54. O. Chen, X. Chen, Y. Yang, J. Lynch, H. Wu, J. Zhuang, Y. C. Cao, Synthesis of metal-selenide nanocrystals using selenium dioxide as the selenium precursor. *Angew. Chem. Int. Ed.* **47**, 8638–8641 (2008). doi:10.1002/anie.200804266 Medline
55. J. Zhang, R. W. Crisp, J. Gao, D. M. Kroupa, M. C. Beard, J. M. Luther, Synthetic conditions for high-accuracy size control of PbS quantum dots. *J. Phys. Chem. Lett.* **6**, 1830–1833 (2015). doi:10.1021/acs.jpclett.5b00689 Medline
56. Z. Quan, D. Wu, J. Zhu, W. H. Evers, J. M. Boncella, L. D. A. Siebbeles, Z. Wang, A. Navrotsky, H. Xu, Energy landscape of self-assembled superlattices of PbSe nanocrystals. *Proc. Natl. Acad. Sci. U.S.A.* **111**, 9054–9057 (2014). doi:10.1073/pnas.1408835111 Medline

57. M. V. Kovalenko, M. I. Bodnarchuk, J. Zaumseil, J.-S. Lee, D. V. Talapin, Expanding the chemical versatility of colloidal nanocrystals capped with molecular metal chalcogenide ligands. *J. Am. Chem. Soc.* **132**, 10085–10092 (2010). doi:10.1021/ja1024832 Medline

58. S. Biggs, P. Mulvaney, Measurement of the forces between gold surfaces in water by atomic force microscopy. *J. Chem. Phys.* **100**, 8501–8505 (1994). doi:10.1063/1.466748

59. W. B. Russel, D. A. Saville, W. R. Schowalter, *Colloidal Dispersions* (Cambridge Univ. Press, 1989).

60. P. Meakin, F. Family, Structure and kinetics of reaction-limited aggregation. *Phys. Rev. A Gen. Phys.* **38**, 2110–2123 (1988). doi:10.1103/PhysRevA.38.2110 Medline

61. S. Jungblut, J.-O. Joswig, A. Eychmüller, Diffusion- and reaction-limited cluster aggregation revisited. *Phys. Chem. Chem. Phys.* **21**, 5723–5729 (2019). doi:10.1039/C9CP00549H Medline

62. D. Frenkel, Entropy-driven phase transitions. *Physica A* **263**, 26–38 (1999). doi:10.1016/S0378-4371(98)00501-9

63. M. I. Bodnarchuk, M. V. Kovalenko, W. Heiss, D. V. Talapin, Energetic and entropic contributions to self-assembly of binary nanocrystal superlattices: Temperature as the structure-directing factor. *J. Am. Chem. Soc.* **132**, 11967–11977 (2010). doi:10.1021/ja103083q Medline

64. T. A. Witten, L. M. Sander, Diffusion-limited aggregation, a kinetic critical phenomenon. *Phys. Rev. Lett.* **47**, 1400–1403 (1981). doi:10.1103/PhysRevLett.47.1400

65. S. Plimpton, Fast parallel algorithms for short-range molecular dynamics. *J. Comput. Phys.* **117**, 1–19 (1995). doi:10.1006/jcph.1995.1039

66. J. D. Weeks, D. Chandler, H. C. Andersen, Role of repulsive forces in determining the equilibrium structure of simple liquids. *J. Chem. Phys.* **54**, 5237–5247 (1971). doi:10.1063/1.1674820

67. P. J. Steinhardt, D. R. Nelson, M. Ronchetti, Bond-orientational order in liquids and glasses. *Phys. Rev. B Condens. Matter* **28**, 784–805 (1983). doi:10.1103/PhysRevB.28.784

68. Y. Li, M. Girard, M. Shen, J. A. Millan, M. Olvera de la Cruz, Strong attractions and repulsions mediated by monovalent salts. *Proc. Natl. Acad. Sci. U.S.A.* **114**, 11838–11843 (2017). doi:10.1073/pnas.1713168114 Medline

69. F. Jiménez-Ángeles, K. J. Harmon, T. D. Nguyen, P. Fenter, M. Olvera de la Cruz, Nonreciprocal interactions induced by water in confinement. *Phys. Rev. Res.* **2**, 043244 (2020). doi:10.1103/PhysRevResearch.2.043244

70. T. D. Nguyen, H. Li, D. Bagchi, F. J. Solis, M. Olvera de la Cruz, Incorporating surface polarization effects into large-scale coarse-grained molecular dynamics simulation. *Comput. Phys. Commun.* **241**, 80–91 (2019). doi:10.1016/j.cpc.2019.03.006

71. P. Tao, A. J. Sodt, Y. Shao, G. König, B. R. Brooks, Computing the free energy along a reaction coordinate using rigid body dynamics. *J. Chem. Theory Comput.* **10**, 4198–4207 (2014). doi:10.1021/ct500342h Medline

72. C. Chipot, M. S. Shell, A. Pohorille, “Free energy calculations: Theory and applications in

chemistry and biology," in *Springer Series in Chemical Physics*, P. Toennies, K. Yamanouchi, Eds. (2007), vol. 86, pp. 1–31.

73. G. I. Guerrero-García, P. González-Mozuelos, M. Olvera de la Cruz, Potential of mean force between identical charged nanoparticles immersed in a size-asymmetric monovalent electrolyte. *J. Chem. Phys.* **135**, 164705 (2011). doi:10.1063/1.3656763 Medline

74. M. H. J. Hagen, D. Frenkel, Determination of phase diagrams for the hard-core attractive Yukawa system. *J. Chem. Phys.* **101**, 4093–4097 (1994). doi:10.1063/1.467526

75. D. Frenkel, B. Smit, *Understanding Molecular Simulation* (Elsevier, 2002).

76. A. Dong, Y. Jiao, D. J. Milliron, Electronically coupled nanocrystal superlattice films by in situ ligand exchange at the liquid-air interface. *ACS Nano* **7**, 10978–10984 (2013). doi:10.1021/nn404566b Medline

77. P. Guyot-Sionnest, Electrical transport in colloidal quantum dot films. *J. Phys. Chem. Lett.* **3**, 1169–1175 (2012). doi:10.1021/jz300048y Medline

78. Y. Liu, M. Gibbs, J. Puthussery, S. Gaik, R. Ihly, H. W. Hillhouse, M. Law, Dependence of carrier mobility on nanocrystal size and ligand length in PbSe nanocrystal solids. *Nano Lett.* **10**, 1960–1969 (2010). doi:10.1021/nl101284k Medline

79. M. Mamode, Electrical resistance between pairs of vertices of a conducting cube and continuum limit for a cubic resistor network. *J. Phys. Commun.* **1**, 35002 (2017). doi:10.1088/2399-6528/aa8ab6

80. H. Liu, E. Lhuillier, P. Guyot-Sionnest, 1/f noise in semiconductor and metal nanocrystal solids. *J. Appl. Phys.* **115**, 154309 (2014). doi:10.1063/1.4871682

81. S. Lee, M. J. Bluemle, F. S. Bates, Discovery of a Frank-Kasper σ phase in sphere-forming block copolymer melts. *Science* **330**, 349–353 (2010). doi:10.1126/science.1195552 Medline

82. G. K. Williamson, W. H. Hall, X-ray line broadening from filed aluminium and wolfram. *Acta Metall.* **1**, 22–31 (1953). doi:10.1016/0001-6160(53)90006-6